2011

Design of a Hand Held Minimally Invasive Lung Tumour Localization Device

Tomasz Piotr Kurowski

Design of a Hand Held Minimally Invasive Lung Tumour Localization Device

(Spine Title: A Minimally Invasive Lung Tumour Localization Device)

(Thesis Format: Monograph)

by

Tomasz P. Kurowski

Faculty of Engineering Science

Department of Mechanical and Materials Engineering

Submitted in partial fulfillment

of the requirements for the degree of

Master of Engineering Science

School of Graduate and Postdoctoral Studies

The University of Western Ontario

London, Ontario, Canada

THE UNIVERSITY OF WESTERN ONTARIO
School of Graduate and Postdoctoral Studies

CERTIFICATE OF EXAMINATION

Supervisor

Dr. Michael Naish

Examining Board:

Dr. Ralph Buchal

Dr. Rajni Patel

Dr. Shaun Salisbury

The thesis by
Tomasz Kurowski
entitled
Design of a Hand Held Minimally Invasive Lung Tumour Localization Device

is accepted in partial fulfillment of the
requirements for the degree of
Master of Engineering Science

Date: _____

Chairman of Examining Board

Design of a Hand Held Minimally Invasive Lung Tumour Localization Device

Tomasz P. Kurowski

M.E.Sc. Thesis, 2011

Department of Mechanical and Materials Engineering

University of Western Ontario

Abstract

Lung cancer is the leading type of cancer that causes death. If diagnosed, the treatment of choice is surgical resection of the tumour. Traditionally, a surgeon feels for the presence of a tumour in open thoracic surgery. However, a minimally invasive approach is desired. A major problem presented by the minimally invasive approach is the localization of the tumour.

This project describes the design, analysis, and experimental validation of a novel minimally invasive instrument for lung tumour localization. The instrument end effector is a two degree of freedom lung tissue palpator. It allows for optimal tissue palpation to increase useful sensor feedback by ensuring sensor contact, and prevents tissue damage by uniformly distributing pressure on the tissue with an upper bound force. Finite element analysis was used extensively to guide the design process. The mechanism is actuated using high strength tungsten cables attached to controlled motors. Heat treatment experiments were undertaken with stainless steel alloy 440C for use in the design, achieving a device factor of safety of 4. This factor of safety is based on a 20 N force on the end effector — the approximate weight of a human lung.

The design was prototyped and validation experiments were carried out to assess its articulation and its load carrying capacity. Up to 10 N of force was applied to the prototype. Issues to resolve in the current design include cable extension effects and the existence of joint inflection.

The end effector was also designed to allow the inclusion of ultrasound, tactile, and kinaesthetic sensors. It is hypothesized that a plurality of sensors will increase the likelihood of positive tumour localization. These sensors, combined with the presented mechanical design, form the basis for research in robotics-assisted palpation. A proof of concept control system is presented for automated palpation.

Acknowledgements

I would like to thank my supervisor Dr. Michael Naish, whose help and guidance was always available and contributed in large part to this project.

I would also like to thank a few professors at the University of Western Ontario who kindly provided advice for many aspects of my project, including Dr. Shaun Salisbury and Dr. Jeff Wood.

Furthermore, without the assistance of the University Machine Services at the University of Western Ontario, the final prototype would not have been completed. The help and patience of Kevin Barker and his team is greatly appreciated.

Canadian Surgical Technologies and Advanced Robotics (CSTAR) founded the basis of my project working on minimally invasive medical instruments. I thank the Director of Engineering, Dr. Rajni Patel for his presence and guidance in my project.

I want to express thanks to my mother and father, Paweł Kurowski and Elżbieta Kurowska. My father, an Assistant Professor at the University of Western Ontario continuously provided help and always had an answer for me. His experience in the various fields of Mechanical Engineering provided a new foundation for my knowledge. His teachings will never be forgotten. To my mother, thank you for your support and to listening about my work.

To my girlfriend, Kristin Elliott — thank you for your support and patience with me. I'm glad you took interest in my project and made sure you understood what I was doing. Your kindness and caring has always been comforting.

I want to thank my friends for great times and experiences — Jeremy Breetzke, Jeremy Cepek, Christopher DeGroot, David Del Rey Fernandez, Steve Farron, Christian Fischer, and Christopher Ward.

Finally, the financial support of the MITACS Accelerate program and Dr. Richard Malthaner on behalf of the London Health Science Centre is gratefully acknowledged.

Contents

List of Figures

List of Tables

Nomenclature and Acronyms

Latin Letters

l	The length of a linkage
t_d	The desired thickness of palpation

Greek Letters

θ	An angle between linkages
θ_d	The desired angle of palpation

Acronyms

1D	One-Dimensional
2D	Two-Dimensional
3D	Three-Dimensional
ABS	Acrylonitrile Butadiene Styrene
DOF	Degree of Freedom
FEA	Finite Element Analysis
FOS	Factor of Safety
FSR	Force Sensing Resistor
LED	Light Emitting Diode
MIS	Minimally Invasive Surgery

MITS	Minimally Invasive Thoracoscopic Surgery
PEEK	Polyether Ether Ketone
P	Proportional (controller)
PC	Personal Computer
PID	Proportional Integral Derivative (controller)
PPS	Pressure Profile Systems Inc.
PVDF	Polyvinylidene Fluoride

Chapter 1

Introduction

1.1 Motivation

Lung cancer is the leading type of cancer that causes death in men and women. In 2010, it is estimated that 20,600 Canadians will have died of lung cancer, and 24,200 will have been diagnosed with lung cancer [1]. The survival rate after a five year period from diagnosis is less than 17% in both men and women [2]. Once lung cancer has been diagnosed, the treatment of choice is surgical resection of the tumour. While minimally invasive surgery (MIS) serves to reduce patient mortality and trauma, localization of tumours during lung cancer treatment presents a significant challenge. This, combined with the limitations of currently available minimally invasive devices, motivate the development of an instrument that offers improved effectiveness for minimally invasive lung tumour localization.

1.2 Current Technologies

In traditional open thoracic surgery, the surgeon palpates or feels the target tissue with a gloved hand. This approach allows the surgeon to characterize tissue by sensing the tactile and kinaesthetic feel with his or her fingers. An underlying tumour is identified by the feeling of a spheroid lump within the tissue, because tumours typically exhibit a higher stiffness than the surrounding healthy tissue.

Although there are benefits to be realized from avoiding open thoracic surgery, MIS forces palpation to be done with instruments that are inherently difficult to use due to reversed instrument movement[1], a lack of direct vision, a loss of kinaesthetic force perception due to friction and elastic effects of the tissue at the trocar[2], and the complete loss of tactile perception. A standard Mediflex Surgical Products Babcock grasper in a jaws closed position is commonly used to palpate tissue. With this instrument, the surgeon attempts to determine tissue stiffness by feeling the force exerted on the instrument handle, or by visually inspecting the characteristics of the tissue as seen through an endoscopic camera. If the surgeon palpates too hard with the instrument, this limited feedback palpation method can lead to permanent tissue damage. Palpation experiments conducted with and without force feedback have shown that excessive palpation forces are often applied when no feedback is available [3]. Incorrect tumour detection can also occur because it is difficult to differentiate a tumour from any other hard underlying tissue due to a lack of tactile shape perception. These problems inspire the work of many researchers and motivate the design of systems to overcome them.

1.3 Forms of Feedback

To prevent damage to the tissue, to decrease the time of a minimally invasive procedure, and to help reliably localize a lung tumour, existing intraoperative techniques commonly use kinaesthetic feedback, tactile feedback, and ultrasound feedback.

1.3.1 Kinaesthetic Feedback

Kinaesthetic information is the overall average force of palpation. It does not include details regarding the texture or local stiffness of the tissue. If kinaesthetic feedback alone is available, there is a reduction in the number of injuries caused during the grasping of tissue [4]. Laparoscopic

[1] By passing the instrument shaft through the thoracic cavity, the fulcrum at the entry point causes the tip motion to be reversed from the handle. Moving the instrument handle up moves the tip down, moving the handle right moves the tip left, and vice versa.

[2] A trocar is a device used to create a passage for minimally invasive instruments from the outside to the inside of a body.

devices[3] that include kinaesthetic feedback operate by either conveying the total average force on the instrument end effector with haptic feedback to the surgeon, or by displaying the bulk force in a visual manner. A short list of techniques that may be used to measure kinaesthetic information include force sensing resistors, strain gauges, and the measurement of current supplied to a motor that controls the palpating jaws of a grasper [5–7].

1.3.2 Tactile Feedback

Tactile information provides insight on the tissue texture and local stiffness as if felt with a finger, thus making it suitable for palpation. Commonly in MIS applications, tactile feedback pertains to the pressure map of a localized region. Tactile feedback is inherently more complicated than kinaesthetic feedback since it requires an array of sensing elements to determine pressures and forces over a small area. The benefit is that more information can be collected about the tissue in contact with the sensor and nonlinearities caused by indirect force measurement may be eliminated [8]. Suitable incorporation of tactile feedback is still an area of active research. Many researchers have attempted to make tactile sensors for MIS tumour localization. They make use of piezoelectric sensors, resistive sensors, current sensors, optical sensors, and thin film sensors [9–12]. Some researchers use capacitive array sensors produced by Pressure Profile Systems Inc. (PPS) [13–17]. Other researchers use tactile sensors to determine the best way to display kinaesthetic and tactile information rather than assessing the sensor performance [7, 15, 17]. Current research has shown that displaying visual feedback on the operating room screen and combining it with haptic feedback increases the chances of localizing a tumour.

1.3.3 Ultrasound Feedback

Ultrasound is a method used to detect the presence of a tumour in most parts of the body. However, a radiologist is often required in the operating room to properly assess the ultrasound images. Furthermore, the use of ultrasound in the lung requires the lung to be fully collapsed to prevent artifacts in the ultrasound signal. Using ultrasound alone, it is difficult to identify the

[3] A medical instrument that is inserted through the abdominal wall for examining or performing surgery in the abdominal cavity.

location of small tumours, roughly 10 mm or less in diameter.

In the design of a new minimally invasive instrument, the goals are to improve the surgical procedure by reducing the operation time, and to design an intuitive device similar to standard surgical devices to reduce the amount of training necessary.

1.4 Project Goals

It is expected that, by using common sensing modalities such as tactile, kinaesthetic, and ultrasound, in combination with haptic and visual feedback, the surgeon's natural perceptions during MIS can be mimicked.

To reach this goal, the development of a hand held laparoscopic minimally invasive tumour localization device using multiple sensing modalities with haptic feedback and an intuitive display of information was undertaken. The goal was to locate tumours through a process of data fusion, combining tactile, kinaesthetic and ultrasound information in a manner that is easily understandable and does not necessarily require a radiologist on site. This project includes the design of a minimally invasive instrument suitable for future incorporation of a semi-automatic tumour detection strategy using feedback from a plurality of sensors to assist in the palpation of tissue, optimizing the palpation force and orientation. The device has two degrees of freedom to increase the articulation of the instrument. The device jaws and subsequent linkages made room for the inclusion of multiple sensing modalities to reduce false positive and false negative findings. The proposed device is shown in Figure 1.1, pointing out key components that will be discussed in detail: the end effector (or grasper) and the motor housing. The grasper is the component that manipulates and palpates the lung tissue. It is designed to hold both tactile, ultrasound, and kinaesthetic sensors. The motor housing holds the motors used to actuate the grasper, routes sensor and mechanical cabling, and is attached to the handle.

1.5 Challenges

To advance the lung tumour localization methods for MIS, the device shown in Figure 1.1 was developed. The final prototype is shown in Figure 1.2. The device can make use of multiple

sensing modalities for palpation information feedback and also gives the surgeon the ability to manipulate the lung in the same manner as a standard surgical grasper. The major challenge in the development of the device was the size constraint — a 12 mm diameter hole that the instrument had to pass through. Constraints caused by the addition of two degrees of freedom included making space for ultrasound and tactile sensors in the instrument jaws, and making space for sensor cabling along mechanical linkages and down the instrument shaft.

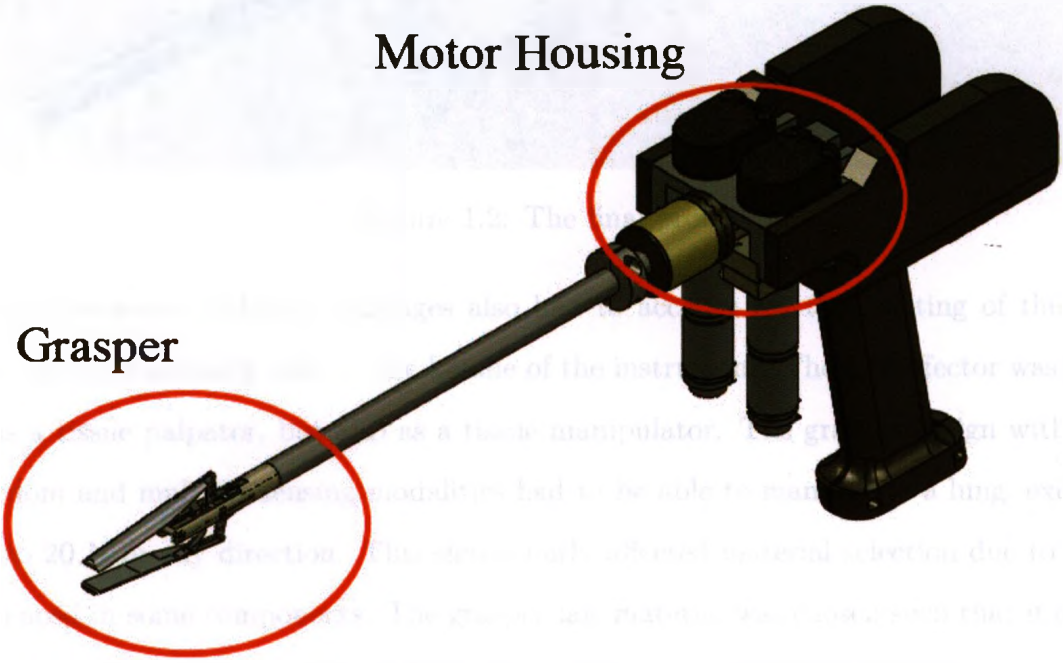

Figure 1.1: Proposed design of a minimally invasive lung tumour localization instrument.

The overall space constraints lead to the use of thinner mechanical linkages, making it important to analyze components for a robust final prototype. Incorporating two degrees of freedom while allowing room for sensor cabling necessitated small sized components, increasing their stress under load. In addition, a high factor of safety was required since the device is intended for use inside a human body. Any failure could increase the risk of patient injury, and lead to the cancelation of minimally invasive surgery and a switch to an open thoracic surgery.

The tungsten cables used for actuation of the grasper jaws had to be carefully placed to make

Figure 1.2: The final prototype.

room for the sensor cabling. Linkages also had to account for the twisting of the end effector relative to the stationary base — the handle of the instrument. The end effector was designed not only as a tissue palpator, but also as a tissue manipulator. The grasper design with two degrees of freedom and multiple sensing modalities had to be able to manipulate a lung, exerting a force of up to 20 N in any direction. This significantly affected material selection due to high stresses experienced in some components. The grasper jaw material was chosen such that it could be heat treated to attain a higher yield strength, increasing the device factor of safety.

1.5.1 Contributions

To date, no multi-modal, multi-degree of freedom (DOF), minimally invasive semi-automatic lung tumour localization devices, including kinaesthetic, tactile, and ultrasound sensing, have been developed. The proposed device has three major innovations.

1. No researchers to date have developed a multi-modal minimally invasive lung tumour localization device. The proposed design can accommodate two imaging sensors, ultrasound and tactile, as well as kinaesthetic sensors. As grounds for future research, a process of data fusion between the plurality of sensors is hypothesized to increase the likelihood of localizing a tumour. This would

also relay more information to the surgeon as compared to other minimally invasive instruments.

2. As a novel mechanical feature, the design makes use of two degrees of freedom in the instrument end effector. The use of two degrees of freedom allows for a wide variety of tissue geometries to be palpated. Additionally, the end effector can be adjusted to use a large portion of the imaging sensor surfaces. Lastly, a more controlled palpation can be achieved on lung tissue, preventing permanent damage.

3. No researchers have developed a real-time mechatronics-assisted force feedback palpation procedure for tumour localization, a feature that can be beneficial [18]. Tholey et al. developed an open-loop automatic grasping function for a kinaesthetic sensor based grasping mechanism to eliminate variability in the results [19]. The experiments used equally-sized tissue phantoms that were palpated for exactly 10 seconds in the same physical manner each time. The design presented in this thesis includes a demonstrative semi-automatic force feedback palpation function to help detect tumours in real-time. This will optimize the applied force during palpation, optimize sensor contact with the tissue, and prevent tissue damage. The incorporation of two degrees of freedom in the grasper jaws helps to provide this capability.

1.6 Organization of Thesis

This thesis is divided into six chapters that progress through the design, analysis and component selection, control, and validation of the presented device. A description of each chapter follows:

Chapter 1 — Introduction

This chapter outlines the motivation and goals behind this work. It identifies important restrictions in current techniques and past technologies for lung tumour localization. It also describes design parameters and points out the contributions of this work.

Chapter 2 — Literature Review

This chapter summarizes similar or related research in the field of lung tumour localization. It reviews existing and emerging technologies in regards to sensing and mechanical systems. The literature is presented in the order of increasing system complexity, starting

with simple axially palpating rods using kinaesthetic feedback, followed by radially palpating or grasping mechanisms with kinaesthetic feedback. Subsequently, tactile sensing is introduced. This section introduces the reader to current tactile sensor technologies and existing commercial tactile sensors. Multi-modal devices are then presented, particularly those that use multiple tactile sensors, multiple ultrasound sensors, and a combination of both. The important contributions for each sensor modality are pointed out, concentrating on the fact that multi-modal systems are of great interest because of their increased performance in tumour detection. Throughout the literature review, existing mechanical designs are presented and their strengths and weaknesses pointed out.

Chapter 3 — Design and Analysis

This is the most comprehensive chapter, covering the majority of work undertaken. It covers particular design constraints and requirements, the mechanisms of motion for the designed mechanical lung palpator, its materials, its sub-components, and its limitations.

A significant portion of this chapter is dedicated to the results obtained from finite element analyses (FEA) of the palpator mechanism. Here it is demonstrated that the device will not experience failure under the considered loads in a variety of different physical configurations. In particular, mechanical linkages and joint forces are analyzed. Using the FEA results, conclusions were drawn on what type of material should be used.

As a result of analyses concluding high material stresses, a heat treatment procedure for alloy 440C stainless steel is presented. The effects of the heat treating process on the steel alloy are tested and reviewed. Comparing the difference between heat treated and untreated steel also simultaneously validates the use of the chosen pins for the linkage joints. Next, a different palpator jaw geometry is introduced for integrating the ultrasound sensor. FEA results show the geometry requires heat treated steel to increase its factor of safety from 1 to 4.

Discussion of the palpator mechanism is followed by a review of the sub-systems. This includes the mechanisms of movement of the jaws with two degrees of freedom. It also includes explanations of the added functionality of twisting the palpator jaw over a 180°

range. Selected components are described including the chosen materials, motors and motor controllers, optical encoders to assess system performance, cable selection and integration, and strain gauge selection for kinaesthetic feedback information.

Chapter 4 — Electronics and Control System

This chapter introduces the associated electronics and control system required to drive the palpator movement. Kinematic equations are first derived, explaining their use in reality and in modelling the system. The desired output variables are described and a path generating algorithm is presented (a continuous point-to-point trajectory). With the possibility that the implemented control system could request movement of the palpator jaws to a geometrically impossible position, a method is designed to move the jaws as close as possible to the desired position. A kinematic model is then presented in MATLAB, describing the movement of the device and chosen path generation scheme.

A large scale mock design is then presented implementing two force sensing resistors (FSR) as feedback inputs. A control system is designed as a proof of concept with FSRs since the tactile sensor was not integrated into the current version of the prototype. Qualitative results are discussed, including limitations of the palpator design.

Chapter 5 — Validation of the Final Prototype

In this chapter, the final prototype is presented and discussed. The positional capability of the jaws are compared to the computer model, and an experiment is designed to validate the performance of the device as compared to the FEA cases previously run. The control system discussed in Chapter 4 is implemented and qualitatively assessed. The strengths and limitations of the design are discussed.

Chapter 6 — Conclusions

This chapter summarizes the work presented in this thesis and offers recommendations for future work.

Chapter 2

Literature Review

Presented in this chapter is an overview of devices developed for tumour localization, beginning with the most simplistic designs and feedback methods, moving through more complicated tactile and ultrasound sensor integration. Comments on mechanical design are made when appropriate.

2.1 Kinaesthetic Instruments

The easiest form of feedback is kinaesthetic, since it only deals with bulk forces. Many researchers [5–8, 11, 14, 19–26] have attempted to use simple nodule[1] localizing instruments using kinaesthetic feedback alone. For such applications, sensors were usually mounted along the instrument, and not in direct contact with the area of palpation. Palpation induces deformation within the instrument. These deformations can be used to extrapolate the bulk force on the instrument end effector. This is a method of indirect sensing [8].

2.1.1 Axially Palpating Instruments

The simplest palpation device is an axially palpating rod integrated with a sensor to determine the force of palpation. Using such a device, a study was conducted to determine safe palpation forces for minimally invasive instruments and their effect on sensor selection [21]. The conclusion drawn was that minimally invasive sensors should be able to sense 0–10 N with a resolution of

[1] A small round lump.

0.01 N. The sensor range was based on a peak palpation force of 1.6 N, and the sensor resolution was deemed to be one order of magnitude less than the smallest sensor variation. This closely corresponded to the commonly accepted 0.1–11 N sensor range requirement [27]. An additional experiment tested the most effective probe shape on the distal end of a cylindrical 9 mm diameter tool when palpating axially. A flat ended design performed much better than a curved one, while instruments with a larger palpation area or smaller palpation area than the suspected tumour performed equally well. This was likely due to less lateral movement of the underlying tumour.

The authors of [28] constructed a similar device to measure the elasticity of soft tissue. A force sensing resistor was used to determine the axial force that a probe exerted during the palpation of a tissue. Results from the constructed device and from an industrial elasticity measuring machine (Zwick/Roell Company, Ulm, Germany) were comparable.

Hosseini et al. [5] studied the behaviour of a breast tumour under palpation. Finite element analysis was first used to determine the pressure on tissue with an underlying tumour undergoing palpation. Experimental results on phantom tissue closely matched the findings of the finite element model. The resulting information could be used to design more advanced instruments.

In an attempt to improve the function of an axially palpating instrument, a minimally invasive probe with a wheel on the distal end for rolling over tissue was developed [20]. A force sensing resistor was used to sense the axial force exerted on the device during palpation. By rolling the end effector over a tissue in several passes, a two-dimensional force map could be created to localize areas with underlying stiffness.

In another design, deformation of a laparoscopic palpation device instrumented with three optical fibres at its tip was studied [25]. The fibres were safely embedded in the instrument shaft. Its working resolution was 0.01 N, with a maximum force of 2.5 N. This type of design could prove useful in palpation applications due to its appropriate sensing resolution and small 5 mm diameter.

Takashima et al. [22] also tried to improve an axially palpating probe by using an infrared filter and image processing algorithms in combination with an endoscopic camera. The data acquisition was slow, operating at 5 Hz. Furthermore the device was not robust in that it had to be separately calibrated for use in air, in the body, or any other media. Additionally, there were many sources of noise. Predicting and eliminating noise was time consuming and contributed to the low sampling

frequency.

Unlike breast palpations which have a stiff rib cage to palpate against, axial palpation of lung tumours is more difficult since the lung cannot always be palpated against the chest wall. Furthermore, the shape of the palpating device may change the results significantly [21]. For this reason, the majority of researchers have developed grasping type designs in an attempt to improve system performance.

2.1.2 Grasping Instruments

Bicchi et al. [8] modified a Babcock grasper to include kinaesthetic feedback. A first experiment determined that there was a loss of sensation using traditional minimally invasive devices. For simplicity, the modified Babcock grasper used a strain gauge mounted near its handle to sense the grasping force. The position of the sensor increased nonlinear friction and backlash effects. A second experiment was conducted to determine whether material properties could be characterized with force feedback.

A grasping device with tri-directional force sensing capability was constructed by [19]. It was used with two piezoresistive sensors for measuring lateral forces at the grasper, and a thin-film force sensor for normal force sensing. With the plurality of force sensors, the shear force on the tissue could be determined. The advantages of having shear force sensing capabilities include detecting tumours while sliding over a tissue sample, and providing the ability to palpate the instrument against tissue in an axial direction with the grasper jaws closed. The sensors were placed as close as possible to the jaws of the instrument to reduce nonlinear effects. The validity of force sensing was determined by comparing the force sensor measurements to the measured current drawn by the motor controlling the jaws. Both sensing means showed comparable final static forces, but significantly different dynamic forces. A thin-film sensor was used to measure the normal force of grasping. A disadvantage of the sensor in this device was that a force had to be applied to the centre of it. An automatic grasping function for instrument validation was used to reduce variability between results. The experiments used equally sized tissue phantoms that were grasped for 10 seconds in the same physical manner each time. Although simple and only used for validation, this open loop control system is one of the few devices that includes an automatic

grasping function. Future design plans were to include haptic feedback.

2.1.3 Inclusion of Feedback

Dargahi et al. [6] also included kinaesthetic feedback using strain gauge sensors on a modified Babcock grasper. The strain gauges were mounted to the back of the grasper jaws, reducing nonlinearities. Finite element analysis determined the required working range of the strain gauges for sensor selection. This simple and compact design also included an array of light emitting diodes (LEDs) near the handle of the instrument that sequentially lit up with increasing grasping force. This allowed a qualitative indication of the grasping force to be relayed to the user visually.

The researchers in [23] and [24] conducted comparative tests between a standard laparoscopic grasper, a custom sensorized laparoscopic grasper, and a gloved finger to determine their relative grasping performance. The end effector of the custom device was controlled electronically by the user through a master–slave system. The position of the grasper jaws was known from an optical encoder. Due to a weak actuator, the force feedback system was based on the position error of the grasper jaws. It is noted that mechanically limiting the grasping force prevents the use of the device in different situations, such as manipulating tissue. The main innovation in this design was the use of simple haptic feedback in the master controller module. The force felt by the grasper was translated to the hand of the user controlling the device handle. No other forms of feedback were used. The sensorized instrument significantly improved tumour detection over using the same instrument with no feedback, however, palpation with a gloved finger produced superior results.

In another design, haptic feedback was provided to an endoscopic grasper [29]. The design was more general purpose however, including force amplification to the end effector grasper for uses such as the ligation of vessels and severing tissue. It was not specifically designed for sensitive environments like lung tissue palpation.

Hu et al. [26] developed a robot assisted master slave grasper with haptic feedback displayed on a PHANToM (Sensable Technologies, Woburn, MA). The goal was to make a system in which a surgeon could tele-operate a grasping device and feel what was being grasped by it. Strain gauges were used to sense the force of grasping in the instrument grasper. Experiments proved that strain gauges were suitable to determine the tissue stiffness, and that stiffness could be determined using

only haptic feedback. When determining the effectiveness of haptic feedback alone, two people out of a ten person group were not able to properly assess the tissue stiffness, suggesting the need for device training. The experiments were performed with one person operating the grasping device, and another person operating the PHANToM. This combination was of course unrealistic and could have both eliminated and added undesirable side effects in tumour detection performance.

To determine the best type of information to relay to a surgeon during a minimally invasive force feedback procedure, a study was done comparing visual force feedback, kinaesthetic force feedback, and a combination of both [7]. The combination of feedback methods outperformed both single feedback methods. Individually, visual feedback outperformed kinaesthetic feedback. These experiments utilized a custom tele-operated system with a PHANToM for kinaesthetic feedback and motor current sensing for grasping force measurement. A major design consideration was the use of cable driven mechanisms to reduce backlash in the end effector.

The main drawbacks of kinaesthetic feedback are the nonlinear effects due to indirect sensing, the ability to only sense bulk force, and the lack of tactile perception. Tactile sensors inherently solve mechanical nonlinearities such as friction by being in direct contact with tissue and also eliminate calibration processes that need to be undertaken for a variety of grasper positions and shapes. Tactile sensing can also determine the underlying shape of the palpated tissue. For example, tactile sensing could differentiate a bronchial tube from a tumour. Furthermore, tactile sensors provide the ability to palpate tissue. Kinaesthetic sensors can only sense grasping force, which does not directly translate to tissue stiffness.

2.2 Tactile Instruments

Tactile information is a combination of tissue stiffness and texture. Often, pressure data is used to display tactile information. Many researchers [9–15, 17, 18, 30–33] have tried to use existing or newly developed tactile sensors with different feedback methods to help detect tumours. Unlike kinaesthetic sensors, tactile sensors do not suffer from mechanical nonlinearities because the sensor is in direct contact with the palpated tissue. Types of tactile sensors include optical emitter/detector pairs, elastomer based, capacitive, piezoresistive, current sensing arrays, and polyvinylidene flu-

oride (PVDF) films. However, not all of these sensors can be used for MIS. Since an area of the tissue can be sensed, tactile sensors are often used for palpation to determine different tissue characteristics, in addition to grasping tissue with an upper bound force to prevent tissue damage.

Tactile sensors are more complicated to manufacture and incorporate into a minimally invasive device because they require many sensing elements within a small area. Still, the advantage of relaying more information about the tissue often outweighs the added complexity.

2.2.1 Types of Sensors

Dargahi et al. [12] developed a scissor-like minimally invasive grasping instrument using PVDF as the sensing medium with four sensing elements. Validation of the instrument was done by comparing the actual sensor output to FEA simulations. The sensor was constructed in layers beginning with four individual upper PVDF electrodes placed in a line, followed by a large PVDF film to cover them all, followed by a large lower PVDF electrode. The sensor could measure loads in four locations along the length of the sensor making it a one-dimensional (1D) tactile sensor. The sensor was placed on the jaws of a surgical grasper. The use of only four sensing elements made the design compact, robust, and inexpensive. However, 1D sensors have severe limitations. The ability to sense in two dimensions proves beneficial for obtaining a topographical pressure map without having to sweep the sensor over a region.

Based on piezoresistive material, a tactile sensor was developed for 1D and two-dimensional (2D) sensing in [31]. A single element was composed of a piezoresistor sandwiched between two conductive tracks. Applying a force to the sensor would decrease its resistance. Tests performed on artificial bowels validated the sensor. Though the prototype was not designed for MIS, the sensor was inexpensive and could be miniaturized to make it suitable for MIS.

Pawluk et al. [33] described a high sensitivity pressure distribution sensor able to replace a human finger. The design used several perpendicular copper strips separated by thin pieces of a silicone dielectric. Increasing pressure on the crossings of the array brought the copper strips closer together, reducing their capacitance. The change in capacitance was closely proportional to the change in applied pressure. This sensor forms the basis for a commercial sensor offered by Pressure Profile Systems, Inc. (PPS).

Two elastomer-based tactile sensors were reviewed for their suitability in a tactile sensor [30]. In one type, carbon or silver was embedded within rubber, such that compression of the rubber caused a local increase in the concentration of the embedded media, thereby increasing the conductivity. The resulting sensor had a few millimetres of spatial resolution. Eltaib et al. [30] also tested a similar sensor to Pawluk [33]. The problems associated with the sensor were noise, hysteresis, creep, and crosstalk. Furthermore, the properties of the rubber layer limited the dynamic range of the sensor, and connecting to a conductive rubber was a source of noise on its own.

Dollar et al. [11] discussed the use of optical reflectance for tactile sensors. With the use of an LED and a photodetector mounted within a casing, deformation of the casing caused a change in the amount of light the detector received, thereby changing the current through the detector. This sensor used inexpensive components but was too large for MIS.

Schostek et al. [10] developed a sensor that was constructed in three layers. The first layer was an array of spherical conductor electrodes, the second layer was a thin conductive film, and the third layer was a copper film. With an applied force, the current passing through the electrodes changed. Similar to PPS sensors, the medium between opposing layers was air. Unlike PPS sensors, this sensor was entirely encased, making it waterproof. It proved to have a large 0–60 N operating range with a 1.4 mm spatial resolution, comparable to a human finger.

A slightly different approach used by Sedaghati et al. [32] was the development of a piezoelectric tactile sensor for use in MIS that measured tissue compliance. A single tactile element was composed of an inner cylinder made of rubber surrounded by a concentric compliant outer cylinder made of softer rubber. A circular piece of PVDF film was placed under the inner cylinder, sized to the same diameter. The assembly was then mounted to two rigid plates separated by PVDF film. The two sets of film allowed for force sensing on a particular element of the array and the overall force on the sensed object, providing a combination of tactile and kinaesthetic information. The problem with the sensor was its size. The size of the prototype was not suitable for MIS, and if constructed smaller, the sensing elements become easy to damage, especially with sliding palpation motions.

A commercially available PPS tactile sensor was used to determine its capability to produce a pressure profile of a tissue using several palpations [18]. Experiments were conducted to pal-

pate tumour embedded ex vivo porcine lung tissue manually, and with robotic assistance. Under robotics-assisted palpation, the maximum pressure of palpation decreased by 35% and increased successful tumour localization by 50% over manual palpation. The optimal force application with robotics-assisted palpation was found to be 4 N with a sensor area of about 240 mm^2. This suggests manual palpation would benefit from mechatronic assistance.

Ottermo et al. [15] conducted a tumour palpation study to compare the relative performances between a gloved finger, a standard laparoscopic instrument, and a custom designed laparoscopic instrument fitted with a PPS sensor. It was found that the sensorized instrument did not perform better than the standard instrument when differentiating hardness and size of tumour phantoms. The gloved finger was not significantly better than the sensorized instrument when judging the hardness of a tumour. The findings suggest that the visual feedback form used was not intuitive, or that it was not an ideal way of representing the tactile sensor information. It was suggested that the tactile information display should be on the same screen as the endoscopic video feed.

2.2.2 Mechanical Designs

An instrument designed by Miller et al. [14] using a PPS sensor featured tactile information overlaid on the endoscopic video screen. The method of tactile information display proved to be very intuitive. To map the sensor readings to the tissue on the screen, optical tracking of LEDs mounted to the palpation probe was used. The tactile sensor was mounted on a cylindrical shaft which had one degree of freedom (DOF) — a rotational joint controlled by a knob, allowing for a wider range of palpation angles. Validation experiments on foam lung phantoms embedded with phantom tumours determined that the device could detect tumours better and faster than a sensorless rigid probe. However, the device did not have the ability to grasp tissue. The experiments were performed with tissue on a rigid surface.

The authors of [34] used an ultrasound probe mounted on the distal end of an endoscopic instrument, attached to a parallelogram style joint. This added DOF allowed the ultrasound probe to be moved up and down without having to rotate the endoscope about the fulcrum at the trocar, which would change the apparent angle of the surface to palpate.

In another attempt to add articulation to MIS, a device was designed to mimic the kinaesthetic

movement of a surgeon's bent or extended finger as a 1 DOF system using two joints and a cable driven mechanism requiring no electrical power [35]. This mechanism was developed to regain the same movements a surgeon would use in open thoracoscopic surgery.

For the purpose of cutting tissue, a hand held endoscopic system was designed with grasper like jaws [36]. The articulation of the device was similar to that developed by Miller [14] in that it had an extra joint, but this system had a grasper as an end effector.

Also similar to Miller [14], a device was made that used no rigid backing when palpating [37]. It did however use two flat tactile sensors. The tactile sensors were hinged on the distal end of the instrument shaft and were able to open and close, similar to a grasper, but without coupled jaw movement. By knowing the angle of the sensors relative to the shaft, tumour location could be determined. This method of sensing helped align the instrument shaft with a tumour, making a biopsy easier. The device was not designed specifically for tumour localization. However, obvious parallels can be drawn for lung tumour localization using a similar device.

2.2.3 Combining Technologies

Feller et al. [13] used a PPS capacitive tactile sensor using haptics to provide the sensation of palpation onto the user's finger. An array of densely packed vertically moving pins was constructed such that the displacement of the individual pins was proportional to the sensed tactile pressure. The design was targeted towards remote breast and liver palpations and was never intended for MIS. One experiment was conducted by mounting the sensor on a robotic arm, tele-operated by one hand through a PHANToM, while the other hand felt the haptic tactile array with one finger. Another experiment was performed by controlling the sensor by hand, while feeling the haptic tactile array with the other. Each experiment used the same phantom tumour model, ranking three levels of tumour stiffness. Both methods were equally accurate in tumour detection. In the tele-operated case, the applied force was significantly lower than the direct palpation case, but also took 150% longer than the hand controlled case. The force feedback gain was varied to improve tumour detection, but proved to have no effect.

Using the haptic tactile feedback array to mimic tissue stiffness may have been sufficient, but a combination of kinaesthetic and tactile feedback are necessary to properly represent touch [18]. In

fact, the quality of tactile data is dependent on the applied force, and the performance in tumour detection depends on how consistent the force is. This suggest that automatically controlled palpation would increase the likelihood of detecting a tumour.

Ottermo et al. [9] developed a remote palpation device that included a 30 element piezoelectric tactile sensor and a haptic tactile array. The device was remotely controlled and was designed to have the haptic feedback array attached to the controlling arm of the device. This eliminated the use of two hands to control and feel, as was required by Feller's [13] device. In trying to mimic the resolution of a human finger, the haptic array consisted of 3×10 micro motors placed at 2 mm increments, the smallest two point discrimination distance of a finger tip [38]. The design implemented a silicon rubber film over the tactile sensor for low pass filtering as described in [39]. Rounded edges of the tactile sensor reduced edge effects.

Using a similar haptic tactile display, a study was conducted to examine the effect of different algorithms for haptic tactile sensor display [17]. A test was set up to observe the effect of using the raw tactile sensor information and subtracting a fixed pressure value, and subtracting a pressure value that was linearly dependent on the applied force. The sets of sensor data were displayed on the haptic tactile array. The tests were performed on several different tissue phantom models. The fixed pressure subtraction value was unique to each tumour model. Therefore, calibration was necessary for every type of palpation medium. However, the algorithm significantly improved tumour localization and decreased the exploration time. Subtracting a pressure value proportional to the applied force further improved localization while keeping the exploration time the same. Tumour localization error was reduced by 37%, the required time to find the tumour was reduced by 44%, but the maximum force increased by 7% from the case of no pressure value subtraction. This suggests that it is necessary to display the tactile information differently from the raw sensor information for more intuitive results. It also may suggest that the improved performance was due to a higher palpation force.

2.2.4 Multiple Modalities

Hyung et al. [40] documented tumour localization for submucosal tumours using two different ultrasound devices. Tumours were successfully removed in two human cases after first localizing

them with endoscopic and laparoscopic ultrasound. Ultrasound was used because the tumours were too deep to be palpated. This procedure proves that multiple sensing modalities could help localize a region of interest. Although it was not minimally invasive and was done on non-palpable tissue, it still justifies the use of multiple sensing modalities to detect lung tumours.

In fact, a multi-modal device for tele-operative breast examinations was constructed [41]. The device included two sensing modalities, tactile and ultrasound, and also provided haptic feedback. The tactile sensor worked on optical total internal reflection. The claim was that the system may actually outperform a physician's own hand. Though not suitable for MIS, the increased modalities are an attractive option to pursue due to the possible increase of tumour detection performance.

A similar handheld device used ultrasound and tactile pressure sensing for the primary use of palpating breast tumours [42]. The two sensors were mounted at different positions on the device and thus had different physical perspectives that needed to be accounted for by tracking their respective positions. The sensor information could be combined to determine tumour position and depth. The device also had the capability to repeat palpation in the same orientation with the same amount of force for subsequent breast examinations. This feature may be appropriate for lung tumour localization if a surgeon needed to re-explore a previously marked area of interest.

2.3 Summary and Conclusions

In the development of a minimally invasive lung tumour localization device using multiple sensing modalities, it was necessary to determine that such a solution does not yet exist. It is hypothesized that such a device could advance the performance of detecting tumours during minimally invasive surgery. The following chapters are dedicated to the design, analysis, control, and validation of the proposed system.

Most current technologies in the author's opinion are too simplistic to transfer enough information to a surgeon to help locate tumours. This includes all axially palpating sensing means, including implementations where a region of tissue could be sensed to develop a tactile map, which may consume too much time and may be difficult. 1D sensors as well require extra time to palpate a region of tissue to obtain tactile information.

Tactile sensing appears the most useful, because it transfers the most amount of information about the palpated region almost immediately. The higher the spatial resolution of a tactile sensor, the easier it is to visualize the underlying tissue, providing the ability to distinguish between tumours and bronchial tubes.

It is also shown through the literature that including multiple sensing means can increase the likelihood of tumour detection. For this reason ultrasound was chosen as a sensing means to be coupled with tactile sensing. The two sensors together should be able to provide a better understanding of the palpated tissue.

Finally, the last advancement in the presented project is the mechanical design. To reduce time and complexity of palpation without damaging tissue, a mechanical design introducing 2 DOF is constructed. This mechanism completely redefines the act of palpating, allowing robotics-assisted functionality to be added to standard human controlled palpation. This optimizes the palpation for varying tissue sections and can enforce a safe limit on the maximum palpable force, preventing damage to the tissue.

Chapter 3

Design and Analysis

3.1 Introduction

The focus of the design for the hand held minimally invasive instrument was primarily on the end effector. The requirement of minimizing the overall size, forced the load bearing areas to be supported by small components, which subsequently increased the material stresses. All moving parts were designed to fold around each other to minimize frontal cross section and device stiffness was maximized by utilizing parts with a high tolerance. The design was required to support a human lung, which can exert a force of approximately 20 N. FEA results showed that the system had a factor of safety of 4 with heat treated material. FEA was an essential step in the creation of the prototype to verify performance, and to reduce the number of constructed prototypes to one. The required machining and heat treating costs to build the end effector were too high to justify a design process that included multiple machined prototypes and experimental tests for validation. Sub-systems were not analyzed in detail because preliminary calculations showed a higher factor of safety than the end effector. These sub-systems included the motor housing, tensioning mechanism, actuating mechanisms and handle.

The design process of the end effector was iterative, and was mostly concerned with the development of different mechanisms of movement. Initially based off of a Babcock grasper, five different designs were modelled using SolidWorks 2010, three of which were rapid prototyped and assembled to have a better physical understanding of the weak areas of the design. The fundamental

difference between the final design and the Babcock grasper was the use of cable actuation rather than push/pull rods. This was intended to accommodate wrist joints for increased instrument articulation. With the final concept chosen, FEA was used to determine the required material properties, which changed some of the design features, but maintained the overall structure of the mechanism.

3.2 Design Requirements

The main requirements that guided the design process were fitting the device through a 12 mm diameter tube, using a cable driven mechanism, including the ability to manipulate a lung and palpate varying lung shapes, to use multiple sensing modalities (kinaesthetic, tactile, and ultrasound), and to obtain repeatable results. Future work includes enhancing the performance of the end effector by using an intuitive control system, and adding functionality such as robotics-assisted palpation, visual and haptic feedback.

The dimensions of the end effector and total instrument length were modelled after an Ethicon Echelon Flex 60 articulating linear cutter (Figure 3.1) following a recommendation from an expert[1] in the field of minimally invasive thoracosopic surgery (MITS). As such, the entire instrument had to fit through a 12 mm diameter trocar (Figure 3.2), and the jaws with which to palpate the lung had to be 90 mm long.

The use of a cable driven mechanism was desired for integration of wrist joints for more degrees of freedom and better positional flexibility. However, wrist joints were not included in the final design to increase its robustness and factor of safety (FOS). Additionally, removing wrist joints reduced the complexity of control systems, subsequently improving intuitive human control of the end effector. It also provided more space for sensor cable routing, and reduced possible undesired effects of bending sensor cables. Furthermore, removal of additional DOF reduced the total length of the end effector making it suitable to use in a wider spectrum of chest cavity sizes. The use of actuating cables saved space compared to alternative actuation means, such as a push/pull rod configuration.

[1]Dr. Richard Malthaner MD, Division of Thoracic Surgery and the Department of Epidemiology & Biostatistics, London Health Sciences Centre.

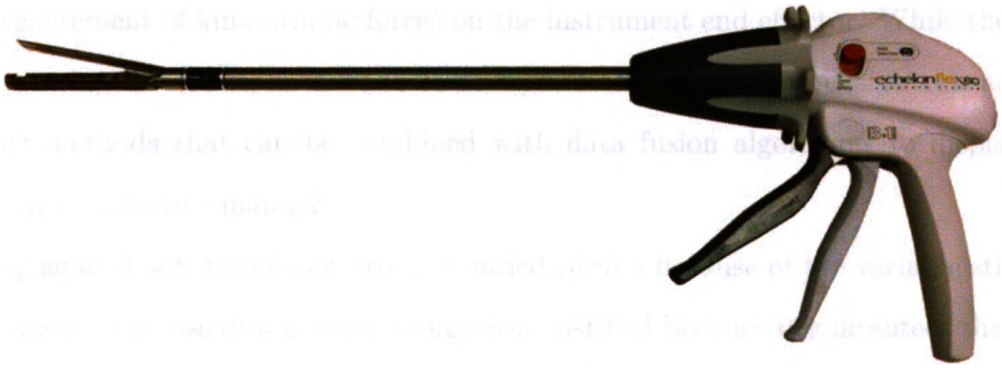

Figure 3.1: Ethicon Echelon Flex 60 Articulating Linear Cutter.

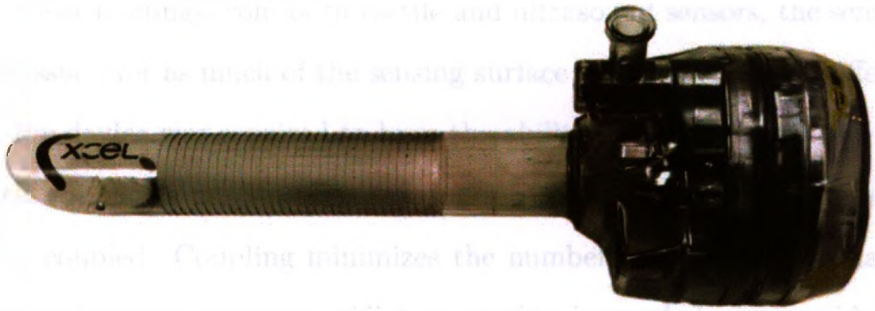

Figure 3.2: A trocar is a device used to create a passage for minimally invasive instruments from the outside to the inside of a body.

The maximum design load of the device was the force required to manipulate a human lung. Designed for the worst case scenario of lifting the entire lung, a 20 N force on the jaws of the end effector was used. This was deemed sufficient since the entire lung is not manoeuvred all at once, rather sections of it at a time, lessening the total load on the jaws. Dynamic load cases were not considered because the device would be used in a quasi-static manner.

In order to increase the probability of detecting a tumour, avoid damaging tissue, reduce the time of surgery, and attempt to restore the surgeon's natural perceptions during surgery, the inclusion of kinaesthetic, tactile, and ultrasound sensing modalities were incorporated into the design. The actuating mechanisms were designed around the most voluminous cabling, which was connected to the tactile sensor. All components were designed to allow a cable of 2.5 $\times$ 5 mm cross-sectional area to pass through the length of the device. The ultrasound cabling required less room than the tactile sensor in terms of thickness, possibly allowing for stronger linkages, but the actuating mechanisms were designed to maintain symmetry. Strain gauges were introduced for

accurate measurement of kinaesthetic forces on the instrument end effector. While the integration of different sensing modalities is beyond the scope of this report, the design can accommodate three sensing methods that can be combined with data fusion algorithms to display palpation information in an intuitive manner.

Palpating against soft tissue can produce varied results because of the variable stiffness of the supporting tissue. The use of a grasper design was justified because it guarantees that the tactile sensor always palpates tissue that is supported by a rigid backing. This increases the repeatability of measurements.

For the best sensor readings from both tactile and ultrasound sensors, the sensors should be in contact with the tissue over as much of the sensing surface as possible. Since different lungs are of different shapes, the device was required to have the ability to adapt to different contact profiles. To occupy as little volume as possible while trying to conform to different lung shapes, the jaw's motions should be coupled. Coupling minimizes the number of actuating mechanisms and saves space to make room for sensor cabling. All topographical morphologies would include the jaws ability to grasp tissues of varying thickness, inline angle, and perpendicular angle (Figure 3.3). Lung tissue is flexible and conforms to the palpating surfaces, in this case two flat sensors. To limit the occupied space and to make room for sensor cabling while still maintaining the ability to conform to tissue shapes, only two degrees of freedom were included; varying thickness, and varying inline angle (Figure 3.3, left). As recommended by a MITS surgeon, the maximum palpable tissue thickness was set at 50 mm. The maximum inline angle of palpation depended on the palpation thickness, but had a range of $-21.5°$ to $69.6°$ (Figure 3.4).

Improving the utility of the grasper requires robot assisted functionality [18]. The controls would utilize the kinaesthetic, tactile and ultrasound sensors to palpate the tissue in an optimal manner without surgeon intervention. This meant the proximal end of the surgical instrument had to include motors and associated electronics to properly control the end effector, while maintaining an appropriate size to be held by an operator. Data acquired by the sensors could then be relayed back to the surgeon in the form of haptic and visual feedback. These feedback methods were not included in the project but are considered as future work.

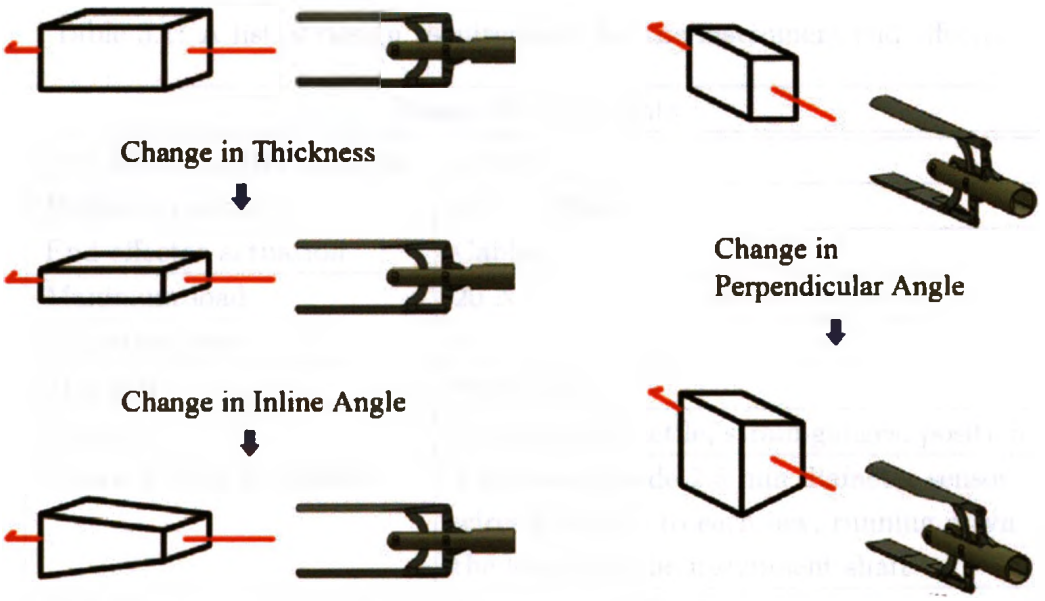

Figure 3.3: Types of lung morphologies that should be addressed by a palpation device.

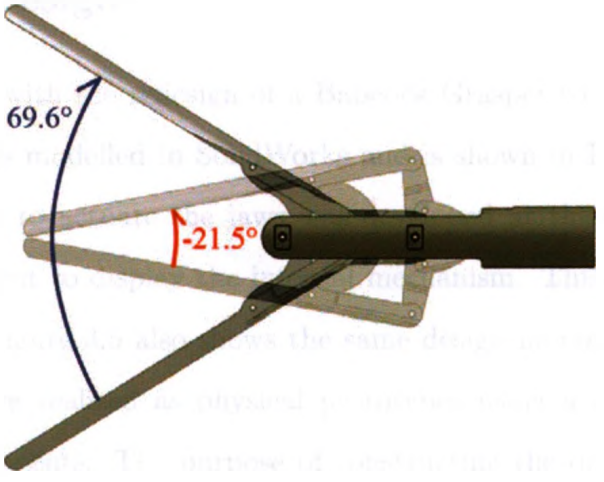

Figure 3.4: Angle range of the end effector jaws.

A summary of the design requirements can be referred to in table 3.1. Some of these requirements are discussed in later sections of this chapter.

Table 3.1: A list of design requirements for the instrument end effector.

Design Requirements	
End effector outer diameter	12 mm
Palpable geometry	50 mm thick
End effector actuation	Cables
Maximum load	20 N
Palpation force	3–5 N
Material	Sterilizable
Sensors	Ultrasound, tactile, strain gauges, position
Sensor wiring dimensions	Two side-by-side 2.5 mm diameter sensor wires mounted to each jaw, running down the length of the instrument shaft
End effector mechanism	Grasper-type design
Control	Semi-automated palpation
Actuators	Minimize weight, attain a cable tension of at least 90 N
Ergonomics	Hand held, light weight

3.3 Instrument Design

The design process began with the redesign of a Babcock Grasper to use a cable mechanism for actuation. This design was modelled in SolidWorks and is shown in Figure 3.5. The concept of using a sliding mechanism to actuate the jaws was developed at this early stage. The grasper housing is shown transparent to display the internal mechanism. This design was the first of an iterative design process. Figure 3.5 also shows the same design mounted on a wrist joint. Some of the designs created were realized as physical prototypes using a 3D printer to produce the linkage and housing components. The purpose of constructing the designs was to gain a better understanding of how the mechanism worked, find where structural weaknesses were located, and to test its ease of use. For example, it was noticed that manually positioning the end effector to a desired configuration with one or more wrist joints integrated was not possible because of cable

movement, varying cable tension, and slack in the system. For this reason and those listed in Section 3.2, wrist joints were not used in the final prototype.

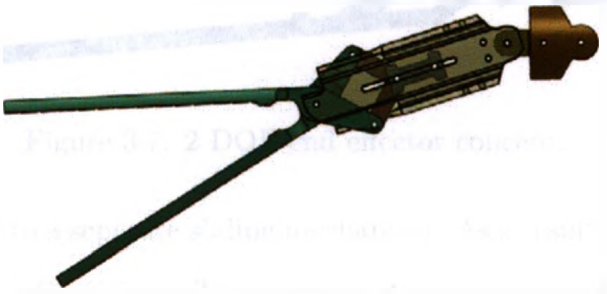

Figure 3.5: Cable actuated Babcock Grasper mechanism connected to a wrist joint.

Before the addition of a second DOF, other 1 DOF grasper concepts were developed to reduce the possible near-pivot point stress concentration on a classic scissor-like grasper design. A parallelogram four bar mechanism was designed to palpate tissue with parallel jaws (Figure 3.6), but it was noticed that the total end effector length increased, making it unsuitable for the majority of lung cavity sizes. A similar design created a virtual pivot point of the grasper jaws far behind the end effector causing the jaws to be parallel when closed and angled at 15° when fully opened.

Nearing the final design, a 2 DOF mechanism was created with slightly different linkages than that of the final prototype. Apart from geometrical differences, the design shown in Figure 3.7 has reversed applied slider forces when opening and closing the grasper jaws. This design was not chosen because the extended back linkages add to the total length of the device, making it unsuitable for use in small chest cavities.

Figure 3.6: End effector with consistently parallel jaws.

The final grasper design is a five bar mechanism designed with one horizontally sliding joint. Two degrees of freedom are incorporated by adding both the sliding joint and the means to actuate

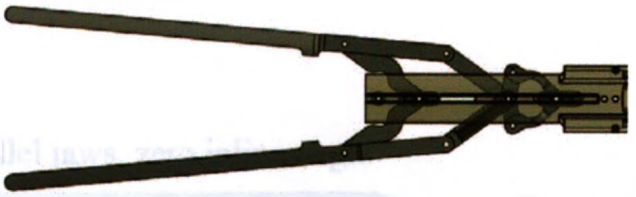

Figure 3.7: 2 DOF end effector concept.

another joint by coupling it to a separate sliding mechanism. As a result, the palpation jaws can be arranged into a wide variety of positions. The measure of palpation angle of the jaws was chosen as the angle from the lower jaw to the upper jaw (Figure 3.8). The internal mechanisms (Figure 3.9) were designed with a tolerance of 0.02 mm to reduce system slack. Figure 3.10 explains the joint naming system used in FEA simulations described later in this chapter. These joints correspond to pin locations. The pins used in the device were selected based on FEA results and experimental results. By the ISO 2338 standard, the 1 mm diameter dowel pins have a double shear strength of 700 N, 500 N higher than the highest expected load. All pin joints in the device were modelled similar to a double shear strength test, maintaining a high tolerance between linkages to avoid bending (Figure 3.11). Pin joint holes were machined to a diameter of 1.016 mm such that the pins could be slid in. Swaging was done where necessary to guarantee the pins would not slide out.

The reference system of the device is described in Figure 3.12. The same figure shows the location of the ultrasound transducer (bottom jaw) and tactile sensor (top jaw). Figure 3.13 shows the Front and Back Sliders. The sliders are controlled by motors pulling cables attached to them to actuate jaw movement. The routing of the cables through the Front Slider is shown in Figure 3.14. The blue and orange contours on the left of the figure outline where the actuating cables are terminated. The right side of the figure shows a top view of the cables routed through the slider. The Back Slider is similarly routed such that no cables interfered with each other. The tungsten actuating cable is fitted with a 304 stainless steel 1.5 mm diameter ball, with a breaking strength of 290 N, 200 N higher than the highest expected load. Tungsten was chosen because it was easy to add a swaged fitting to terminate the cable compared to non-metal cables. It also has the smallest bending radius compared to other metal cables.

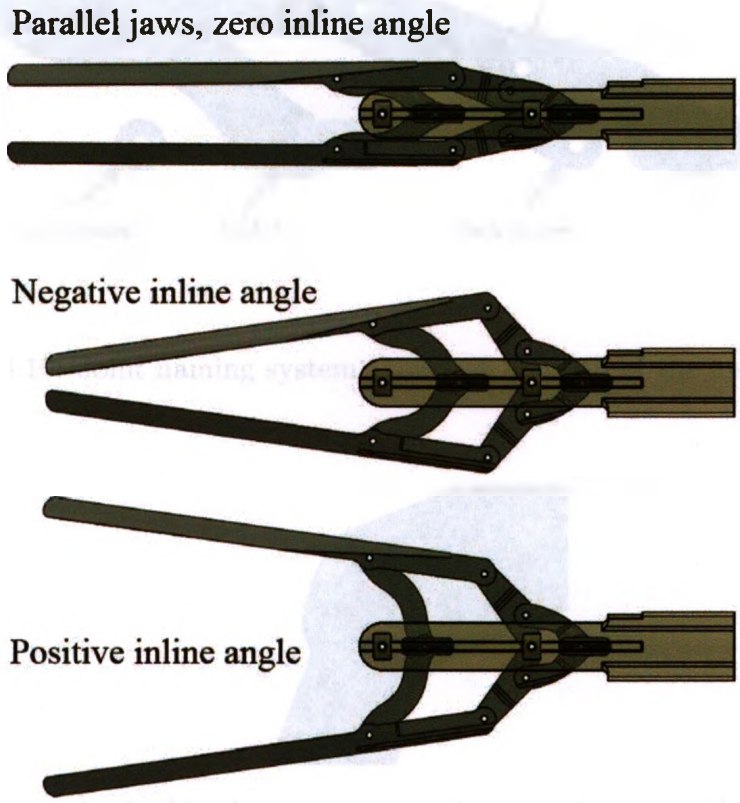

Figure 3.8: Definition of positive and negative inline angles.

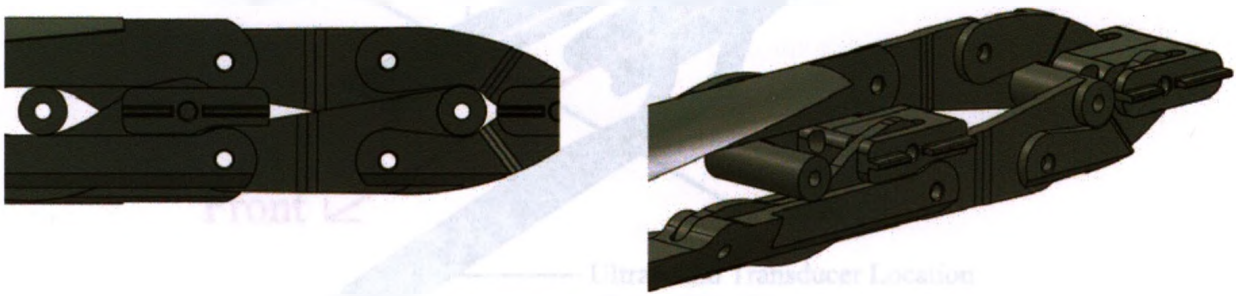

Figure 3.9: Internal components, housing not shown.

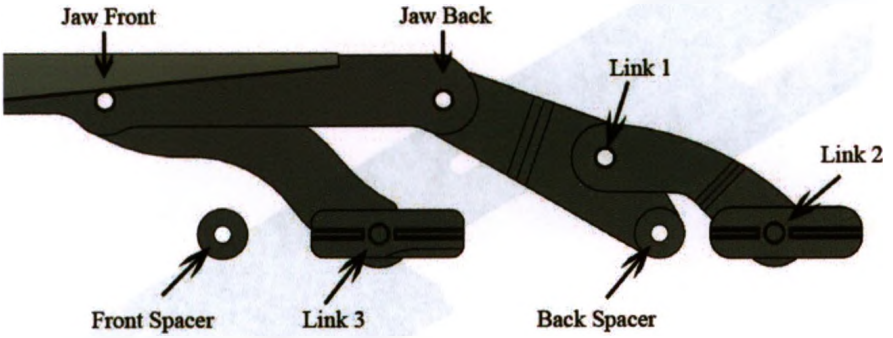

Figure 3.10: Joint naming system shown on one half of the instrument.

Figure 3.11: Joint set up in double shear to prevent bending forces on the joint pin. Jaw Back joint shown.

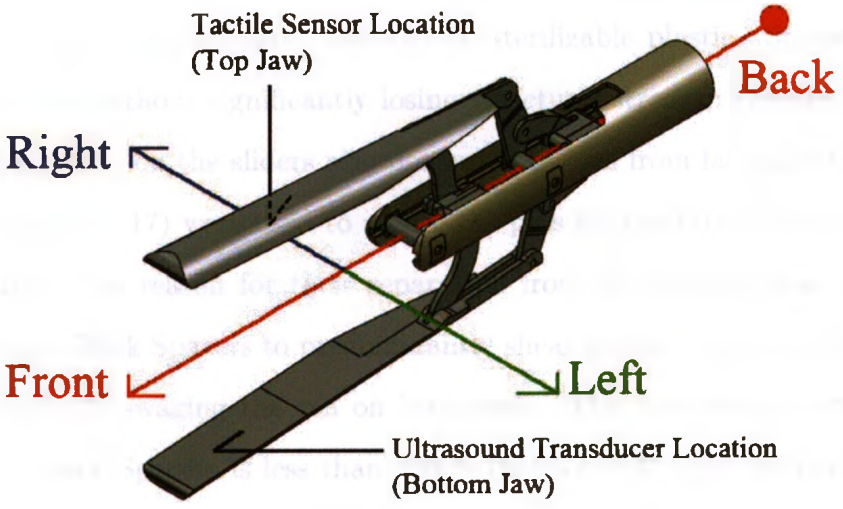

Figure 3.12: End effector reference naming system.

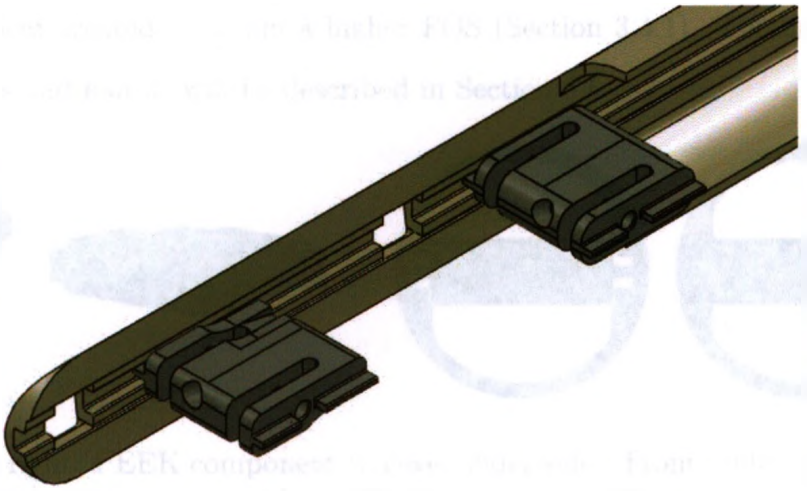

Figure 3.13: Front Slider (left) and Back Slider (right) shown in half of the grasper housing.

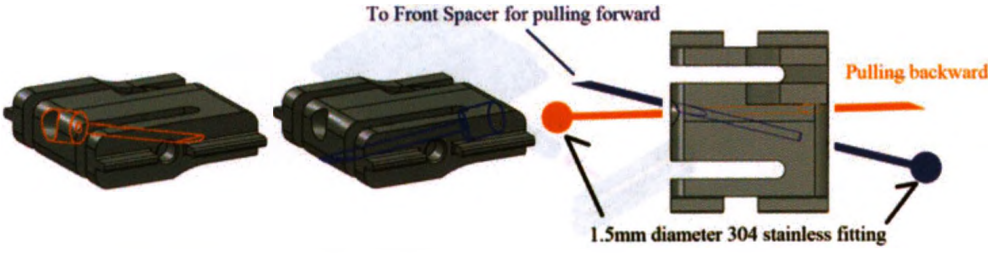

Figure 3.14: Cable routing of the Front Slider. One cable pulls the slider backwards, the other loops around joint Front Spacer (Figure 3.10) to pull the slider forward.

To ensure that the sliders move easily in the sliding rails, their sides are covered with polyether ether ketone (PEEK), a high strength, low friction sterilizable plastic. Space was provided for the PEEK components without significantly losing structural strength (Figure 3.15). The PEEK material covering the tabs on the sliders also prevents the pins from falling out (Figure 3.16).

The "plugs" (Figure 3.17) were used to secure the pins for the Front Spacer and Back Spacer joints (Figure 3.10). The reason for their separation from the housing was to isolate the pins holding the Front and Back Spacers to predominantly shear forces. The plugs themselves are held in place by permanently swaging the pin on both ends. The maximum exerted shear force on either the Front or Back Spacers is less than 160 N (Section 3.4), and the pin's maximum shear strength is 700 N. It will also be shown that 178 N of shear load does not permanently deform the pin (Section 3.4.1.3).

The jaws were heat treated to attain a higher FOS (Section 3.4.1). The motor housing with combined electronics and handle will be described in Section 3.5.

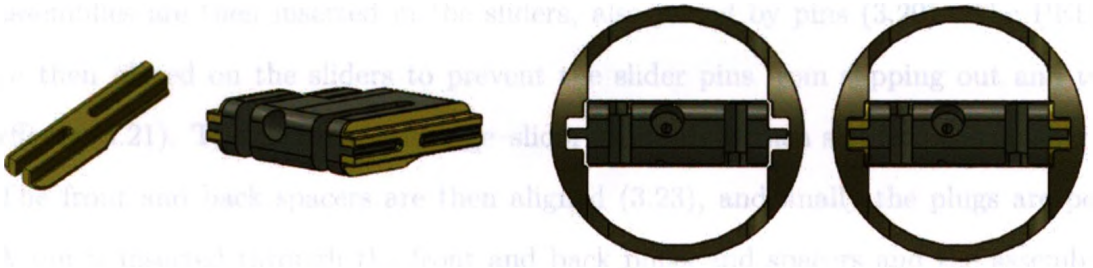

Figure 3.15: Left to right: PEEK component to cover slider sides, Front Slider with PEEK covers, end effector front view without PEEK covers, end effector front view with PEEK covers.

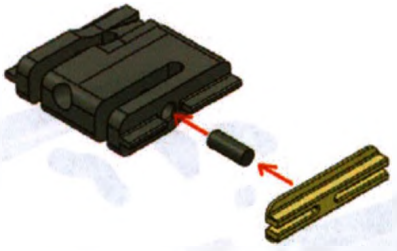

Figure 3.16: An illustration of how the PEEK covers prevent the pin joints from falling out.

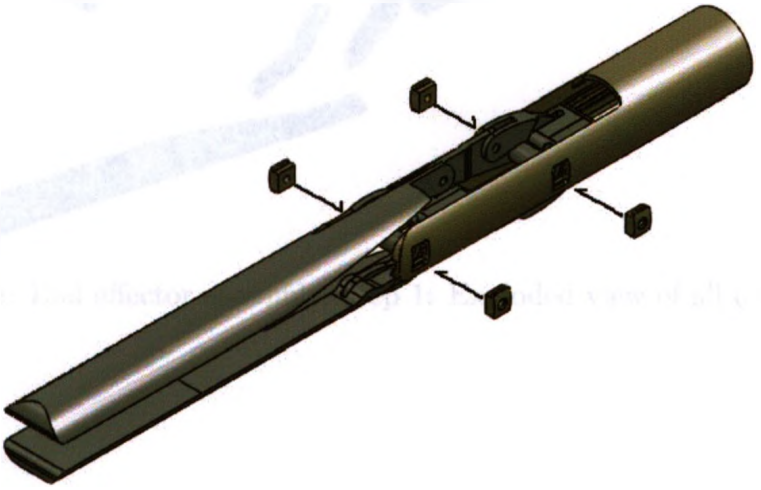

Figure 3.17: Front and Back Spacer "plugs" separated from the end effector housing.

Finally, Figures 3.18 through 3.24 show the assembly of the device. In Figure 3.18, the entire part is disassembled. First the jaw and linkages are joined together with pins (3.19). The two linkage assemblies are then inserted in the sliders, also joined by pins (3.20). The PEEK slider covers are then placed on the sliders to prevent the slider pins from slipping out and to reduce friction effects (3.21). The entire jaw–linkage–slider assembly is then slid into the grasper housing (3.22). The front and back spacers are then aligned (3.23), and finally the plugs are positioned (3.24). A pin is inserted through the front and back plugs and spacers and the assembly of the end effector is complete.

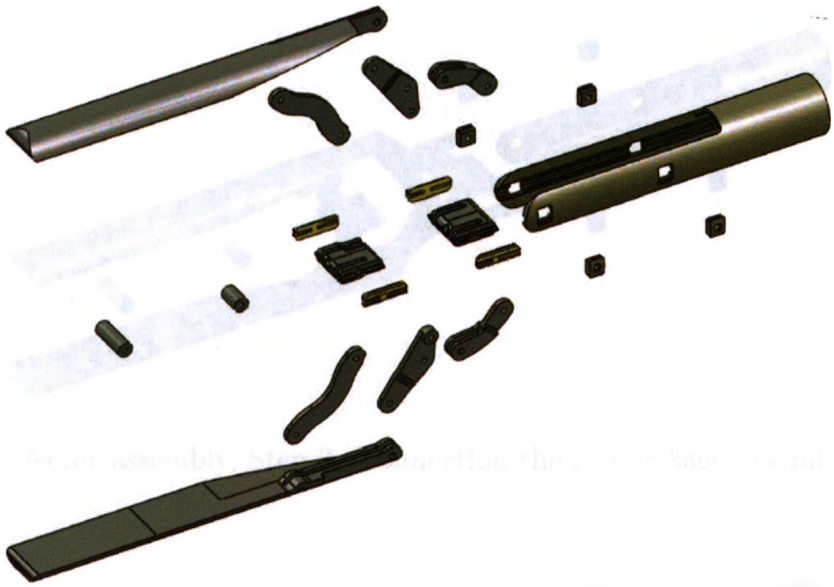

Figure 3.18: End effector assembly, Step 1: Exploded view of all components.

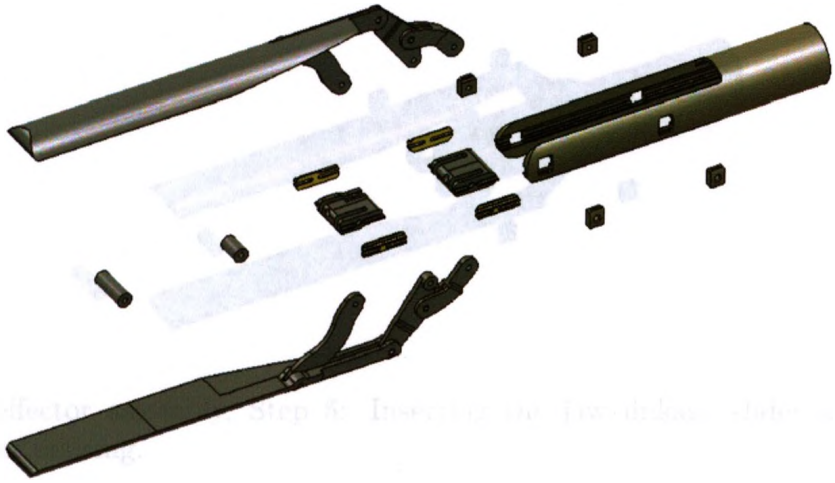

Figure 3.19: End effector assembly, Step 2: Connecting jaws and linkages.

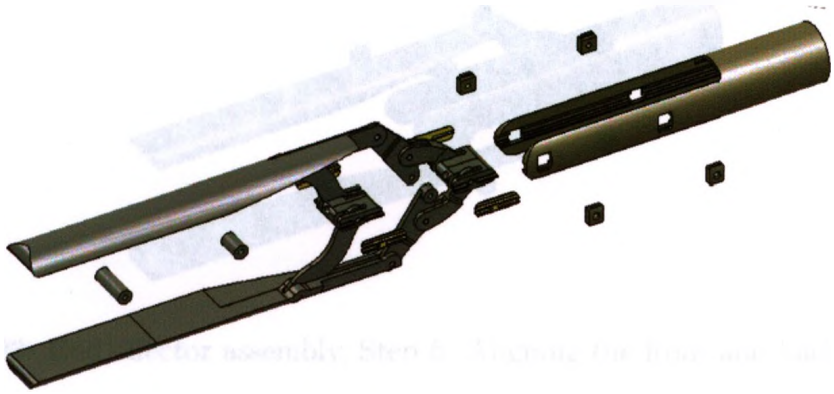

Figure 3.20: End effector assembly, Step 3: Connecting the jaw–linkage assemblies to the sliders.

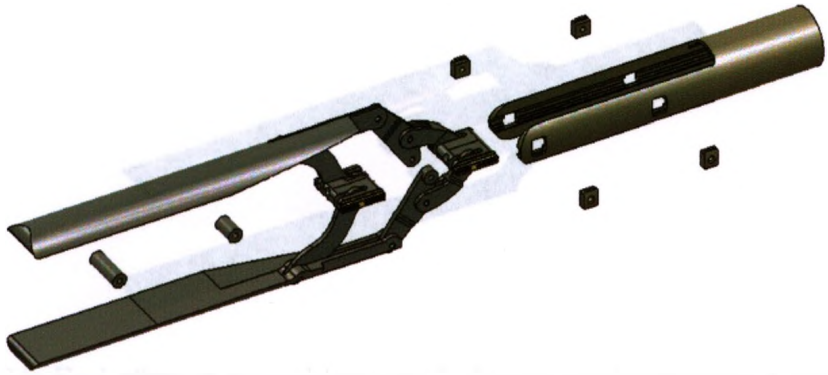

Figure 3.21: End effector assembly, Step 4: Connecting the PEEK slider covers over the sliders.

Figure 3.22: End effector assembly, Step 5: Inserting the jaw–linkage–slider assembly into the grasper housing.

Figure 3.23: End effector assembly, Step 6: Aligning the front and back spacers.

Figure 3.24: End effector assembly, Step 7: Inserting the front and back plugs.

3.4 Finite Element Analysis and Material Selection

A number of properties were considered in material selection, including corrosion resistance and the ability to be sterilized. Following a review of existing instruments, stainless steel was selected. Since the grasper should not permanently deform, the material stresses should not surpass the material yield strength using the von Mises stress criteria, suitable for ductile materials such as steel [43].

Initial simulations of the end effector were carried out to determine stresses in the linkages and jaws, and to find the resultant forces on the pin joints. SolidWorks Simulation 2010 was used for all FEA cases. For these analyses, a generic sensorless jaw geometry was used since the final jaw geometries had not yet been determined. This generic jaw connects to the linkages in the same manner as the final jaw geometries, providing validity to the results in the remaining components. Specific jaw geometry will be discussed later in the chapter. Five different grasper positions were analyzed. The five positions included (Figure 3.25):

Case I) A jaws parallel and closed position,

Case II) A jaws parallel and half opened position,

Case III) A jaws parallel and fully opened position,

Case IV) A jaws opened with a large positive inline angle position, and

Case V) A jaws opened with a large negative inline angle position.

In each of the five position cases, four different load cases were analyzed, shown in Figure 3.26 on the parallel open configuration (Case III):

Case a) A 20N force downward on the lower jaw,

Case b) A 20N force downward on the upper jaw,

Case c) A 20N force perpendicular to a jaw in the left direction, and

Case d) A 20N force perpendicular to a jaw in the right direction.

The load cases were chosen to represent the worst case scenarios of loadings — the maximum load in all possible directions in a variety of palpation scenarios.

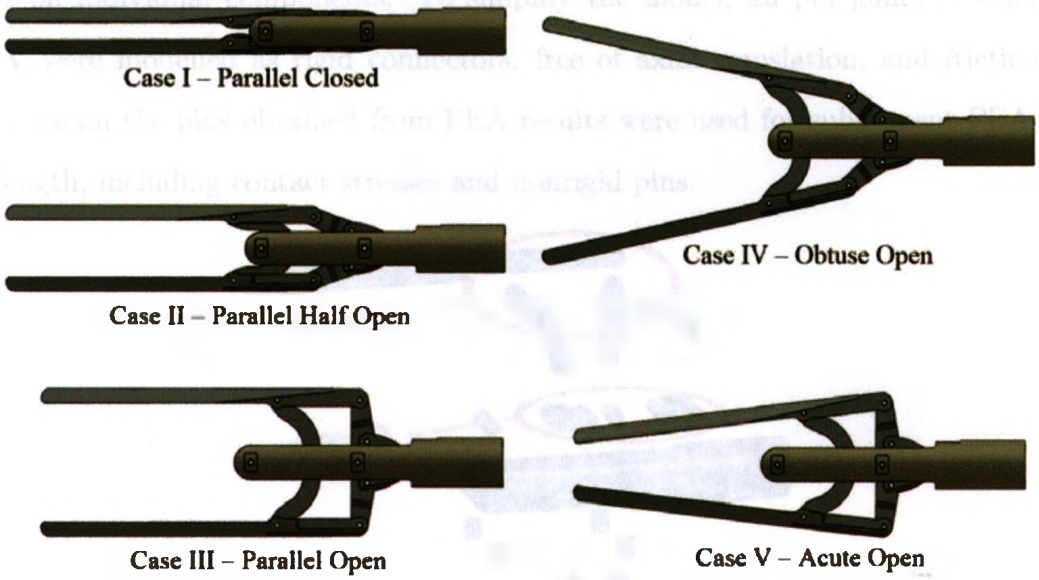

Figure 3.25: Configurations used for FEA studies.

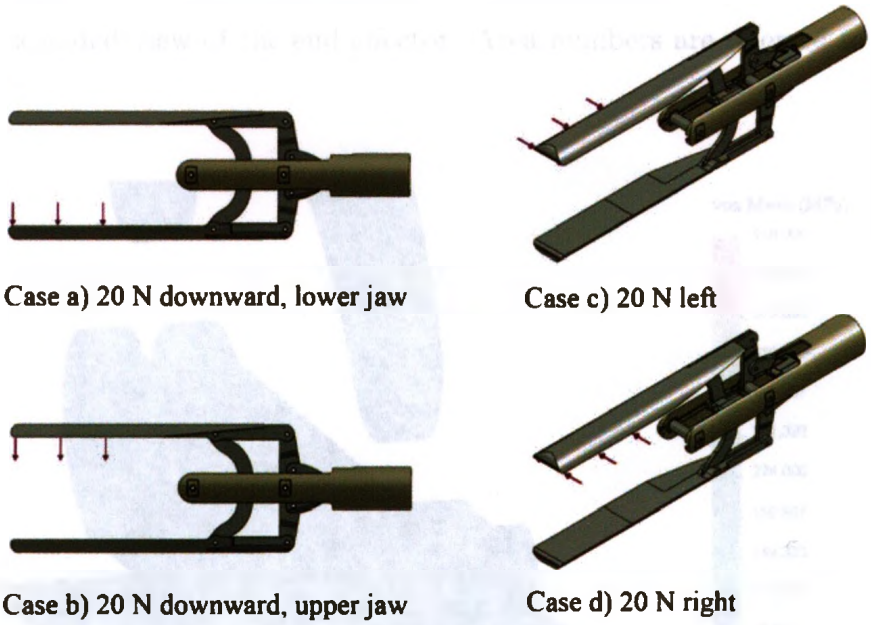

Figure 3.26: Load cases for all configurations displayed on the parallel open configuration (Case III).

The identified areas of interest are presented in the next series of figures showing FEA results on Case III in Load Cases a through d of the grasper. Exploded views are used to better visualize the stresses on individual components. To simplify the model, all pin joints in Configurations I through V were modelled as rigid connectors, free of axial translation, and frictionless. The resultant forces on the pins obtained from FEA results were used for subsequent FEA modelling of joint strength, including contact stresses and nonrigid pins.

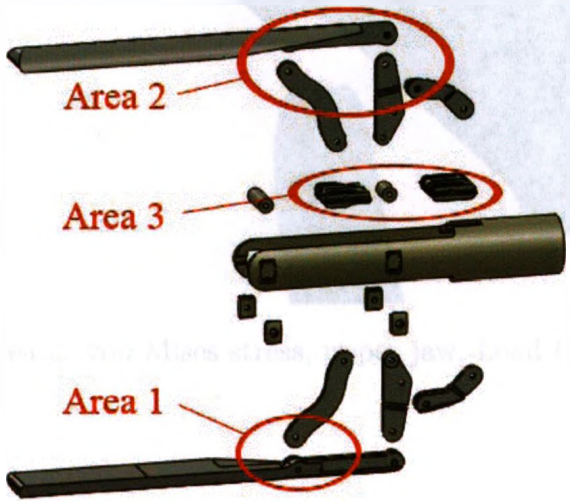

Figure 3.27: An exploded view of the end effector. Area numbers are referred to in the following figures.

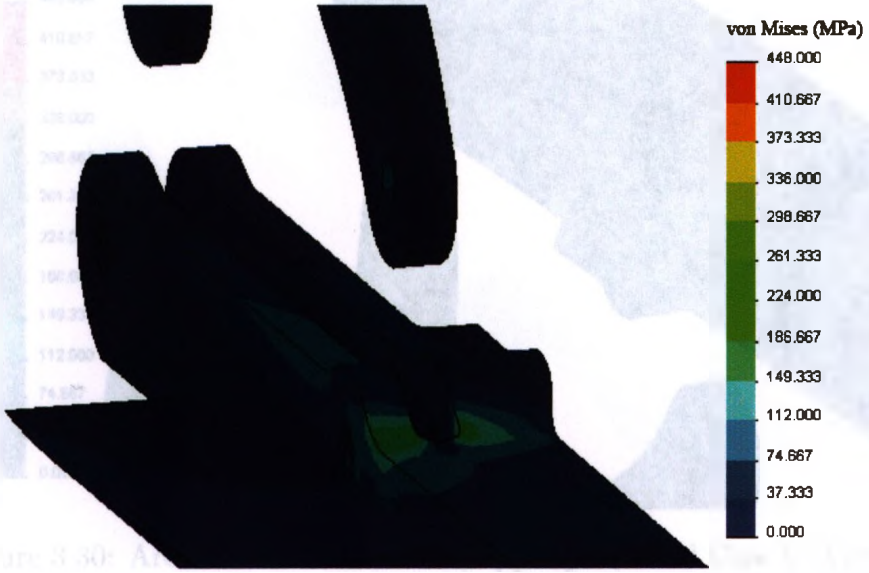

Figure 3.28: Area 1: von Mises stress, lower jaw, Load Case a.

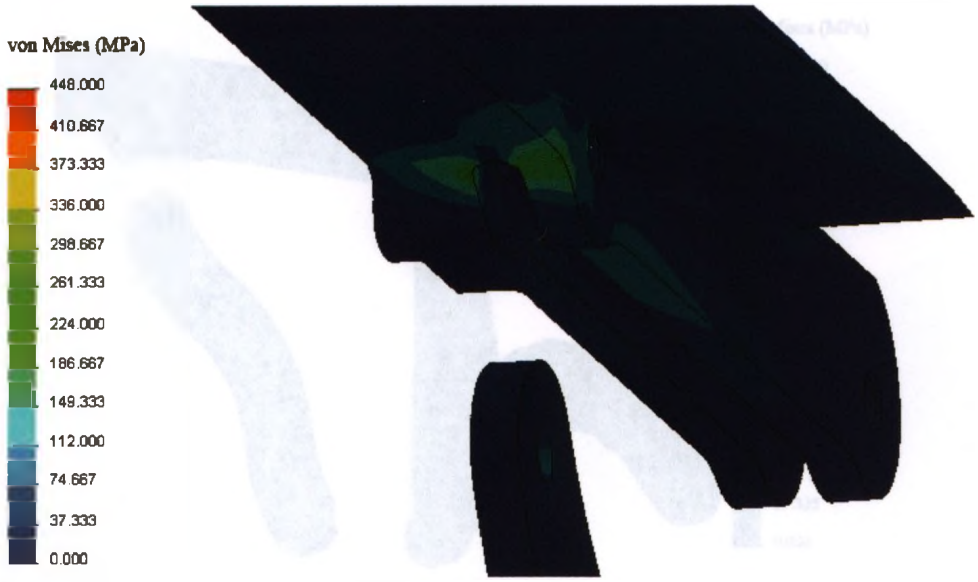

Figure 3.29: Area 2: von Mises stress, upper jaw, Load Case b (View 1).

Figure 3.30: Area 2: von Mises stress, upper jaw, Load Case b (View 2).

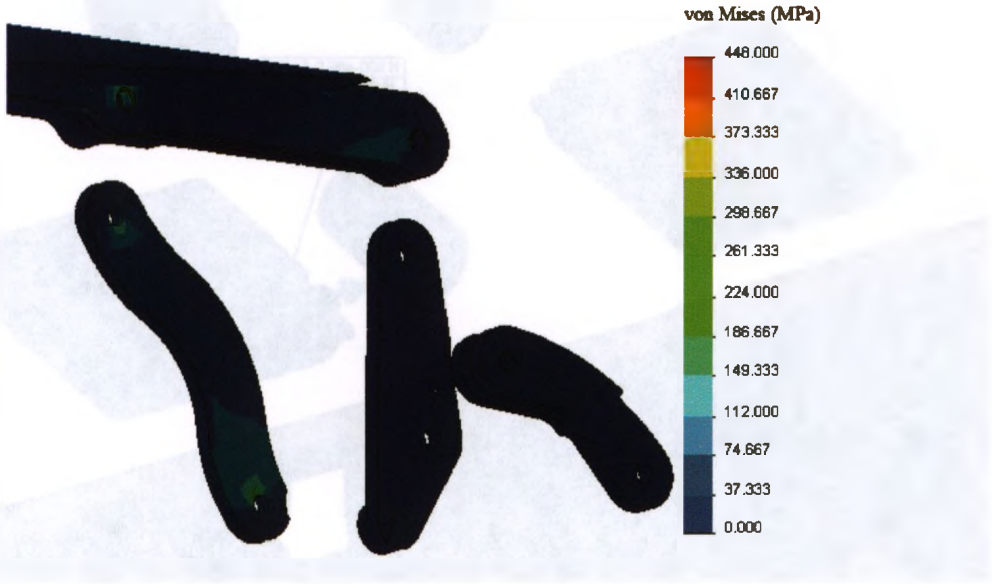

Figure 3.31: Area 2: von Mises stress, upper linkages, Load Case c.

Figure 3.32: Area 2: von Mises stress, upper linkages, Load Case d.

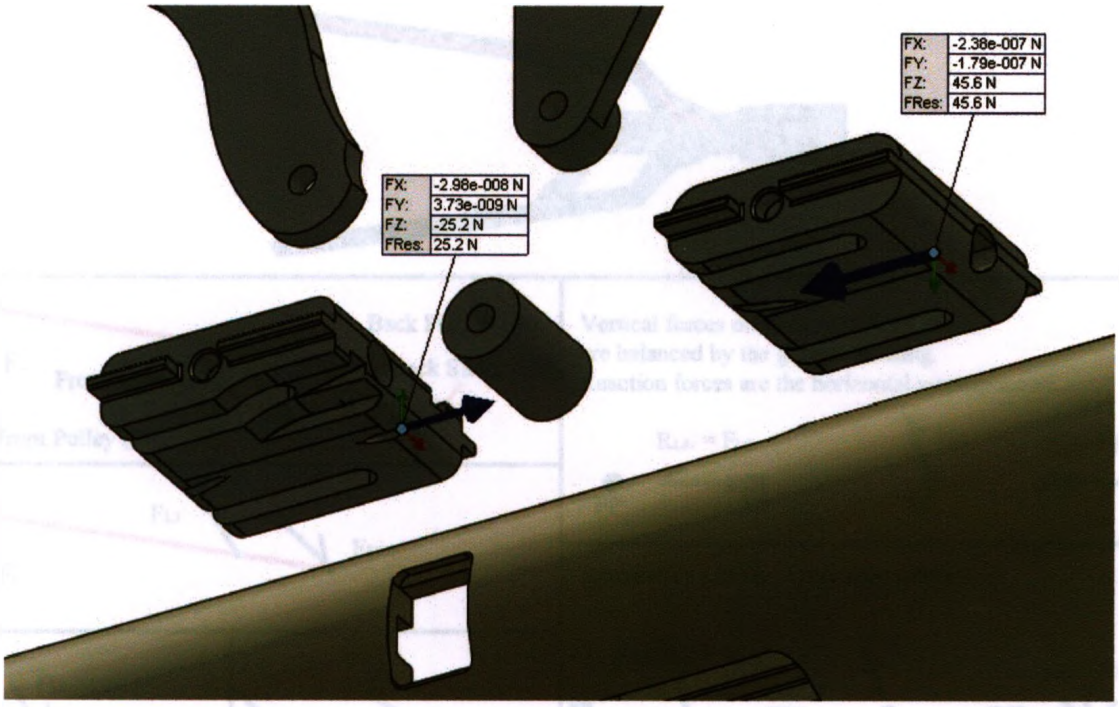

Figure 3.33: Area 3: Resultant force on sliders, Case a.

The area of highest stress concentration in all models was found in Load Case b around the pin Jaw Front (Figures 3.29 and 3.30), with a maximum value of 260 MPa. These results immediately eliminated the use of 300 series stainless steels because of their low yield strength. The stress scale shown was therefore adjusted for a higher strength steel alloy, 448 MPa yield strength for alloy 440C. Alloy 440C can be heat treated to further increase its yield strength. The Front and Back Sliders were fixed in the finite element model at the points shown in Figure 3.33. The sliders are actuated by cables. If the reaction forces in Figure 3.33 were directed forward on the sliders, the cables holding their positions would have to wrap around the Front and Back Spacers, using them as pulleys. This would induce a shear stress on the Front and Back Spacer pins. Forward direct forces were therefore used to determine the shear force on the pins at the Front and Back Spacer locations. Figure 3.34 graphically explains the reasoning behind this. In the figure, the Front Spacer and Back Spacer are referred to as the Front Pulley (FP) and Back Pulley (BP) since they are used as pulleys for the actuating cables, and to differentiate from the abbreviated Front Slider (FS) and Back Slider (BS).

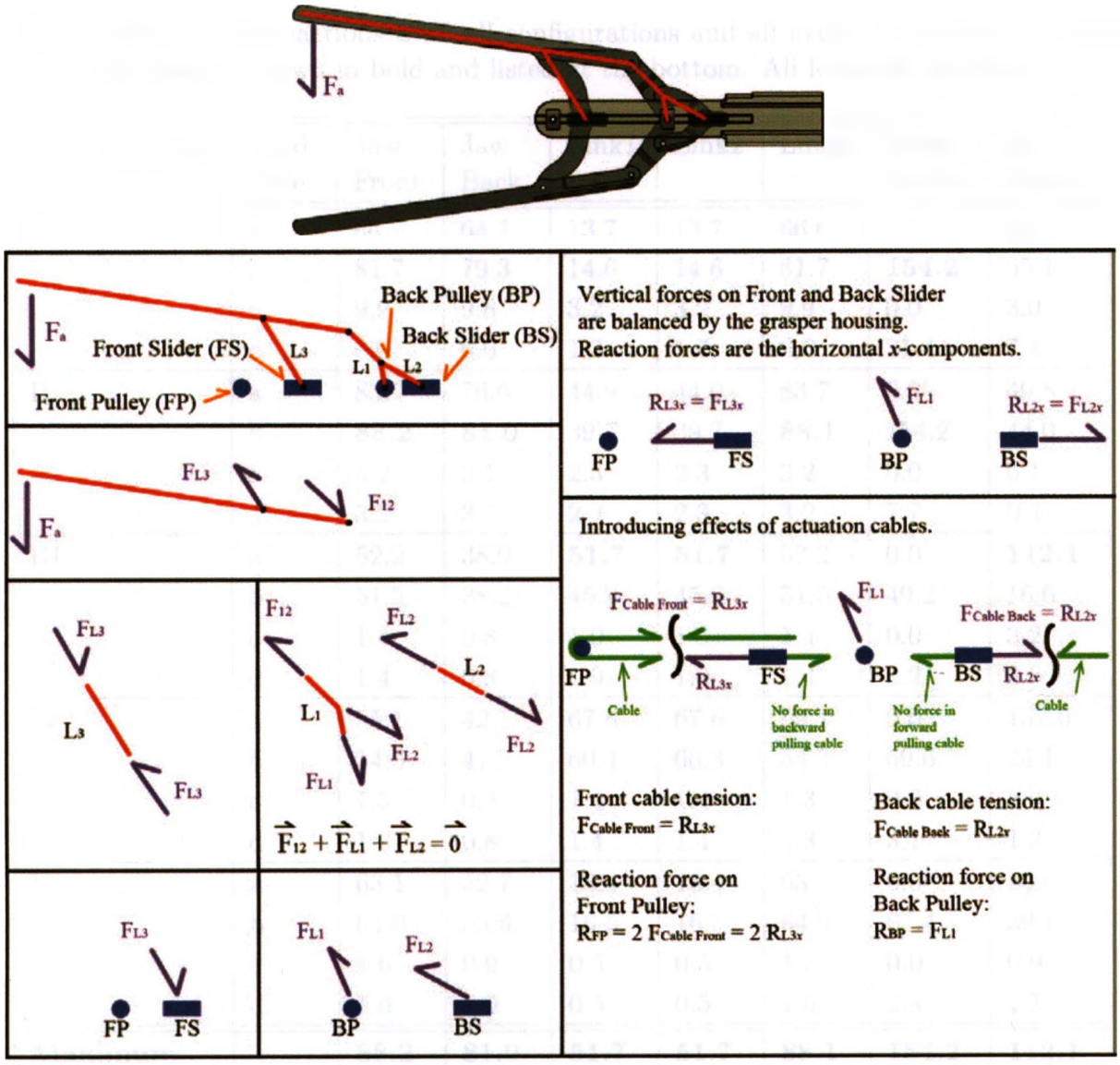

Figure 3.34: Reaction forces on Front and Back Pulleys.

The stresses on pin joints were predominantly shear stresses because the high tolerance between mating parts eliminated bending. This simplified pin model is appropriate since no axial or bending loads had to be applied to analyze joint strength. The highest shear force on each pin as identified from all studies was used on the weakest joint for analysis. The weakest joint was deemed to be the one that had the least amount of supporting material. Table 3.2 lists the highest pin shear forces from all configurations and load cases, and Figure 3.10 shows the joint naming system on half of the grasper design. Because of symmetry, the maximum shear force from either one of the symmetrical joints may be used for analysis.

Table 3.2: Table of joint reactions from all configurations and all loads. The maximum load for each joint is shown in bold and listed at the bottom. All forces in Newtons.

Configuration	Load Case	Jaw Front	Jaw Back	Link1	Link2	Link3	Front Spacer	Back Spacer
I	a	66.7	64.1	13.7	13.7	66.6	0.0	26.9
	b	81.7	79.3	14.6	14.6	81.7	**154.2**	65.1
	c	9.9	9.8	3.2	3.2	9.9	0.0	3.0
	d	6.0	6.0	1.7	1.7	6.0	21.4	7.1
II	a	83.7	76.6	44.9	44.9	83.7	0.0	49.8
	b	**88.2**	**81.0**	39.7	39.7	**88.1**	154.2	44.0
	c	3.2	3.1	2.3	2.3	3.2	0.0	6.1
	d	3.2	3.1	2.3	2.3	3.2	7.7	0.4
III	a	52.2	38.9	**51.7**	**51.7**	52.2	0.0	**112.1**
	b	51.5	38.2	45.9	45.9	51.5	49.2	16.6
	c	1.4	0.8	1.0	1.0	1.4	0.0	3.2
	d	1.4	0.8	1.0	1.0	1.4	2.2	0.8
IV	a	55.1	42.1	67.6	67.6	55.1	0.0	157.0
	b	54.3	41.2	60.4	60.3	54.3	69.6	24.1
	c	1.3	0.8	1.4	1.4	1.3	0.0	5.9
	d	1.3	0.8	1.4	1.4	1.3	3.1	1.3
V	a	63.1	52.7	18.4	18.4	63.1	0.0	25.6
	b	64.0	53.6	16.5	16.5	64.0	67.4	39.1
	c	1.6	0.9	0.5	0.5	1.5	0.0	0.9
	d	1.6	1.0	0.5	0.5	1.6	2.8	1.1
Maximum		**88.2**	**81.0**	**51.7**	**51.7**	**88.1**	**154.2**	**112.1**

The pin joints were designed the same as a double shear test — one linkage forked to let the next linkage fit in between, all held together by a pin (Figure 3.11). The weakest joints, assumed to be those which had the least supporting material, were analyzed with the largest resultant shear force because of the similarity between all joints, even if the resultant force did not act in the weakest direction. If the weakest joints were able to withstand the largest experienced force, then all joints could withstand their respective applied forces. As such, joints Link 1 and Link 3 were both analyzed under a 90 N load.

The studies of Link 1 and Link 3 both show a stress higher than yield strength for alloy 440C around the portion of the link that experienced compression. Nonlinear material analysis or testing could both be used to examine the effect of local yielding on the performance of the pin joints. Given the alternative to FEA, it was decided to address the problem by testing. Experiments were carried out to determine joint strength for both heat treated and untreated samples of 440C steel.

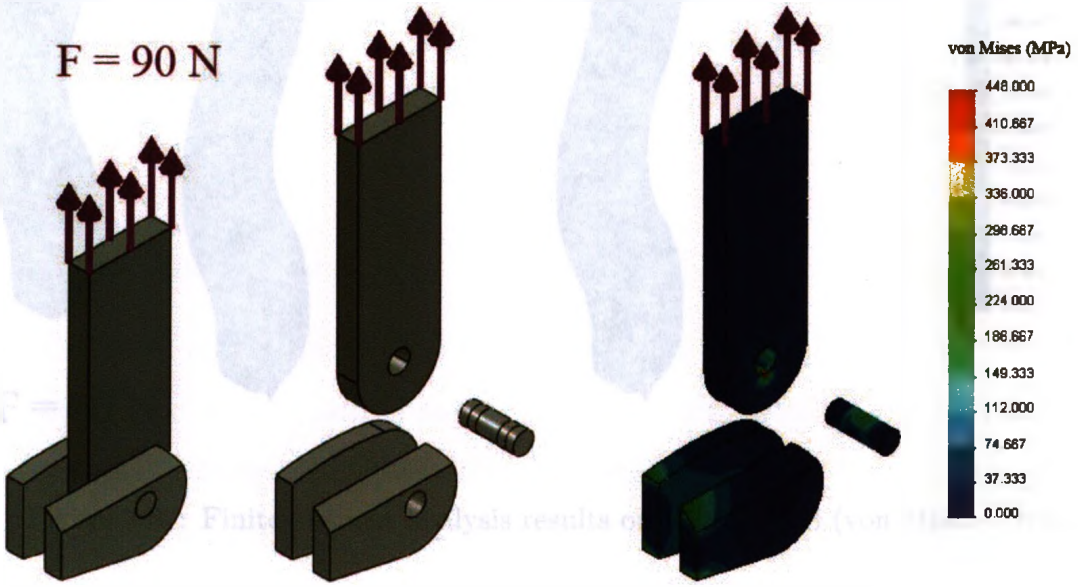

Figure 3.35: Finite element analysis results on joint Link 1 (von Mises Stress).

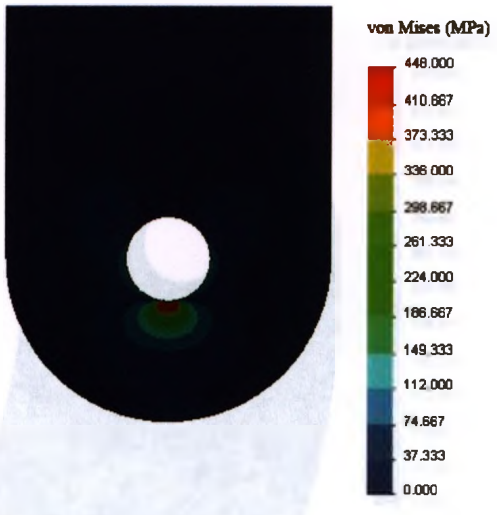

Figure 3.36: Close up of finite element analysis results on joint Link 1 (von Mises Stress).

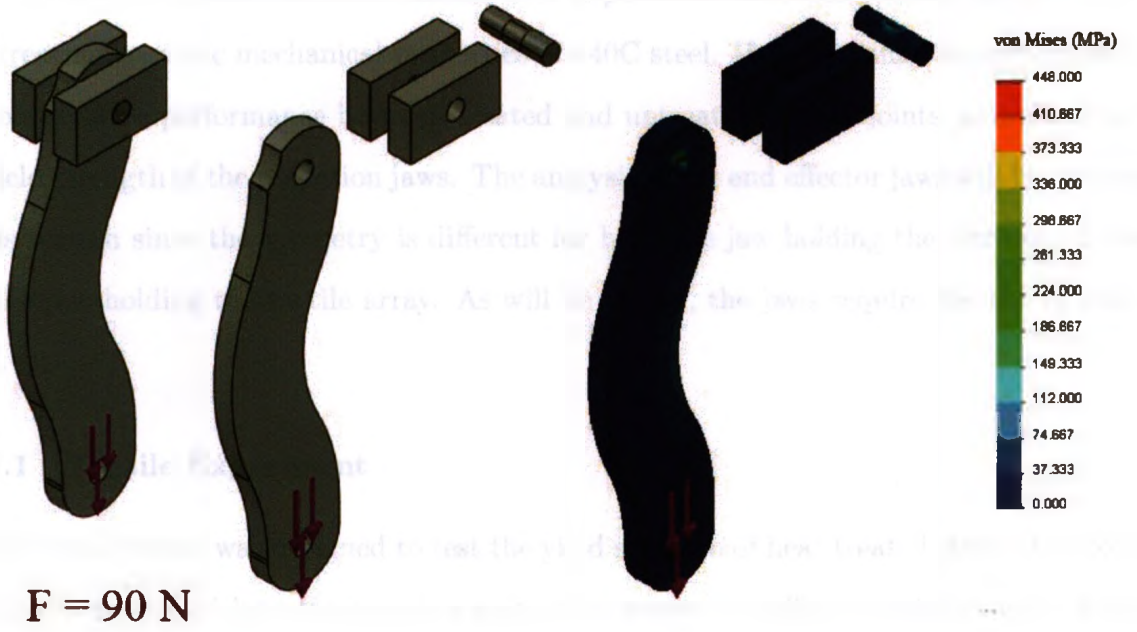

Figure 3.37: Finite element analysis results on joint Link 3 (von Mises Stress).

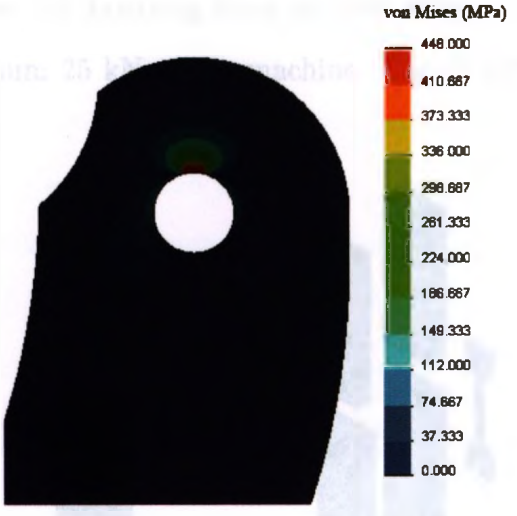

Figure 3.38: Close up of finite element analysis results on joint Link 3 (von Mises Stress).

3.4.1 Heat Treating

A heat treatment procedure and a tensile test experiment were designed to analyze the effect of heat treatment on the mechanical properties of 440C steel. Heat treating was considered to assess the comparative performance between treated and untreated linkage joints, as well as to increase the yield strength of the palpation jaws. The analysis of the end effector jaws will be discussed later in this section since the geometry is different for both the jaw holding the ultrasound transducer and the jaw holding the tactile array. As will be shown, the jaws require the use of heat treated 440C.

3.4.1.1 Tensile Experiment

A tensile experiment was designed to test the yield strength of heat treated steel. Holes of different diameter were drilled into the tensile specimen to assess the effects of shrinkage or enlargement after heat treating. The experiment was designed in SolidWorks 2010. To verify the forces required to cause yield in a specimen with a yield strength of 1900 MPa, which is the highest attainable yield strength for heat treated 440C [44], a sample with a rectangular cross section of 7.72 mm^2 was used. This cross section assumed that the sample could be tested in a QTest QT/25 machine capable of a 25 kN tensile load. With a purchased 440C sheet thickness of 1.93 mm, a 4.00 mm width was designed such that the breaking force of 1900 MPa $\times$ 1.93 mm $\times$ 4.00 mm = 14.668 kN was less than the maximum 25 kN of the machine. Figure 3.39 shows the design of the test specimen and jig to hold it.

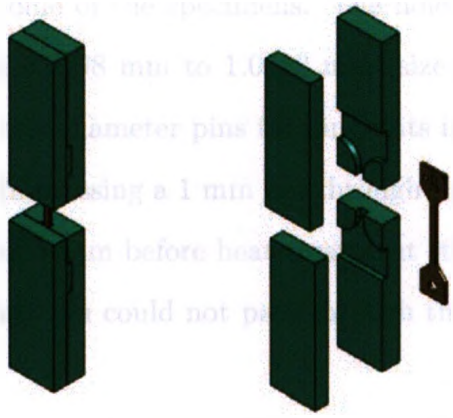

Figure 3.39: Tensile specimen and jig for material testing. Left: Assembled. Right: Exploded.

3.4.1.2 Heat Treatment

The objective of the heat treatment procedure was to increase the yield strength of the 440C alloy. Simultaneously, the shrinkage or enlargement after heat treating was assessed. The procedure consisted of the following steps:

1. Place the specimen in an oven at room temperature. Set the temperature to heat to 550 °C over 5 hours [45]. Let the parts sit for 1 hour [46].
2. Set the temperature to heat to 760 °C (from 550 °C) over 3 hours [45]. Let the specimen sit for 30 minutes.
3. Increase the heat rapidly to 1035 °C [45], wait until the temperature has been reached. Wait 30 minutes, and remove the parts [45]. Oil quench the specimen to room temperature.
4. Immediately after quenching (when the part is cool to the touch), place the specimen in an oven at room temperature and gradually heat to 315 °C at 100 °C per hour. When the temperature has been reached, leave the specimen in the oven for an hour. Remove and air quench to room temperature [46].
5. Repeat Step 4 to remove retained austenite [47].

A temperature–time graph of the procedure is shown in Figure 3.40. It was noted that the specimens were covered by a film of oxidation due to the presence of air during the heat treatment cycle. The film was sanded off by pressing the specimens against 400 grit sandpaper. Warpage and bending were exhibited in some of the specimens. The holes drilled into the specimen were of 5 different sizes ranging from 0.9398 mm to 1.0668 mm (size #58–63 drill bits). These sizes were chosen due to the use of 1 mm diameter pins for pin joints in the final design. There was no shrinkage or enlargement found in pressing a 1 mm pin through the different sized holes after heat treating. Holes drilled larger than 1 mm before heat treatment still allowed the 1 mm pin to pass through them. Similarly the 1 mm pin could not pass through the holes originally drilled smaller than 1 mm.

Some specimens exhibited undesirable pitting (Figure 3.41). The presence of the oxidation and the pitting meant that if the parts were to be heat treated, they would have to be machined twice;

once to an approximate dimension followed by heat treating, and again to remove excess material that would include the oxidation film and pitting effects, an undesirable side effect that would increase the cost of manufacturing. It is noted that heat treating in the presence of an inert gas would reduce the exhibited negative consequences of heat treating.

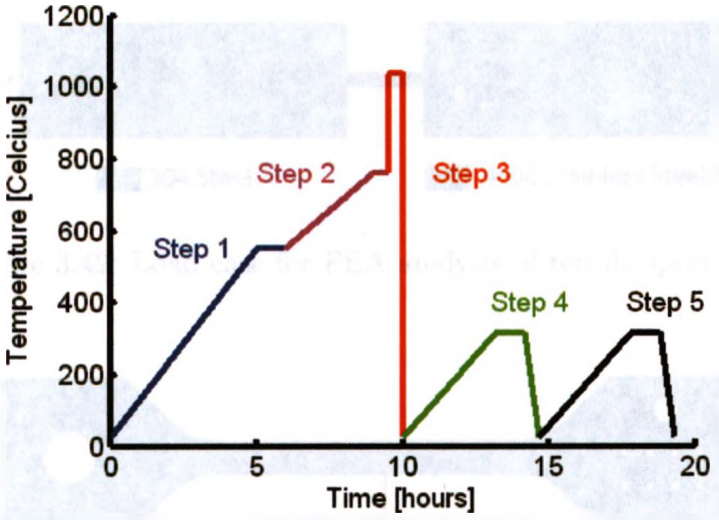

Figure 3.40: Temperature–time graph of the heat treatment procedure.

Figure 3.41: Pitting effects from heat treatment.

A QTest QT/25 tensile strength testing machine was used to assess the ultimate tensile strength of the specimens. Seven samples were tested resulting in ultimate tensile forces of 13.950 kN, 13.243 kN, 13.191 kN, 13.234 kN, 13.917 kN, 14.425 kN, and 13.774 kN. An average breaking force of 13.676 kN and standard deviation of 0.469 kN was calculated. The heat treated specimens exhibited a brittle fracture, and showed no measurable necking as measured with a digital caliper accurate to 0.01 mm. To make a conservative conclusion, the breaking strength of the heat treated specimens was calculated as the average breaking strength minus two standard deviations, 12.737 kN. This resulted in an ultimate strength of 1650 MPa. The 12.737 kN breaking load was then

simulated in SolidWorks Simulation 2010 to compare experimental and theoretical results (Figure 3.42), and to validate the force output readings of the QTest QT/25 instrument. Analysis of the principle stresses was carried out due to the brittle nature of the heat treated steel [43] (Figure 3.43).

Figure 3.42: Load case for FEA analysis of tensile specimen.

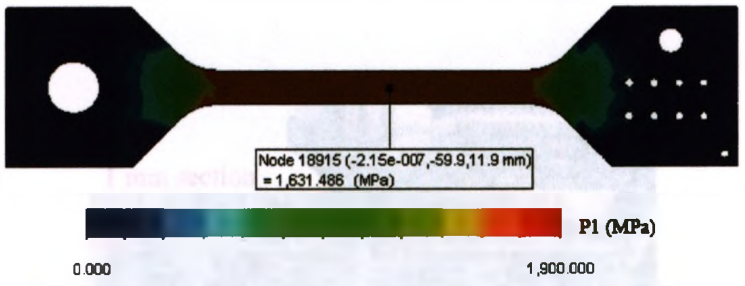

Figure 3.43: Theoretical principle stress in the tensile specimen.

The central portion of the specimen shows the highest first principle stress, corresponding to the tensile stress. Analyzing a single node on the yielding portion of the specimen shows a stress of 1631 MPa. With a percentage error of less than 1.2% between experiment and theory, 1650 MPa was concluded to be the conservative ultimate tensile strength of the heat treated steel.

3.4.1.3 Testing Heat Treated Parts

The effect of heat treatment on pin strength was studied in a test duplicating the design of the joint to be used. Weights were hung to apply a load on the pin joint. The FOS on the pin joints compared to the maximum force results from Table 3.2 were examined. An untreated specimen was milled to a thickness of 1 mm, and the edges around one of the 1.016 mm holes was ground down to a width of 2.8 mm around the hole (Figure 3.44), simulating a worse case than that of

the final design which had a material width of 4 mm around the joint hole with the same 1 mm thickness. Weights were then hung from the pin joint in a double shear manner (Figure 3.45).

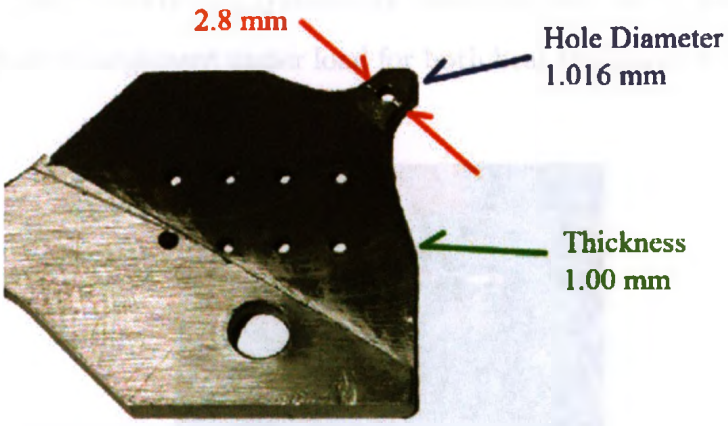

Figure 3.44: Sample for joint strength test.

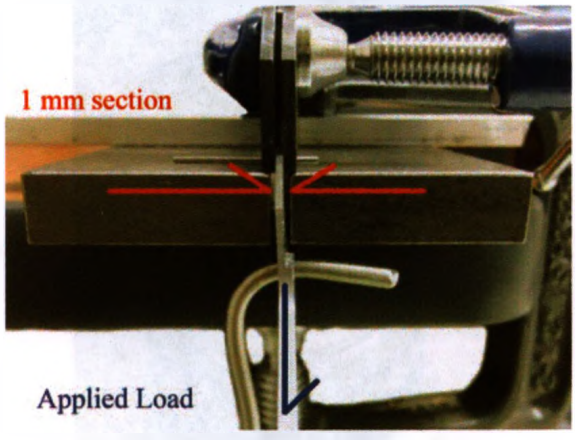

Figure 3.45: Double shear test setup.

With an applied load of 178 N, there was no visible damage to the supporting pin or the specimen. This was 23 N higher than the expected load on pin Front Spacer, the pin with the highest expected shear loading. The tested pin sustained 364 N of applied load (Figure 3.46). With the exhibited factor of safety of roughly 4, the experiment was not carried out to failure. Though the sample did not break, at the 364 N load some damage was visible after the removal of the weights (Figure 3.47). Under load, the hole expanded due to local deformation and subsequent hardening of the material. The pin's rated shear strength in double shear was 700 N to failure, which explained why it did not break. Qualitatively, the effects of hole enlargement in the heat

treated sample were smaller. This experiment provided insight on the joint strength in that heat treating the joints was not a necessity, but could provide better system response by reducing nonlinearities with regards to control systems by reducing play in the joints. To determine this, closer inspection of hole enlargement under load for both heat treated and untreated samples would have to be assessed.

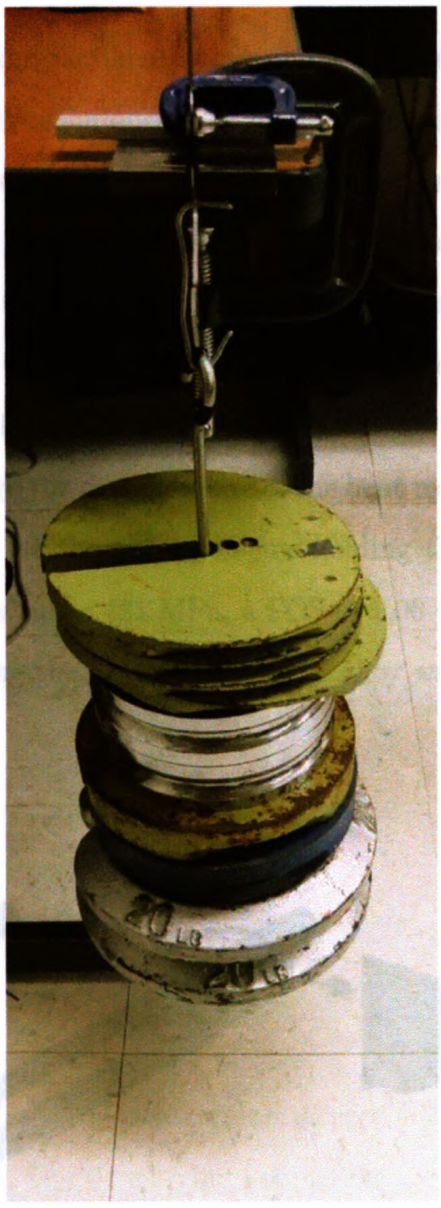

Figure 3.46: Joint strength test sample with 364 N applied load.

Figure 3.47: Pin yielding in shear.

The inclusion of ultrasound and tactile sensors require top and bottom jaw geometry to be different due to the sensor mounting techniques used for sensor specific requirements. The presented CAD jaw geometry thus far has been for a generic sensorless jaw. Jaw geometry for the ultrasound mounted jaw is presented and analyzed to show the necessity of the heat treated material. Similarly, the jaw geometry for the tactile sensor must be analyzed. However, during the course of this project, a final geometry was not yet determined and is considered as future work.

The heat treatment process showed that a conservative estimate on the ultimate strength of the material was 1650 MPa. Although the disadvantage of the heat treated material was its brittleness, its high strength was necessary for the palpation jaw holding the ultrasound transducer, which exhibited stress concentrations of up to 421 MPa, a FOS of 1.06 with untreated 440C, in its worst configuration (Figure 3.48). Using the heat treated 440C alloy was therefore necessary to improve the FOS from 1.06 to 4.

Figure 3.48: Tensile stresses in ultrasound jaw geometry.

3.5 Design and Analysis of the Motor Housing

This section discusses all of the components other than the grasper. Immediately attached to the grasper is the stainless steel tube that houses the wires and cables attached to the grasper jaws and sliders. With a standard tube diameter of 12.7 mm, it was verified that the tube could fit through a 12 mm Ethicon Endopath XCEL trocar. Two studies were carried out on the 12.7 mm diameter, 1.422 mm thick, stainless steel tube, alloy 304. The first was a linear buckling analysis on a 400 mm long section of tubing to determine the capability of the shaft to hold a load without buckling. An axial load was used in analysis because the cables attached to the sliders produce this type of load. A buckling load of 1431 N was found. Comparing the largest combination of shear force exerted on pins Front Spacer (155 N) and Back Spacer (112 N) (Table 3.2), which translates to the total axial force on the shaft of 267 N, to the buckling load, it was clear that the buckling load was significantly higher than the maximum possible axial force. Even though a linear buckling analysis provides a nonconservative result, with such a large buckling load compared to the maximum possible force, it was concluded that the tube would not fail in buckling (Figure 3.49).

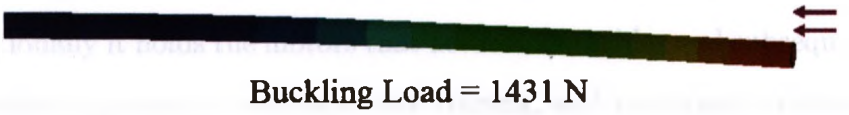

Figure 3.49: Result of buckling load analysis of the instrument tube.

The second load case was that of the shaft holding a 20 N radially directed load representing the weight of the supported lung, and a 266 N load axially representing the reaction forces on the cables from the sliders in the highest load scenario. The load case was simulated on a 150 mm long section, representing the depth with which the end effector would penetrate the trocar during manipulation of the lung. The simplifying assumption is explained in Figure 3.50. Due to modelling the tube as rigid at one end, the FOS was artificially low because of over constraining. The tube followed the ASTM A269 standard, having a yield strength of 241 MPa, and therefore a factor of safety greater than 3.8. It was concluded that the tube would not yield and was appropriate for the design (Figure 3.51).

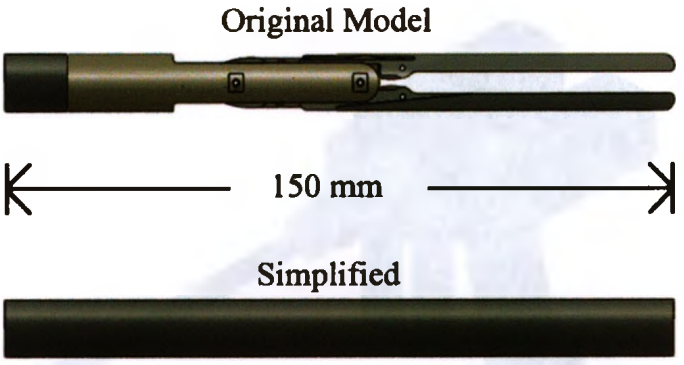

Figure 3.50: Simplifying assumption for tube analysis model – the tube replaces the geometry of the end effector.

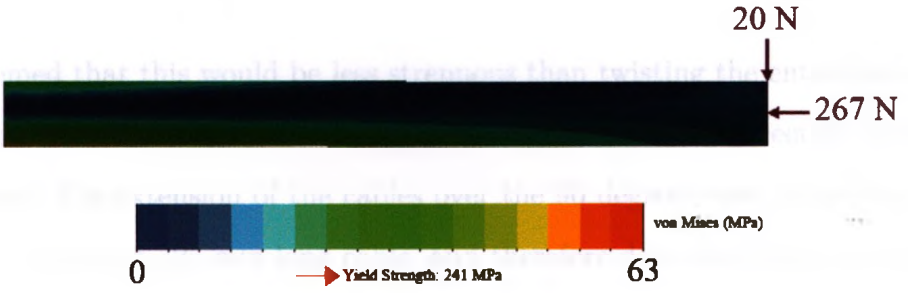

Figure 3.51: von Mises stress on the instrument tube.

The motor housing includes a method to twist the grasper jaws without twisting the entire instrument. Additionally it holds the motors that actuate the cables and subsequently the palpator jaws, the cable tensioning system, electrical wire routing, and electronics controlling the motors. The housing is held by an acrylonitrile butadiene styrene (ABS) handle to encase everything into a holdable item (Figure 3.52).

In the foremost position of the motor housing, a handle is able to twist the end effector without having to twist the entire motor housing. This cylindrical handle is made of PEEK and is mounted to the grasper shaft. The angular position of the grasper is maintained by a toothed clutch pressed together with a spring. The PEEK handle is able to slide lengthwise along the shaft and rotate the instrument shaft by pushing against a welded tab. The welded tab, running parallel to the shaft, prevents the handle from twisting about the shaft, but allows for movement along the shaft. To twist the grasper to a new position, the handle is pushed outwards, twisted, and released to re-settle the toothed clutch into its new position (Figure 3.53). With this method, the angular position of the grasper relative to the motor housing is meant to be set and maintained during

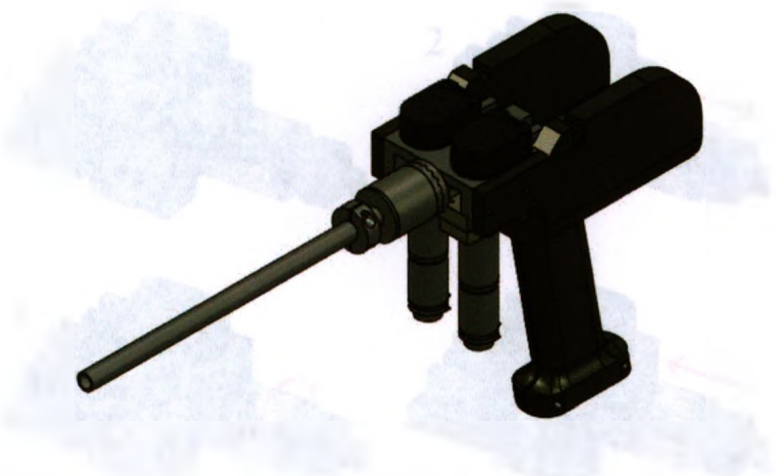

Figure 3.52: The entire instrument not including the grasper.

MIS. It was deemed that this would be less strenuous than twisting the entire motor housing and attached components. The range of twisting is 90 degrees in either direction with a total of 11 discrete positions. The extension of the cables over the 90 degree twist is less than 0.046 mm on a conservatively measured 325 mm long cable, and therefore does not require compensation. The twisting of the end effector adds approximately 4.4 N of force on the cables (Figure 3.54), and therefore adds 8.8 N on the Front and Back Spacer pins. With this additional force, the shear pin force is still less than 178 N (see Section 3.4.1.3), a force that does not cause permanent damage to the pins. Using the 178 N force as the upper limit, the cables could be pre-tensioned with a 14 N force.

With the presented tensioner system, no feedback in terms of measuring cable tension exists. Even so, the maximum forces on the end effector apply to the Front Spacer pin. If this pin deforms under load, it does not affect the geometry related to the grasper; however the cable would likely have to be tensioned again due to the deformation of the pin.

The presented tensioner system tensions each cable. This allows integration of strain gauges to measure cable tension on each cable moving the Front and Back Sliders, allowing dynamic measurement of cable tension. This is considered as future work. Tungsten cables were used for their high tensile strength and small end mountings, as inspired by the da Vinci surgical robot made by Intuitive Surgical Incorporated. With a 304 stainless steel ball swaged on the end, the cables had a breaking strength of 290 N, exceeding the maximum expected loads by 200 N.

The motor housing holds the motors in place, routes the actuating cables through the tensioning

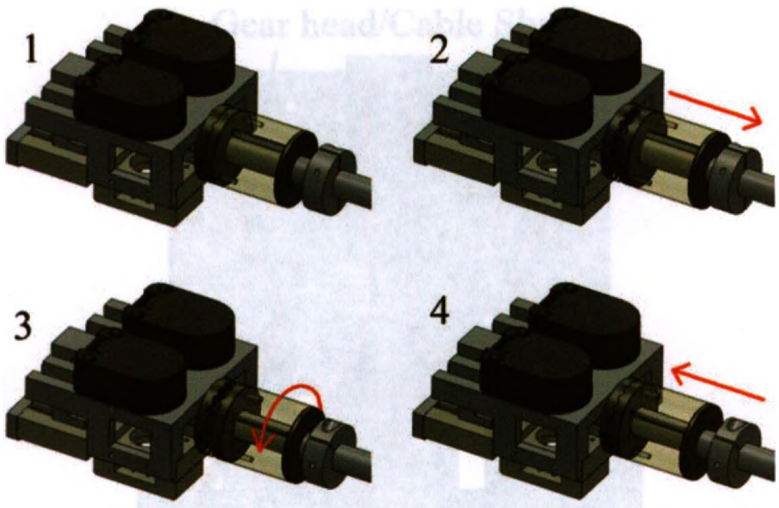

Figure 3.53: Twisting the end effector. The PEEK handle is shown translucent.

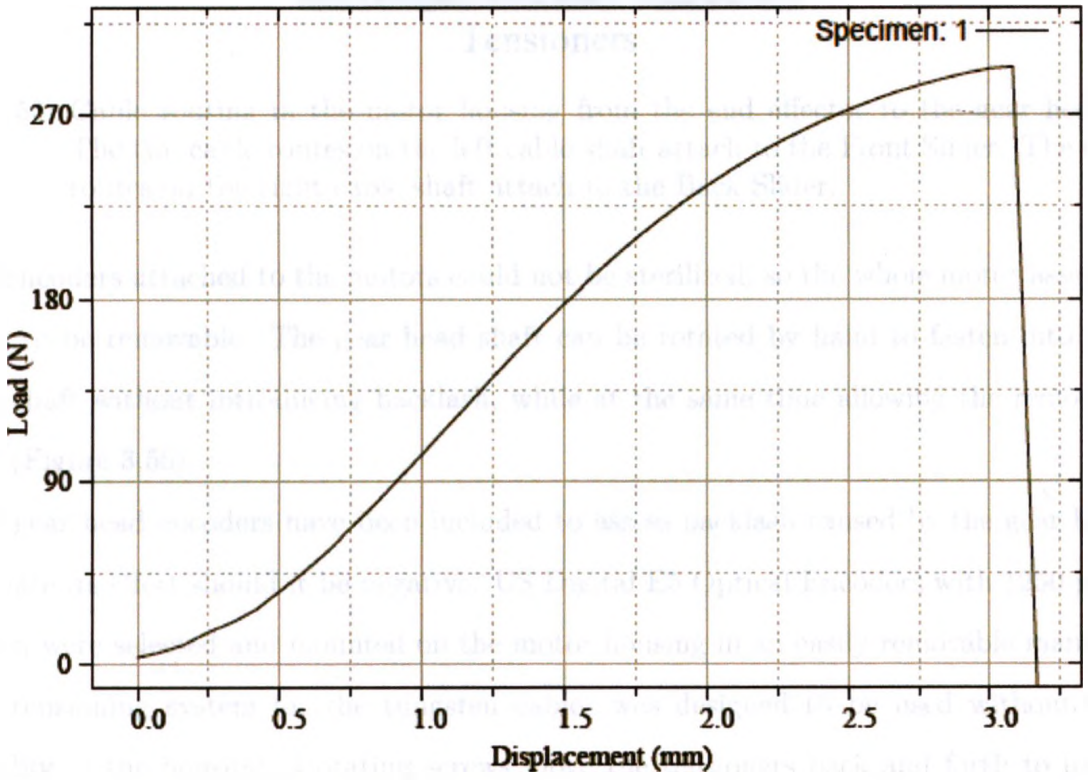

Figure 3.54: Load–displacement plot of the tungsten cable used in the design. Initial cable length of 250 mm.

system and to the gear head shaft (Figure 3.55), and has the post gear head encoders mounted to it. Since the entire assembly was designed to be sterilized, those components that could not be sterilized were designed for easy disassembly.

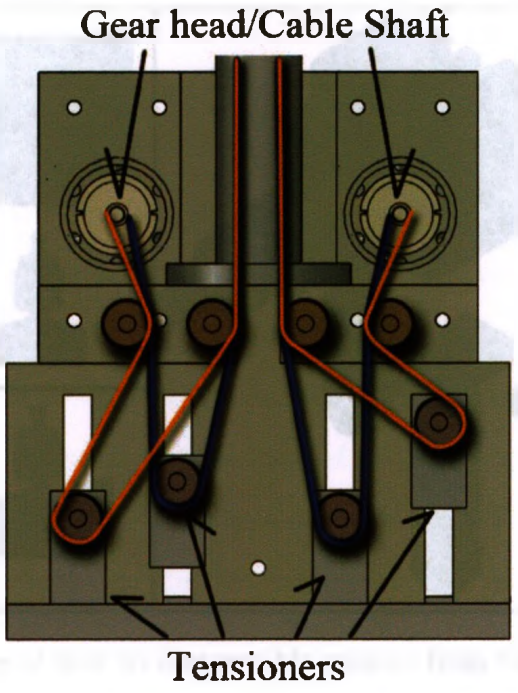

Figure 3.55: Cable routing in the motor housing from the end effector to the gear head shafts. The two cable routes on the left cable shaft attach to the Front Slider. The two cable routes on the right cable shaft attach to the Back Slider.

The encoders attached to the motors could not be sterilized, so the whole motor assembly was designed to be removable. The gear head shaft can be rotated by hand to fasten into the cable winding shaft without introducing backlash, while at the same time allowing the removal of the motors. (Figure 3.56).

Post gear head encoders have been included to assess backlash caused by the gear heads and to eliminate its effect should it be negative. US Digital E5 Optical Encoders with 1250 pulses per revolution were selected and mounted on the motor housing in an easily removable manner.

The tensioning system for the tungsten cables was designed to be used without requiring disassembly of the housing. Rotating screws move the tensioners back and forth to increase or decrease the tension in the cables (Figure 3.57). The pulleys used are 7.23 mm in diameter and rotate about 2.37 mm diameter pins, both stainless steel. To eliminate back-driving, a fine-pitch screw was used in the tensioning mechanism. No tensioning springs were included because the system could be tensioned by hand when necessary.

Fitting together in two halves, the ABS handle surrounds the motor housing assembly. The handle provides space for placing electronics and routing power and sensing cables to their data ac-

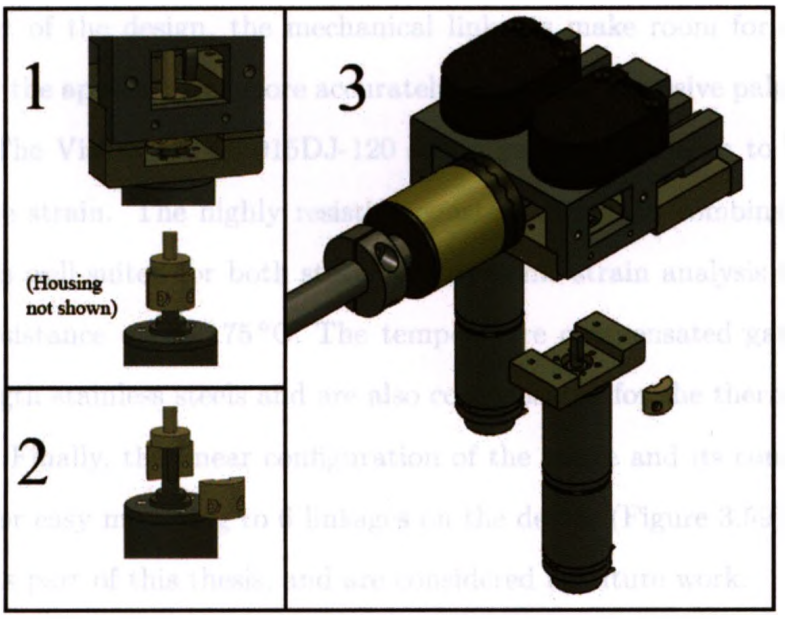

Figure 3.56: Steps of how to disassemble motors from the motor housing.

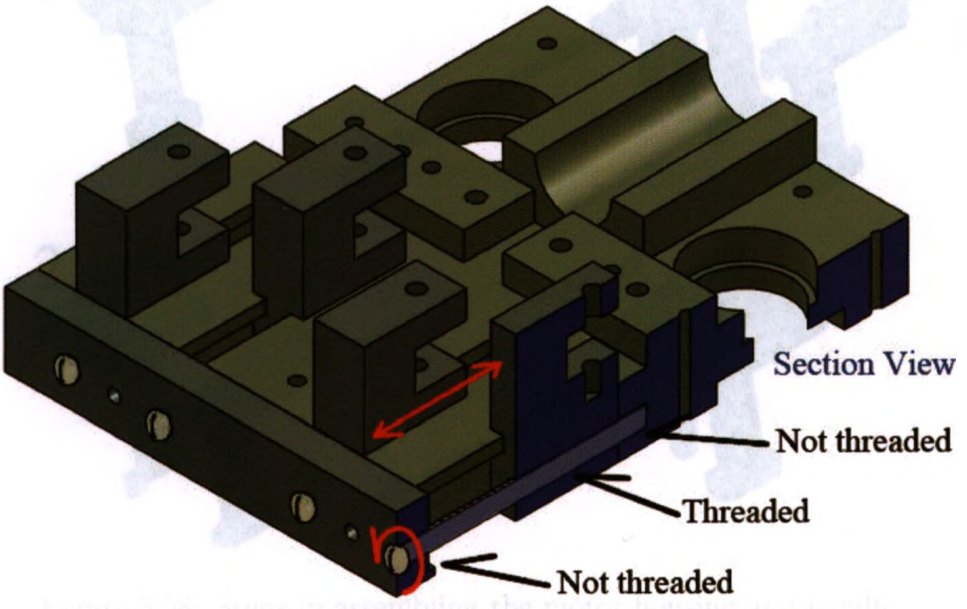

Figure 3.57: Functionality of tensioners.

quisition units. Mounting the electronics on the handle also allows for the separation of electronics from the motor housing for sterilization purposes (Figure 3.58).

As the final part of the design, the mechanical linkages make room for strain gauges to be mounted to monitor the applied force more accurately to prevent excessive palpation forces leading to tissue damage. The Vishay EA-06-015DJ-120 strain gauge was chosen to be used in multiple locations to measure strain. The highly resistive constantan foil, in combination with a flexible polyimide backing is well-suited for both static and dynamic strain analysis with an error of 3% and temperature resistance up to 175 °C. The temperature compensated gauges are specifically suited to high strength stainless steels and are also compensated for the thermal expansion of the mounting material. Finally, the linear configuration of the gauge and its compact size (2.54 mm × 0.51 mm) allow for easy mounting to 6 linkages on the device (Figure 3.59). The strain gauges were not mounted as part of this thesis, and are considered as future work.

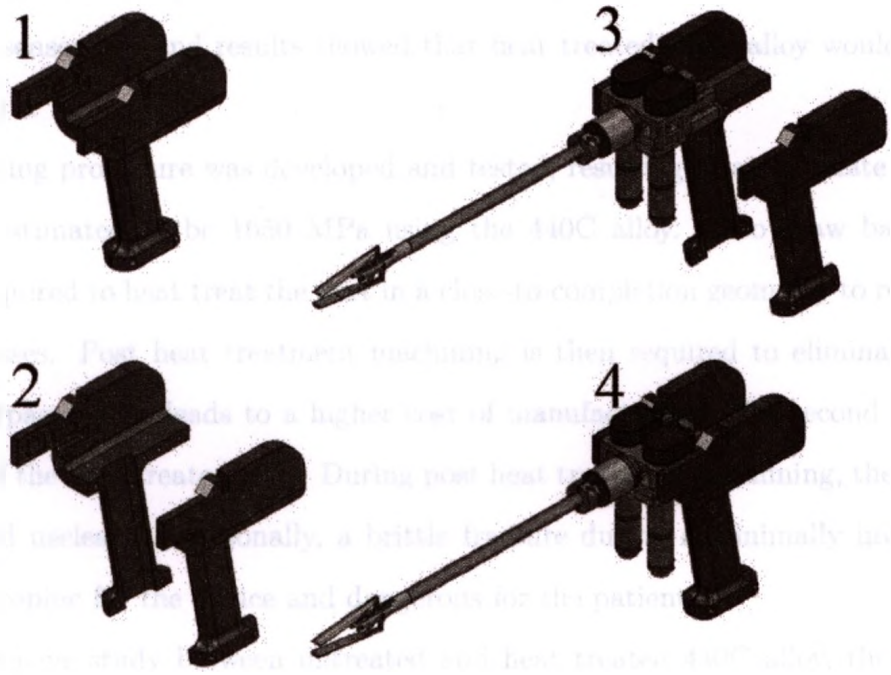

Figure 3.58: Steps in assembling the motor housing and handle.

Figure 3.59: Location of strain gauges for extrinsic force measurements on the grasper jaws highlighted in red on half the grasper model.

3.6 Conclusion

With an iterative design process initially inspired by a Babcock grasper, a novel 2 DOF device was constructed. The device was designed to hold a 20 N load in a multitude of configurations. Using finite element analysis, it was determined that a FOS of 4 could be attained for the instrument end effector and instrument shaft.

Guiding the design of the end effector were constraints including a maximum 12 mm cylindrical diameter, the use of cable driven mechanisms, and providing multiple degrees of freedom, all while maintaining space for sensor cabling — a 2.5 × 5 mm channel — for each end effector jaw.

It was determined that stainless steel alloy 440C with a yield strength of 448 MPa had to be used for the majority of the end effector components. Finite element analysis was conducted on the ultrasound sensor jaw and results showed that heat treated 440C alloy would be required to raise its FOS to 4.

A heat treating procedure was developed and tested, resulting in an ultimate tensile strength conservatively estimated to be 1650 MPa using the 440C alloy. Two draw backs exist. Pre-machining is required to heat treat the part in a close-to-completion geometry to reduce the effects of internal stresses. Post heat treatment machining is then required to eliminate the effects of pitting and warpage. This leads to a higher cost of manufacturing. The second drawback is the brittle nature of the heat treated steel. During post heat treatment machining, the parts can crack and be rendered useless. Additionally, a brittle fracture during a minimally invasive procedure could be catastrophic for the device and dangerous for the patient.

In a comparative study between untreated and heat treated 440C alloy, the performance of the selected pins was assessed. In the untreated case, the pin was able to maintain 364 N of load without breaking. The study was not carried to failure because the pin could significantly outperformed the forces introduced by the end effector. It was seen that the pin could sustain 178 N of force without any visible permanent deformation. The pins were deemed appropriate because of the ability to resist the expected loads.

In addition to the design of the end effector, all other required sub-systems were designed. This includes the means to actuate the grasper jaws, hold associated electronics, route power, tension

the actuation cables, twist the end effector up to 90° in either direction, measure post gear head backlash, and hold the device.

The motor housing was made entirely of stainless steel alloy 304. This sub-system includes a method to easily mount and dismount other components including: actuation motors, post gear head encoders, the handle and electronics for motor controllers and future strain gauge measurement. The housing also includes a device to easily rotate the end effector into 11 discrete positions over a 180° range. Twisting did not have a large effect on the elongation of cables.

Future work for this system includes making and integrating sensor specific jaw geometries, and mounting strain gauges to the linkages and calibrating their output to a known device position and applied load.

Chapter 4

Electronics and Control System

4.1 Overview

The base electrical system of the device was designed to use commercially available components: a tactile sensor and corresponding data acquisition system provided by Pressure Profile Systems Inc., with libraries for integration on a personal computer; an ultrasound transducer including the same, provided by Blatek, Inc.; and motors with controllers using a proportional integral derivative (PID) control scheme, provided by Maxon Precision Motors, Inc. This chapter covers the implemented control system, and outlines the sensors used to demonstrate the control system in the absence of tactile and ultrasound sensors.

4.2 Control of the End Effector

A demonstrative control system is presented to examine the performance of the design. In doing so, the modelled system only physically controls half of the designed end effector. This is due to the symmetry of the end effector. Symmetric movement was deemed appropriate because of the compliance of the tissue, which can deform to the jaw faces in varying configurations.

The governing equations for the position of the end effector and sliders were first derived. Figure 4.1 depicts one half of the grasper and the symbols representing the linkage lengths and joint angles. Table 4.1 defines the variables in the model. Equations 4.1 through 4.6 show the

reverse kinematics starting with the desired position of the jaw. The tissue thickness for palpation, t_d, is defined to be approximately in the middle of the jaw length (Point #8 in Figure 4.1). The angle of palpation, θ_d, is defined to be the angle of the jaw from the x-axis. Equations 4.7 through 4.16 show the forward kinematics starting with the slider positions from the origin, $\vec{l}^*_{31}$ and $\vec{l}^*_{36}$.

The reverse kinematics equations are used in the real time control system on the constructed prototype. Sensor inputs on the end effector are used to determine the desired new thickness, t_d, and angle, θ_d, of palpation, should it be changed. The known thickness and angle are then used to determine the unknown slider positions, $\vec{l}^*_{31}$ and $\vec{l}^*_{36}$, which are inputs controlled physically by motors.

The forward kinematics equations are used to model the presented control system with MATLAB. In this case, the known slider positions, $\vec{l}^*_{31}$ and $\vec{l}^*_{36}$, dictate the unknown end effector position and orientation — the thickness and angle of palpation. Their path from one position to the next also dictates the path from one end effector position to the next. With a desired change in thickness and angle, the forward kinematics equations will model the path of thickness and angle actually taken.

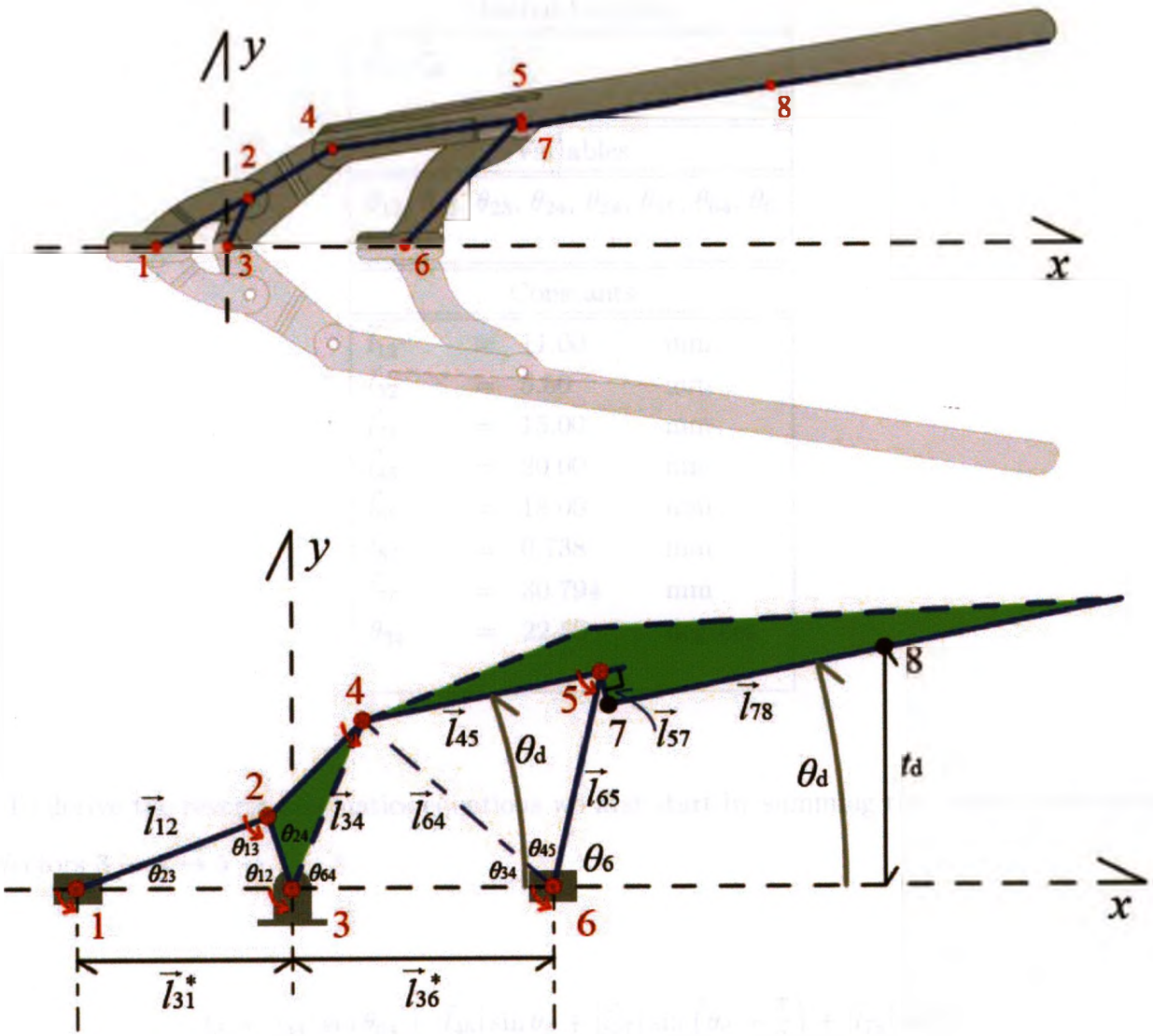

Figure 4.1: Kinematic model of the grasper.

Table 4.1: Table of variable definitions from Figure 4.1.

Desired Inputs		
t_d, θ_d		
Desired Outputs		
$\vec{l}^*_{31}$, $\vec{l}^*_{36}$		
Variables		
θ_{12}, θ_{13}, θ_{23}, θ_{24}, θ_{34}, θ_{45}, θ_{64}, θ_6		
Constants		
$\vec{l}_{12}$	= 11.00	mm
$\vec{l}_{32}$	= 5.50	mm
$\vec{l}_{34}$	= 15.00	mm
$\vec{l}_{45}$	= 20.00	mm
$\vec{l}_{65}$	= 18.00	mm
$\vec{l}_{57}$	= 0.738	mm
$\vec{l}_{78}$	= 30.794	mm
θ_{24}	= 22.50	degrees

To derive the reverse kinematics equations we first start by summing the vertical components of Vectors $3 \rightarrow 4 \rightarrow 5 \rightarrow 7 \rightarrow 8$:

$$t_d = \left|\vec{l}_{34}\right| \sin\theta_{64} + \left|\vec{l}_{45}\right| \sin\theta_d + \left|\vec{l}_{57}\right| \sin\left(\theta_d - \frac{\pi}{2}\right) + \left|\vec{l}_{78}\right| \sin\theta_d$$

$$\therefore \theta_{64} = \sin^{-1}\left(\frac{t_d - \left|\vec{l}_{45}\right| \sin\theta_d - \left|\vec{l}_{57}\right| \sin\left(\theta_d - \frac{\pi}{2}\right) - \left|\vec{l}_{78}\right| \sin\theta_d}{\left|\vec{l}_{34}\right|}\right). \tag{4.1}$$

We must find two solutions of t_d because the manipulator has a closed design. In an open, or serial configuration, one DOF is joined to the next DOF or end effector and thus, one DOF relatively controls the position of subsequent DOFs. In a closed configuration, such as that presented,

multiple DOFs control the same subsequent DOFs. In this case, multiple DOFs control the jaws. Summing the vertical components of Vectors $6 \rightarrow 5 \rightarrow 7 \rightarrow 8$, we get:

$$\begin{aligned} t_d &= \left|\vec{l}_{65}\right| \sin\theta_6 + \left|\vec{l}_{57}\right| \sin\left(\theta_d - \frac{\pi}{2}\right) + \left|\vec{l}_{78}\right| \sin\theta_d \\ \therefore \theta_6 &= \sin^{-1}\left(\frac{t_d - \left|\vec{l}_{57}\right| \sin\left(\theta_d - \frac{\pi}{2}\right) - \left|\vec{l}_{78}\right| \sin\theta_d}{\left|\vec{l}_{65}\right|}\right). \end{aligned} \tag{4.2}$$

On the triangle defined by Joints $1, 2, 3$, we can use the sine law to solve for θ_{23} and for θ_{13}:

$$\begin{aligned} \frac{\left|\vec{l}_{32}\right|}{\sin(\theta_{23})} &= \frac{\left|\vec{l}_{12}\right|}{\sin(\theta_{32})} \\ &= \frac{\left|\vec{l}_{12}\right|}{\sin(\pi - \theta_{24} - \theta_{64})} \\ \therefore \theta_{23} &= \sin^{-1}\left(\frac{\left|\vec{l}_{32}\right| \sin(\pi - \theta_{24} - \theta_{64})}{\left|\vec{l}_{12}\right|}\right) \end{aligned} \tag{4.3}$$

$$\begin{aligned} \therefore \theta_{13} &= \pi - \theta_{23} - \theta_{32} \\ &= \theta_{24} + \theta_{64} - \theta_{23}. \end{aligned} \tag{4.4}$$

Now, using Equation 4.1 and Equation 4.4, we can solve for the desired output $\vec{l}^*_{31}$, starting with the sine law on the triangle defined by Joints $1, 2, 3$:

$$\begin{aligned} \frac{\left|\vec{l}^*_{31}\right|}{\sin(\theta_{13})} &= \frac{\left|\vec{l}_{12}\right|}{\sin(\theta_{32})} \\ \therefore \left|\vec{l}^*_{31}\right| &= \frac{\left|\vec{l}_{12}\right| \sin(\theta_{13})}{\sin(\theta_{32})} \\ &= \frac{\left|\vec{l}_{12}\right| \sin(\theta_{13})}{\sin(\pi - \theta_{24} - \theta_{64})}. \end{aligned} \tag{4.5}$$

Again, because of the closed configuration of the manipulator, we must find two solutions, one

for $\vec{l}^{*}_{31}$, and one for $\vec{l}^{*}_{36}$. The solution for $\vec{l}^{*}_{36}$ is found by summing x-components:

$$3 \rightarrow 4 \rightarrow 5 = 3 \rightarrow 6 \rightarrow 5$$

$$\left|\vec{l}_{34}\right| \cos(\theta_{64}) + \left|\vec{l}_{45}\right| \cos(\theta_{\mathrm{d}}) = \left|\vec{l}^{*}_{36}\right| + \left|\vec{l}_{65}\right| \cos(\theta_{6})$$

$$\therefore \left|\vec{l}^{*}_{36}\right| = \left|\vec{l}_{34}\right| \cos(\theta_{64}) + \left|\vec{l}_{45}\right| \cos(\theta_{\mathrm{d}}) - \left|\vec{l}_{65}\right| \cos(\theta_{6}). \tag{4.6}$$

The forward kinematics are more easily proven separately rather than using the inverse kinematics equations in reverse order, because both of the output variables $\vec{l}^{*}_{31}$ and $\vec{l}^{*}_{36}$ are coupled with t_{d} and θ_{d}, making them difficult to separate. Forward kinematics equations are used in the modelling of the implemented control system, and are presented here. Starting from the triangle defined by Joints $1, 2, 3$, the cosine law is used to solve for θ_{32} and θ_{64}:

$$\left|\vec{l}_{12}\right|^{2} = \left|\vec{l}^{*}_{31}\right|^{2} + \left|\vec{l}_{32}\right|^{2} - 2\left|\vec{l}^{*}_{31}\right|\left|\vec{l}_{32}\right| \cos(\theta_{32})$$

$$\therefore \theta_{32} = \cos^{-1}\left(\frac{\left|\vec{l}^{*}_{31}\right|^{2} + \left|\vec{l}_{32}\right|^{2} - \left|\vec{l}_{12}\right|^{2}}{2\left|\vec{l}^{*}_{31}\right|\left|\vec{l}_{32}\right|}\right) \tag{4.7}$$

$$\therefore \theta_{64} = \pi - \theta_{32} - \theta_{24}. \tag{4.8}$$

Then, looking at the triangle defined by Joints $3, 4, 6$, we intermediately solve for the distance between Joints 6 and 4, $\vec{l}_{64}$, using the cosine law:

$$\left|\vec{l}_{64}\right|^{2} = \left|\vec{l}_{34}\right|^{2} + \left|\vec{l}^{*}_{36}\right|^{2} - 2\left|\vec{l}_{34}\right|\left|\vec{l}^{*}_{36}\right| \cos(\theta_{64})$$

$$\therefore \left|\vec{l}_{64}\right| = \sqrt{\left|\vec{l}_{34}\right|^{2} + \left|\vec{l}^{*}_{36}\right|^{2} - 2\left|\vec{l}_{34}\right|\left|\vec{l}^{*}_{36}\right| \cos(\theta_{64})}. \tag{4.9}$$

Knowing $\vec{l}_{64}$, we can use the cosine law to solve for θ_{34} on the triangle defined by Joints $3, 4, 6$, and again use the cosine law to solve for θ_{45} on the triangle defined by Joints $4, 5, 6$:

$$\left|\vec{l}_{34}\right|^2 = \left|\vec{l}_{64}\right|^2 + \left|\vec{l}^*_{36}\right|^2 - 2\left|\vec{l}_{64}\right|\left|\vec{l}^*_{36}\right|\cos(\theta_{34})$$

$$\therefore \theta_{34} = \cos^{-1}\left(\frac{\left|\vec{l}^*_{36}\right|^2 + \left|\vec{l}_{64}\right|^2 - \left|\vec{l}_{34}\right|^2}{2\left|\vec{l}^*_{36}\right|^2\left|\vec{l}_{64}\right|^2}\right) \tag{4.10}$$

$$\left|\vec{l}_{45}\right|^2 = \left|\vec{l}_{64}\right|^2 + \left|\vec{l}_{65}\right|^2 - 2\left|\vec{l}_{64}\right|\left|\vec{l}_{65}\right|\cos(\theta_{45})$$

$$\therefore \theta_{45} = \cos^{-1}\left(\frac{\left|\vec{l}_{64}\right|^2 + \left|\vec{l}_{65}\right|^2 - \left|\vec{l}_{45}\right|^2}{2\left|\vec{l}_{64}\right|^2\left|\vec{l}_{65}\right|^2}\right). \tag{4.11}$$

We can then solve for θ_6 with Equation 4.10 and Equation 4.11:

$$\theta_6 = \pi - \theta_{34} - \theta_{45}. \tag{4.12}$$

To solve for θ_d, we sum the x and y components of the vectors defined by Joints $3 \rightarrow 4 \rightarrow 5$, and $3 \rightarrow 6 \rightarrow 5$:

$$3 \rightarrow 4 \rightarrow 5 = 3 \rightarrow 6 \rightarrow 5$$

$$\left|\vec{l}_{34}\right|\cos(\theta_{64}) + \left|\vec{l}_{45}\right|\cos(\theta_d) = \left|\vec{l}^*_{36}\right| + \left|\vec{l}_{65}\right|\cos(\theta_6) \tag{4.13}$$

$$\left|\vec{l}_{34}\right|\sin(\theta_{64}) + \left|\vec{l}_{45}\right|\sin(\theta_d) = \left|\vec{l}_{65}\right|\sin(\theta_6). \tag{4.14}$$

Then we divide Equation 4.14 by Equation 4.13, and rearrange to solve for θ_d:

$$\tan(\theta_d) = \frac{\left|\vec{l}_{65}\right|\sin(\theta_6) - \left|\vec{l}_{34}\right|\sin(\theta_{64})}{\left|\vec{l}^*_{36}\right| + \left|\vec{l}_{65}\right|\cos(\theta_6) - \left|\vec{l}_{34}\right|\cos(\theta_{64})}$$

$$\theta_d = \tan^{-1}\left(\frac{\left|\vec{l}_{65}\right|\sin(\theta_6) - \left|\vec{l}_{34}\right|\sin(\theta_{64})}{\left|\vec{l}^*_{36}\right| + \left|\vec{l}_{65}\right|\cos(\theta_6) - \left|\vec{l}_{34}\right|\cos(\theta_{64})}\right). \tag{4.15}$$

Having solved for all angles, we can add the vertical components from Joints $6 \rightarrow 5 \rightarrow 7 \rightarrow 8$

to solve for t_d:

$$t_d = \left|\vec{l}_{65}\right| \sin(\theta_6) + \left|\vec{l}_{57}\right| \sin\left(\theta_d - \frac{\pi}{2}\right) + \left|\vec{l}_{78}\right| \sin(\theta_d). \tag{4.16}$$

The presented equations define the position of the jaws and the required slider positions. The sliders are set by cables attached to motors. In operation, it was desirable to have the palpation thickness, t_d, and palpation angle, θ_d, move linearly from current to desired values. The approach used was a continuous point-to-point motion. Though kinematically coupled, the thickness and angle were treated separately in the presented approach. Between the current palpation thickness and angle, and the desired thickness and angle, the path was broken down into multiple linear segments to lessen the computational burden compared to solving the linear movement of the end effector and subsequent motion of variables $\vec{l}^*_{31}$ and $\vec{l}^*_{36}$ analytically. This was necessary due to the coupled nonlinearity between $\vec{l}^*_{31}$ and $\vec{l}^*_{36}$, and t^*_d and θ^*_d. Instead, with a discretized path, the variables $\vec{l}^*_{31}$ and $\vec{l}^*_{36}$ were given a new position and a velocity with which to reach the position for each path segment (Figure 4.2). The higher the number of discrete points between the desired start and end positions, the more accurate the path. Figure 4.3 shows the effect of discretizing the desired path on the actual output path. The path shown in blue is due to the linear velocity of motors. The more points the path is broken into, the closer it is to the desired path. The number of steps between two different locations was chosen as the highest number of points that can be produced by the hardware controlling the motors. Path smoothing and velocity smoothing techniques were implemented to prevent piecewise continuous movement, resulting in a smooth motion of the grasper jaws. Within a certain error margin of reaching a desired point, the slider movement for the next desired point was updated, providing smooth motion between points. Without path smoothing, the velocity at each intermediate point between current and desired values would be zero, resulting in a jerky movement of the jaw.

In order to set a desired value for the jaw position, it is required that, in the case that a position is not kinematically possible, the jaw should move to the closest possible position. This is a necessity when used with sensor feedback. If the implemented control system were to provide a position that is impossible to reach due to the jaw geometry, the program running the system

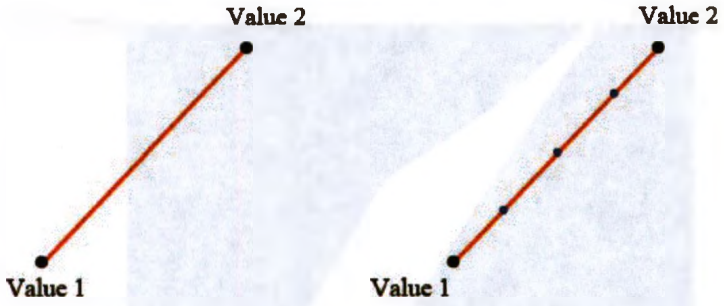

Figure 4.2: Discretized path trajectory.
Left: Desired path from Value 1 to Value 2. Right: Discretized path from Value 1 to Value 2.

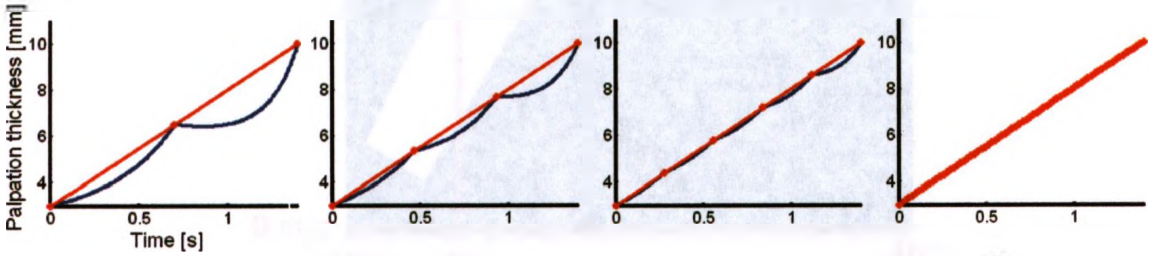

Figure 4.3: Reducing the step size of the path drawn by variable t_d, changing from 3 mm to 10 mm. Desired path shown as the straight red line. Actual output path shown as the piecewise continuous blue line. Discontinuity points are the discretized path points. Left to right: 2 steps, 3 steps, 5 steps, 71 steps.

could freeze, or the grasper may experience lock-up or failure.

In order to implement a control system, a large scale model of half the grasper was built, as shown in Figure 4.11. To prevent damage to the system, the work area of all possible thickness and angle positions of the end effector were mapped out onto a reference image. Using the reverse kinematics equations, the workspace was determined for the large scale design for thickness values ranging from 0 to 120 mm in 0.1 mm increments, and for angle values ranging from -10 to 40° in 0.05° increments. The result was a 1000 × 1200 pixel image coloured white where the end effector position was possible, and black where the position was not possible (Figure 4.4).

The resultant image was refined to remove sharp corners and add a single pixel wide outline of the work area. Sharp corners were rounded for cases in which the jaw position was to follow the outer edge. With rounded corners, the change of thickness and angle are more gradual. A single pixel outline of the workspace was included for the determination of its outer edge, the physical limit of the end effector.

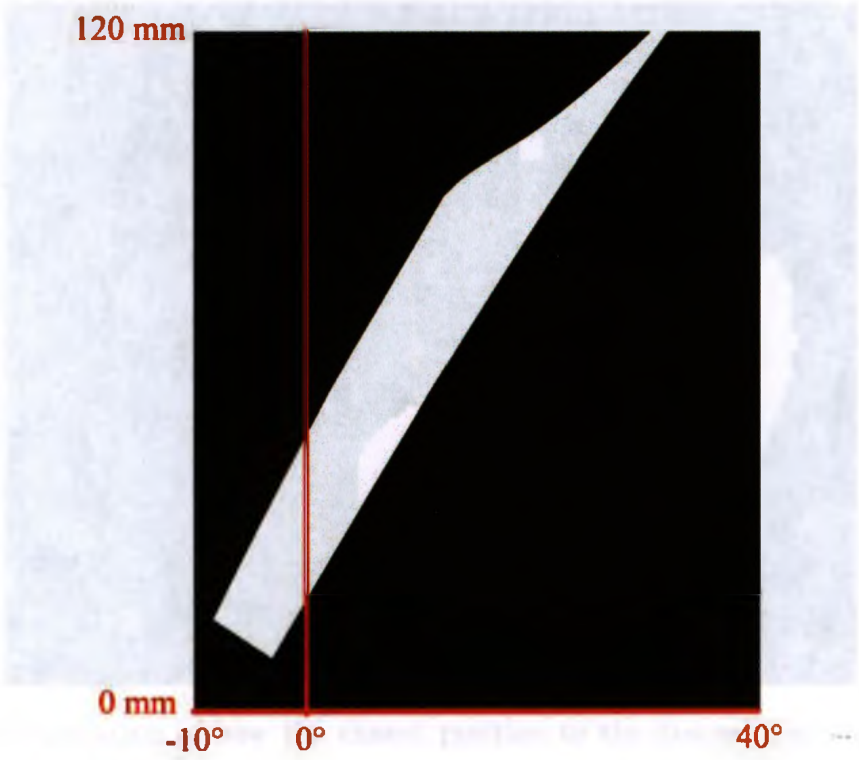

Figure 4.4: Workspace of the large scale prototype.

Using the edited image, a function was developed to determine whether or not the desired location was possible. By providing the desired thickness and angle and converting them into their associated pixel values, the image is used essentially as a lookup table of possible positions. If the desired location was within the workspace, then the reverse kinematics equations are used to determine the appropriate slider positions. If the desired location is not within the workspace, then the chosen location is selected as the one with the smallest pixel distance to the desired location, as shown in a general workspace in Figure 4.5. This is done by following the outer edge of the workspace along its complete path. The distance of each pixel on the outer edge to the desired position pixel is calculated, storing in memory which pixel had the shortest distance.

For cases in which two minimum distances exist, the function also includes inputs for the previous jaw position, choosing the location closest to the previous position (Figure 4.6).

MATLAB was used to model the trajectory of the jaw given two inputs — the current position of thickness, t_{current}, and angle, θ_{current}, called Position 1, and the desired position, t_{desired} and θ_{desired}, called Position 2. The number of intermediate steps between positions is determined by

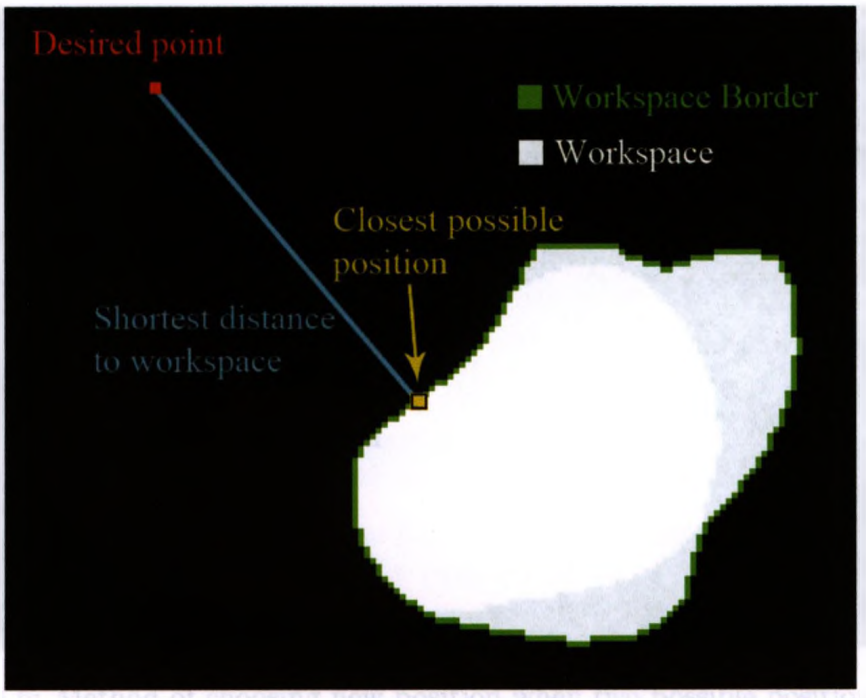

Figure 4.5: A demonstration of how the closest position to the desired position is chosen when outside of the workspace.

setting a maximum allowable change in both thickness and angle. The change in value of thickness and angle between Position 1 and Position 2 are divided by their maximum allowable change per step, respectively. The result with a higher number of steps is chosen as the number steps to split the path into. Figure 4.7 shows the change from a thickness and angle of 70 mm and 10° to 30 mm and 0°. In this figure, the chosen maximum allowable change for thickness and angle per step was 50 mm and 50°, resulting in no discretization of the path. The red line shows the desired path between points, a straight line, and the blue line shows the path taken. The image on the right side of the figure shows the path trajectory in the workspace image. The time scale shown was determined by setting variables that dictate the time between consecutive points. The model does not take into account the time taken to communicate with the motor controllers, or the actual velocity profile of the motors. The same position inputs are shown in Figure 4.8 but with a maximum allowable change of thickness and angle per step of 2 mm and 2°, resulting in 20 intermediate points. It is evident here that with a smaller maximum allowable change per step, the higher the degree of discretization, and the closer the actual path is to the desired path.

The MATLAB program to generate the path taken first determines the closest possible current

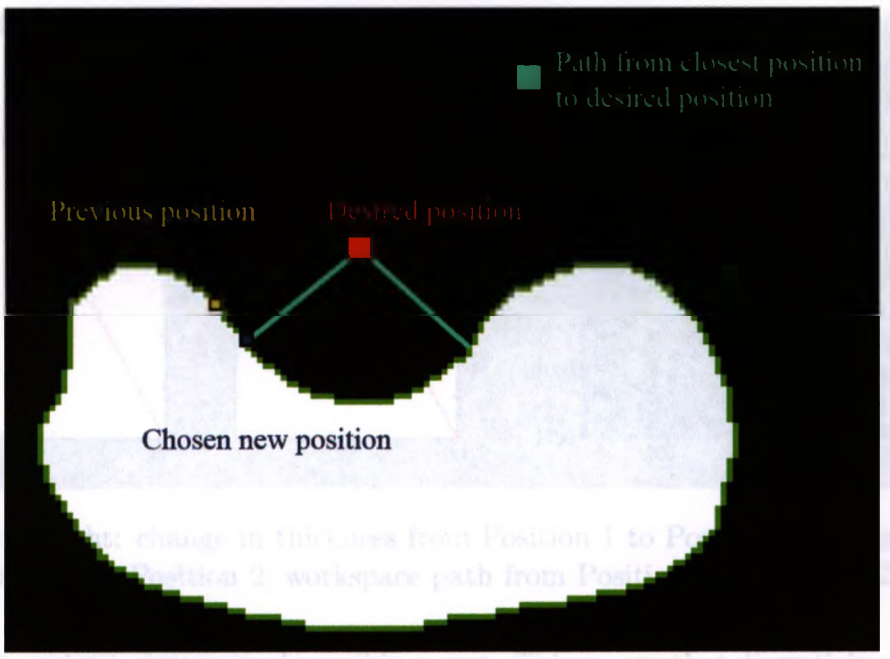

Figure 4.6: Method of choosing new position when two possible positions exist.

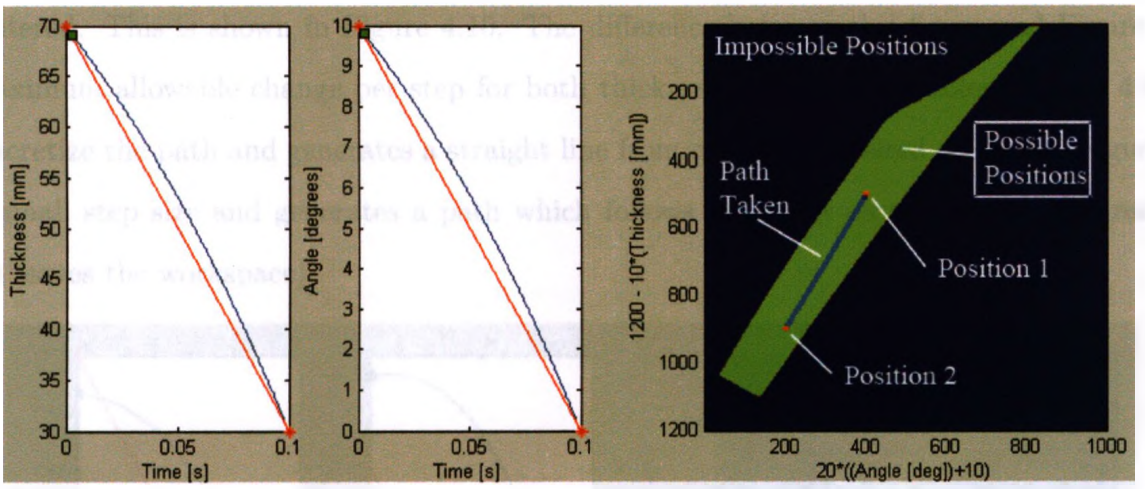

Figure 4.7: Left to right: change in thickness from Position 1 to Position 2, change in angle from Position 1 to Position 2, workspace path from Position 1 to Position 2.

position, and the closest possible desired position. A path is then discretized between the two points. This means that if either of the positions lies outside of the workspace, and no discretization is necessary, then the path will not follow the closest possible path to that desired. Figure 4.9 shows the desired path in yellow, the closest possible path that follows the desired path up to its workspace limit in black, and the path generated with no discretization — a straight line from current to desired values. Since the discretization algorithm adds points along the desired path,

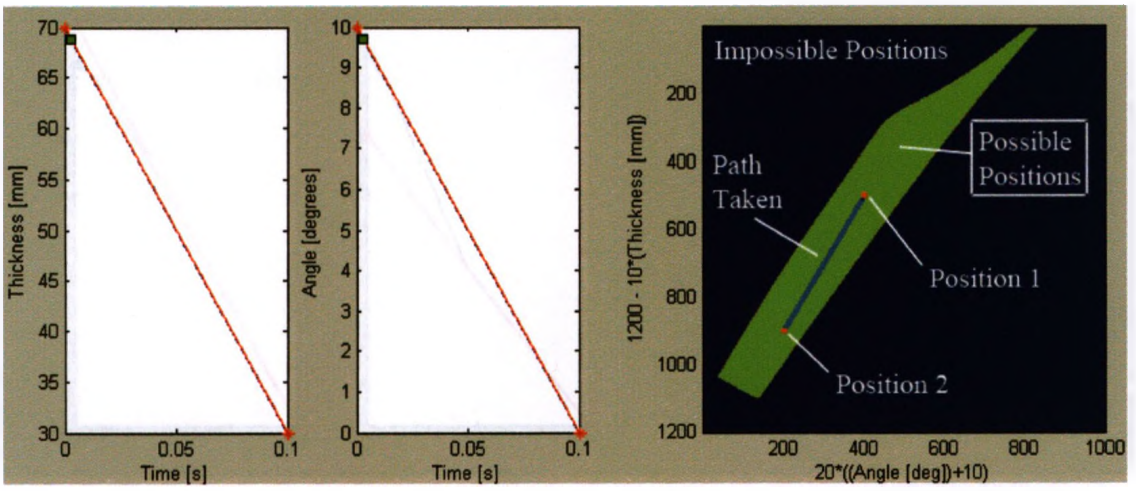

Figure 4.8: Left to right: change in thickness from Position 1 to Position 2, change in angle from Position 1 to Position 2, workspace path from Position 1 to Position 2.

each intermediate point is determined possible or not. This means that discretizing the path causes the path generated to follow the desired path, only deviating from it when the workspace limit is encountered. This is shown in Figure 4.10. The difference between this figure and Figure 4.9 is the maximum allowable change per step for both thickness and angle variables. Figure 4.9 does not discretize the path and generates a straight line from current to desired positions. Figure 4.10 has a small step size and generates a path which follows as closely as possible the desired path (which leaves the workspace).

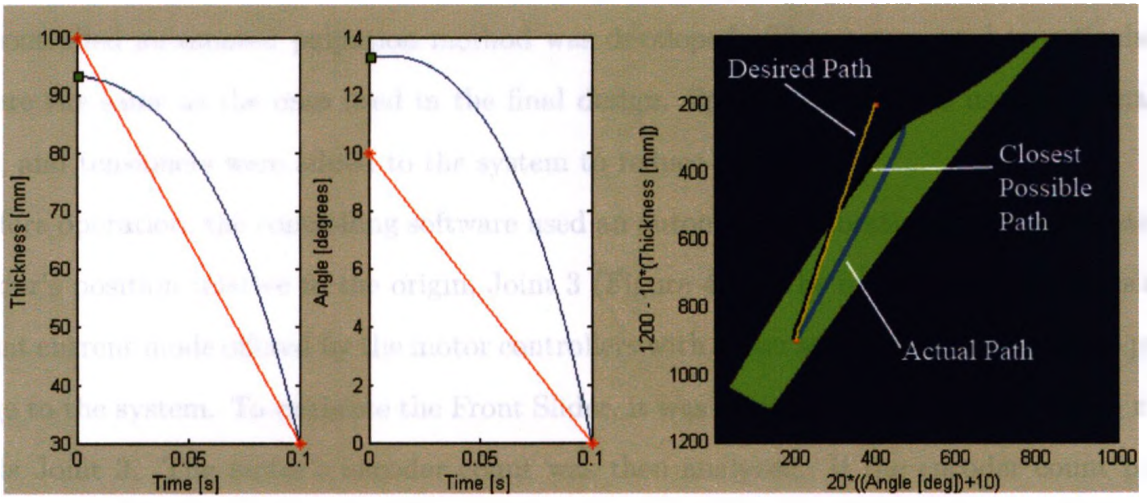

Figure 4.9: With no path discretization, the actual path does not follow the closest possible path (Yellow line: desired path, Black line: closest possible path, Light blue line: actual path).

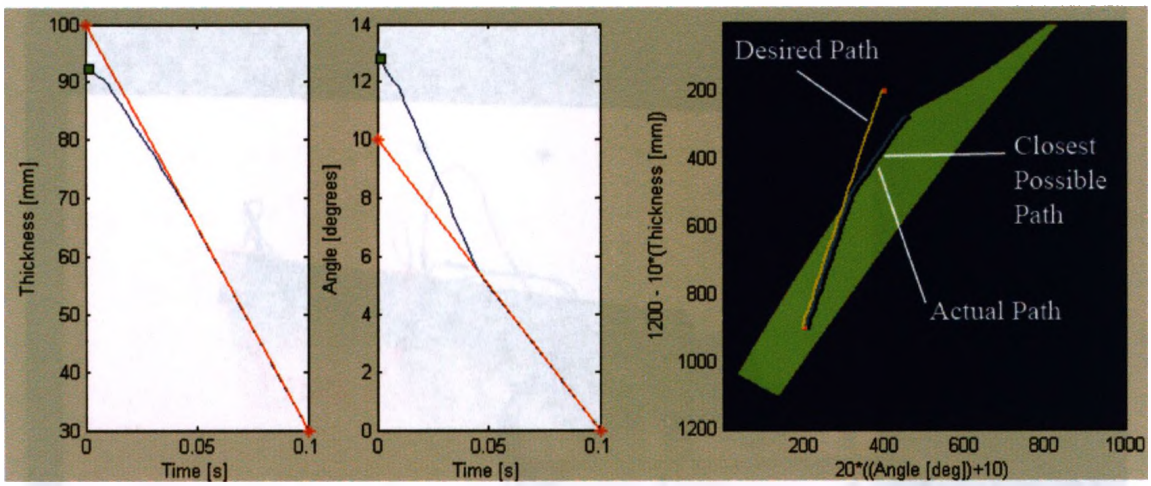

Figure 4.10: With a discretized path, the actual path approaches the closest possible path (Yellow line: desired path, Black line: closest possible path, Light blue line: actual path).

4.3 Sensor Feedback

During the design phase of the project, it was not known if the ultrasound and tactile sensors would be mounted to the first prototype. In the case of unexpected failure, it would be an undesirable expense. In order to demonstrate the use of the end effector jaws with feedback using a closed loop palpation scheme, a large scale version of half of the grasper was constructed, as shown in Figure 4.11. Rather than using tactile sensing, two force sensing resistors (FSR) were used to obtain data related to the total force of palpation and the angle of palpation. In this manner, a force-controlled automated palpation method was developed. The motors used to articulate the jaw were the same as the ones used in the final design. Spectra cables were used to actuate the sliders, and tensioners were added to the system to reduce backlash.

Before operation, the controlling software used an automated calibration function to determine the slider's position relative to the origin, Joint 3 (Figure 4.1). The motors were driven using the constant current mode offered by the motor controllers with a user set maximum velocity to prevent damage to the system. To calibrate the Front Slider, it was set into constant current mode moving towards Joint 3. The motor's encoder count was then analyzed. If the encoder count position was consistently the same for 100 readings in a row, the slider was assumed to be immobile and the encoder position was recorded. The home position was then calculated as the recorded count minus the number of encoder counts required to move the slider half of its own length, minus the

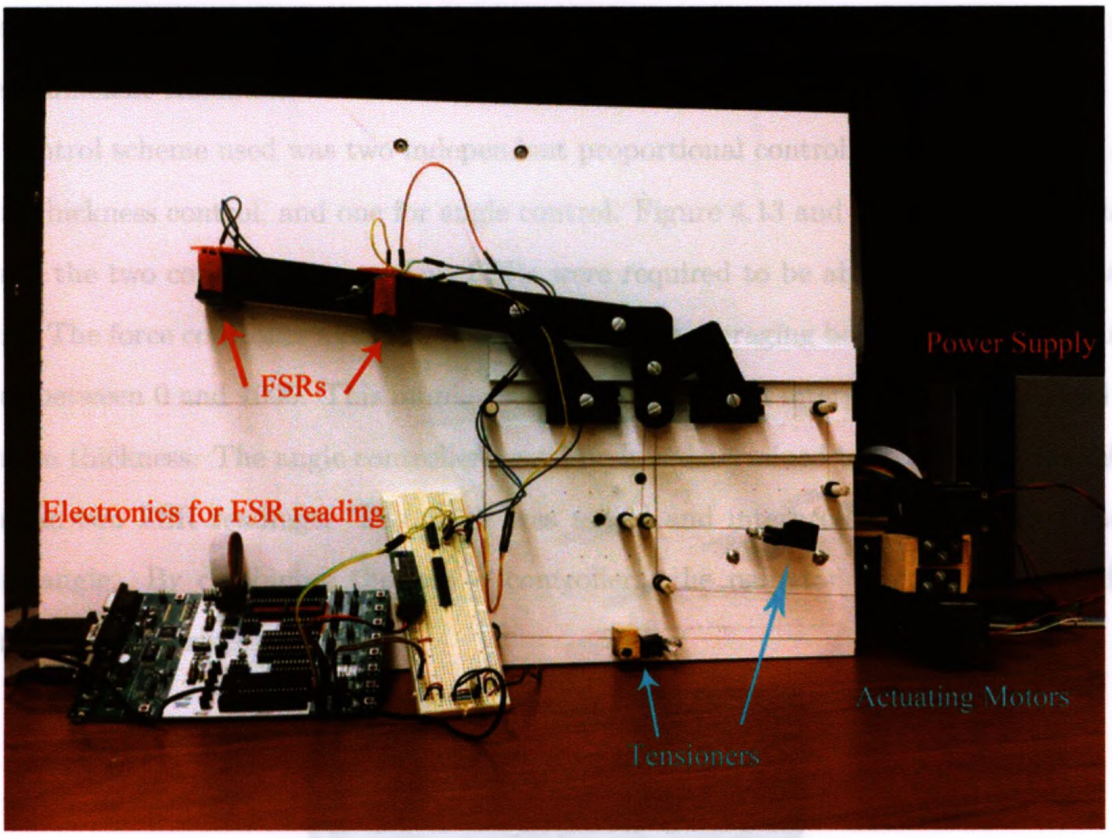

Figure 4.11: A picture of the large scale model of the grasper jaw with identifying features.

radius of the pin at Joint 3 (Equation 4.19). The same technique was used for the Back Slider.

$$\text{Zero Position} = \text{Encoder Count at Immobile Position} \tag{4.17}$$

$$- \frac{\left(\frac{\text{Slider Length}}{2} + \text{Pin Radius at Joint 3}\right)}{2\pi\,(\text{Cable Pulley Diameter})} \tag{4.18}$$

$$- \frac{(\text{Encoder Pulses Per Revolution})\,(\text{Gear Head Ratio})}{2\pi\,(\text{Cable Pulley Diameter})} \tag{4.19}$$

The FSRs used were Part No. 400 from Interlink Electronics. They were adhered to the large scale palpator jaw with double sided tape and a rounded bumper was mounted to them to try to distribute the load on them evenly and repeatably from any direction of force (Figure 4.12). The FSRs became active with about a 0.5 N force and were given an upper limit of 10 N, set in software. The scale from 0 to 10 N was normalized to 1, then multiplied by 1000. The reason for scaling the sensor output to a number between 0 and 1000 was to make use of integer numbers

to decrease the computation time as compared to floating point numbers. The scale of 0 to 1000 exhibited sufficient resolution for the control system.

The control scheme used was two independent proportional controllers (P controllers): one for palpation thickness control, and one for angle control. Figure 4.13 and Figure 4.14 show the block diagram of the two control systems. Two FSRs were required to be able to interpret the angle of palpation. The force controller's reading was calculated by averaging both FSR values, resulting in a number between 0 and 1000. This number was then scaled and interpreted as a required change in palpation thickness. The angle controller's reading was determined by calculating the difference between the two FSR readings. The result was scaled and interpreted as a required change in palpation angle. By combining the two P controllers, the palpator jaw is able to conform to approximately flat surfaces.

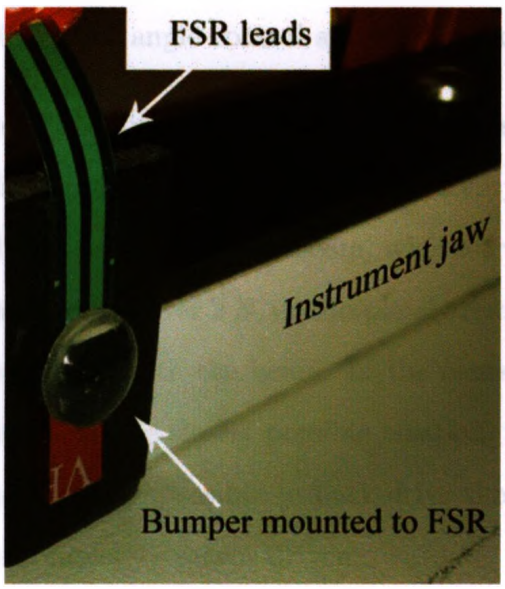

Figure 4.12: The mounted FSR.

For demonstration purposes, a desired palpation force of 2 N was used along with a desired palpation angle of 0°. Shear forces do have an affect on the sensor reading but were not taken into account in the control scheme and were attempted to be minimized by using materials that would easily slide against each other. This was an acceptable simplification because some sliding always occurs during lung palpation.

To demonstrate the designed automatic palpation process, a flexible plastic beam was used

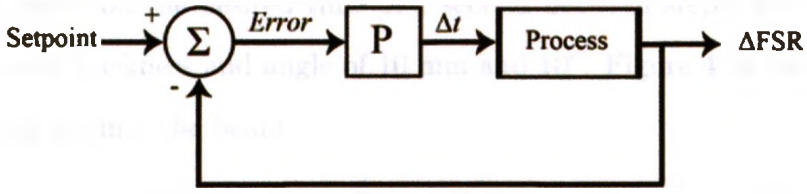

Figure 4.13: The thickness control system block diagram.

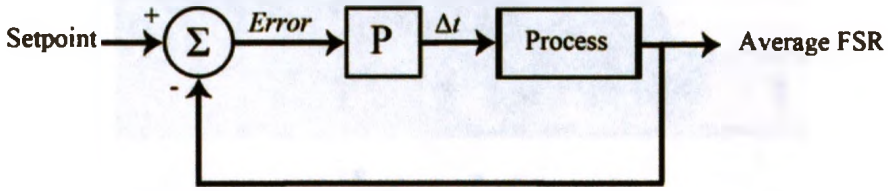

Figure 4.14: The angle control system block diagram.

to palpate against. The beam's flexibility shows that the system is robust and can work around changing object geometries. Similarly, lung tissue has some flexibility. During testing, the palpator jaw moved such that it was always flat against the beam, whether the beam pushed hard against the jaw, increasing the palpation force to over 2 N, or completely removed, forcing the jaw to slowly close until it made contact once again with the beam. In the cases where the jaw was physically unable to reach the beam, it moved to the closest possible position, not necessarily in contact with the beam. It is also noted that it was impossible to back-drive the motors by pushing or pulling on the jaw. All movement was completely sensor driven.

FSR reading and P controller calculations were done by an Atmel AVR ATmega644 microcontroller, sending values to Windows XP Professional serially using the RS-232 communication protocol. The remainder of the control loop was programmed for Windows XP Professional using the Nokia QT libraries and C++. This method was chosen for demonstrative purposes because speed was not an issue, so a low, infrequent sampling frequency caused by Windows scheduling was acceptable. Furthermore, libraries were provided for the motor controllers to work over a serial port on Windows. To use the motor controllers with embedded hardware would require recreating the library functions, a task outside of the scope of this thesis. The speed of the motors

was calculated based on the desired time of 1 second between steps, with a maximum allowable change per step for thickness and angle of 10 mm and 10°. Figure 4.15 shows a series of photos of the jaw palpating against the beam.

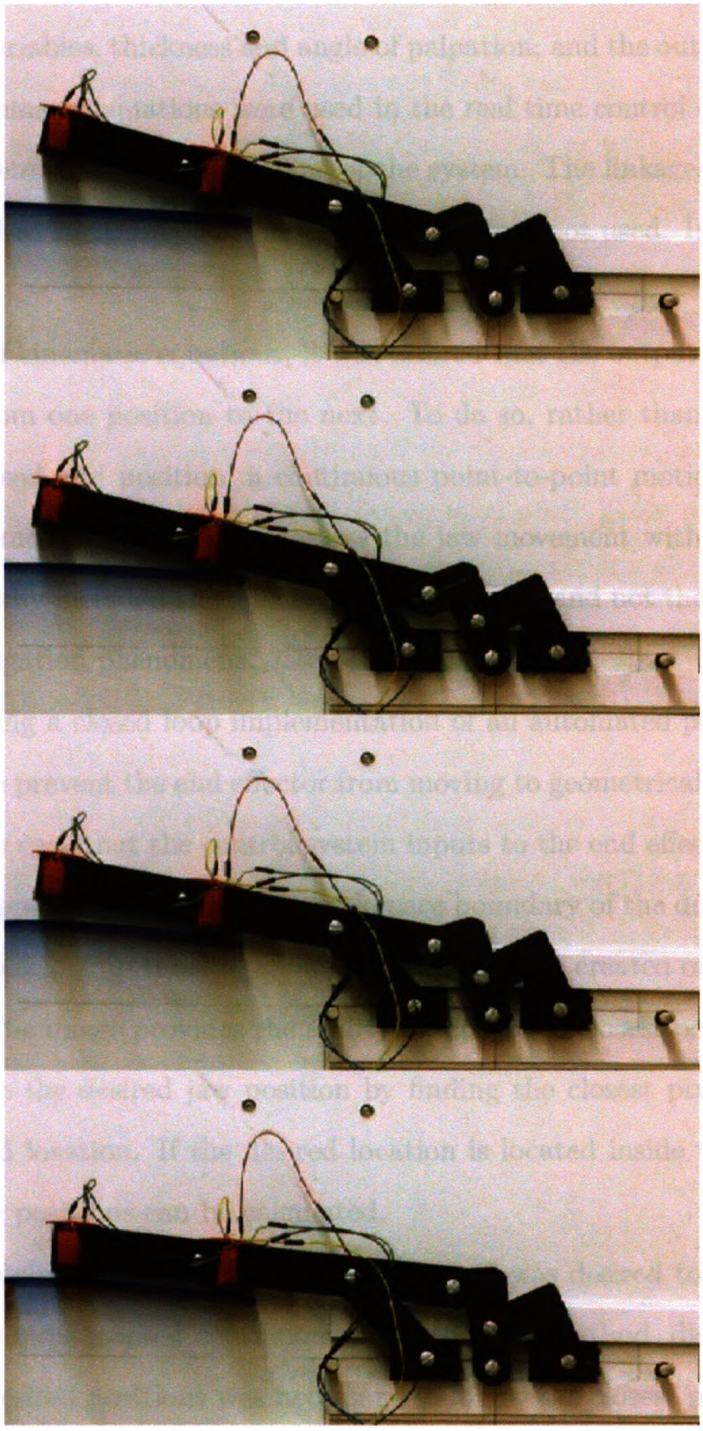

Figure 4.15: A series of pictures showing the palpator jaw converging to the position of the palpated object.

4.4 Conclusions

In the development of the control system, a kinematic model was first developed for the end effector jaw, modelling only half of it due to symmetry. Reverse and forward kinematic equations were derived for the input variables, thickness and angle of palpation; and the output variables, the slider positions. Reverse kinematic equations were used in the real time control of the system. Forward kinematic equations were used in the modelling of the system. The linkages of the device were not serially connected, and as such, robotic linkage equations were not used. Instead, standard vector math was employed.

With the developed kinematic equations, it was desired that the output values of thickness and angle move linearly from one position to the next. To do so, rather than deriving equations for the required motor speed and position, a continuous point-to-point motion algorithm was used. A model was programmed in MATLAB to assess the jaw movement with the desired movement function. This model only included the kinematics of the robot, and not the motor position profile, backlash, or cable elongation phenomena.

Before demonstrating a closed loop implementation of an automated palpation process, a system was put in place to prevent the end effector from moving to geometrically impossible positions. This was desired in the case that the control system inputs to the end effector were not physically possible, which can happen when nearing the workspace boundary of the device. As a preventative measure, an image based lookup table of allowable positions was created on a large scale mock up of the jaw geometry. The image provides the ability to locate the closest possible physical position of the jaw geometry to the desired jaw position by finding the closest pixel in the workspace to the pixel in the desired location. If the desired location is located inside the workspace, then an exact solution of slider positions can be calculated.

Along with maintaining the closest possible position, it was desired to follow the closest possible path. Due to the implemented continuous point-to-point method, discretization of the path between current and desired positions was necessary to follow the closest possible path. Although many levels of discretization exist, the more there are, the slower the device moves due to the communication time between the personal computer (PC) and the motor controllers. The path

step size was chosen empirically.

To demonstrate the desired movement of the jaw geometry, a large scale prototype was built using a Windows PC as the control system. The sampling frequency was slow enough in this demonstration that the effect of using a PC as a control system was negligible. The mock design made use of two force sensing resistors (FSR). The two FSRs had the ability to sense if the overall force on a flat object was equally distributed over the sensors, and whether or not both sensors were in contact with a flat surface.

To implement the control system, two P controllers were used, using both FSRs as inputs. The first averaged the FSR readings, gaining insight on the total applied load on the palpated surface. The second subtracted one FSR reading from the other, giving insight on the current angle to the palpated surface. This control system was only used for demonstration purposes, and in fact the real control system using tactile and ultrasound sensor inputs will likely be different.

The implemented control system performed the tracking of a flexible plastic beam, showing robustness in the control system. The jaw was able to settle on, and track the motion of the beam.

As a proof of concept, no quantitative results were collected. It was noticed however that in some positions, due to the selected jaw geometry, that there was a degree of sliding. This could be minimized by using a different path generation scheme or using slightly different link geometries. Ultimately, the problem is that for each possible thickness and angle there exists only one geometric position. For example, with a constant thickness of palpation, and a change from negative to positive palpation angle, the jaws will inherently have to move forward. This effect could be eliminated with the addition of one more degree of freedom to compensate for the undesired sliding motion.

Chapter 5

Validation of the Final Prototype

5.1 Introduction

This chapter describes the final prototype. It will show the final constructed prototype and outline the main features of the design. A number of experiments are used to validate the workspace of the mechanism and test its load carrying capacity compared to the results of the finite element analysis conducted in Chapter 3. The control system developed in Chapter 4 is implemented and qualitatively assessed. Throughout each section, the strengths and weaknesses of the designed mechanism are discussed.

5.2 Overview of the Final Prototype

This section presents images of the final prototype, based on the design presented in Chapter 3. Before detailed images of the end effector and motor housing are shown, the fully constructed prototype is presented from several different angles. First, in Figure 5.1, the design in its entirety is displayed. The end effector is in a jaws-closed configuration, and the wires leaving the back of the handle are used to power and communicate with the motor controllers. A closer view of the handle and installed electronics is displayed in Figures 5.2 and 5.3, showing two different views of the instrument handle. Figure 5.2 shows the end effector twisting mechanism, the motors, the gear head shaft encoders, the motor housing, the handle, and the motor controllers. In Figure 5.3

all the same is visible but the motors.

Figure 5.1: Entire instrument assembled.

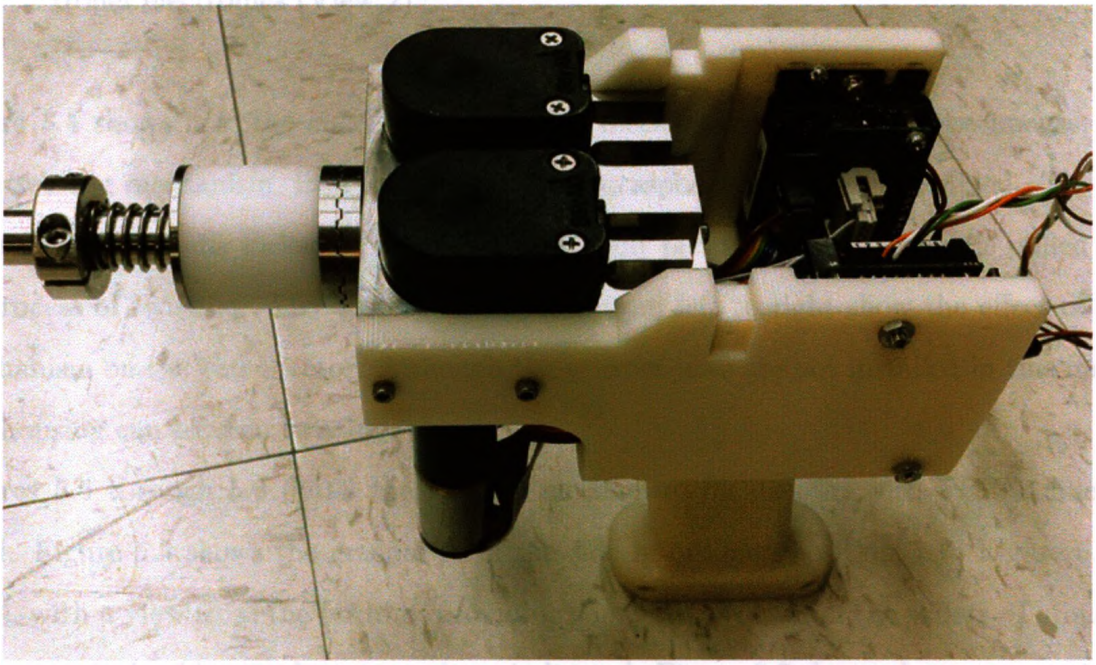

Figure 5.2: The assembled handle holding the motor housing, encoders, motors, and motor controller electronics (View 1).

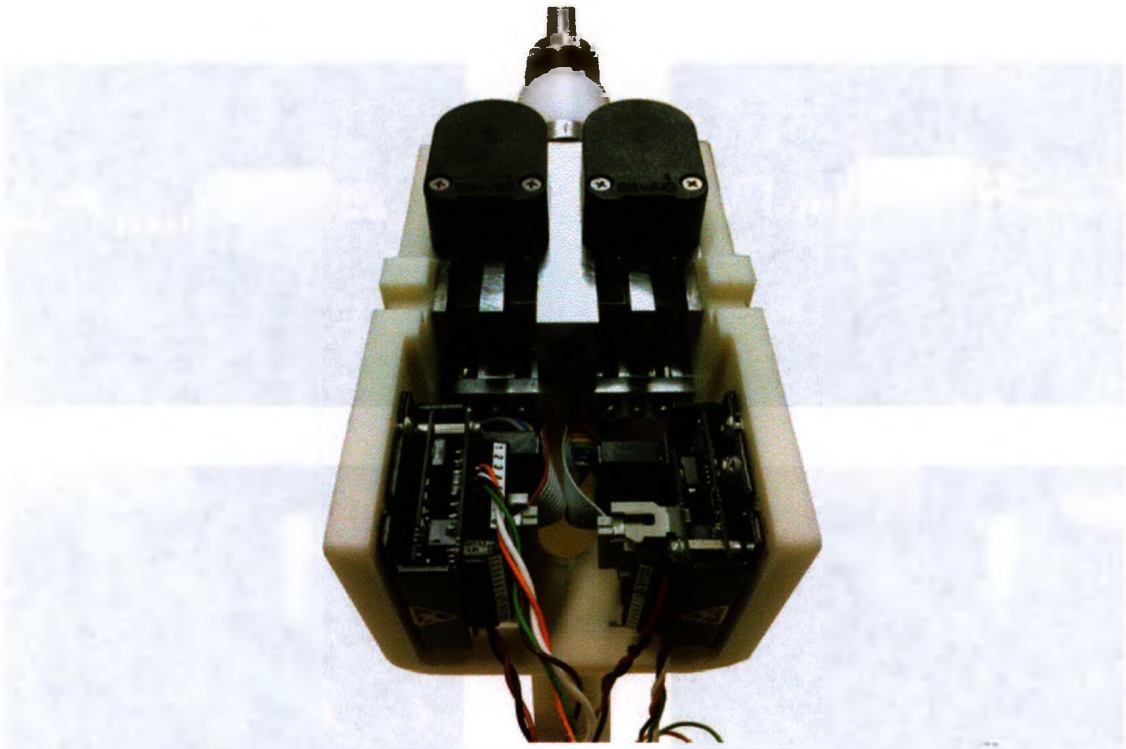

Figure 5.3: The assembled handle holding the motor housing, encoders, motors, and motor controller electronics (View 2).

Figure 5.4 shows how the end effector twisting mechanism works. In these images, nothing but the twisting mechanism, instrument shaft, and grasper housing are assembled. The top left picture shows the handle locked in place. The top right picture shows the handle pulled out and in the process of twisting. The bottom two photos from left to right show the effect of twisting the mechanism on the end effector. Although the grasper jaws are not installed in this image, the grasper housing can be seen twisting.

Figures 5.5 through 5.9 detail the grasper mechanism on its own with PEEK slider covers attached. Figure 5.5 shows the grasper from the side in an open position, and Figure 5.6 shows the same, with a view from the bottom, providing some visual detail of the sliders. Through holes for the uninstalled cables can be seen and are indicated. Figure 5.7 shows the grasper in its closed position. In this position, its outer diameter is 12.7 mm. In all of these images, the pins used for the linkage joints can be seen to be swaged in permanently. Eventual installation of jaws with attached tactile and ultrasound sensors would require drilling the pins out.

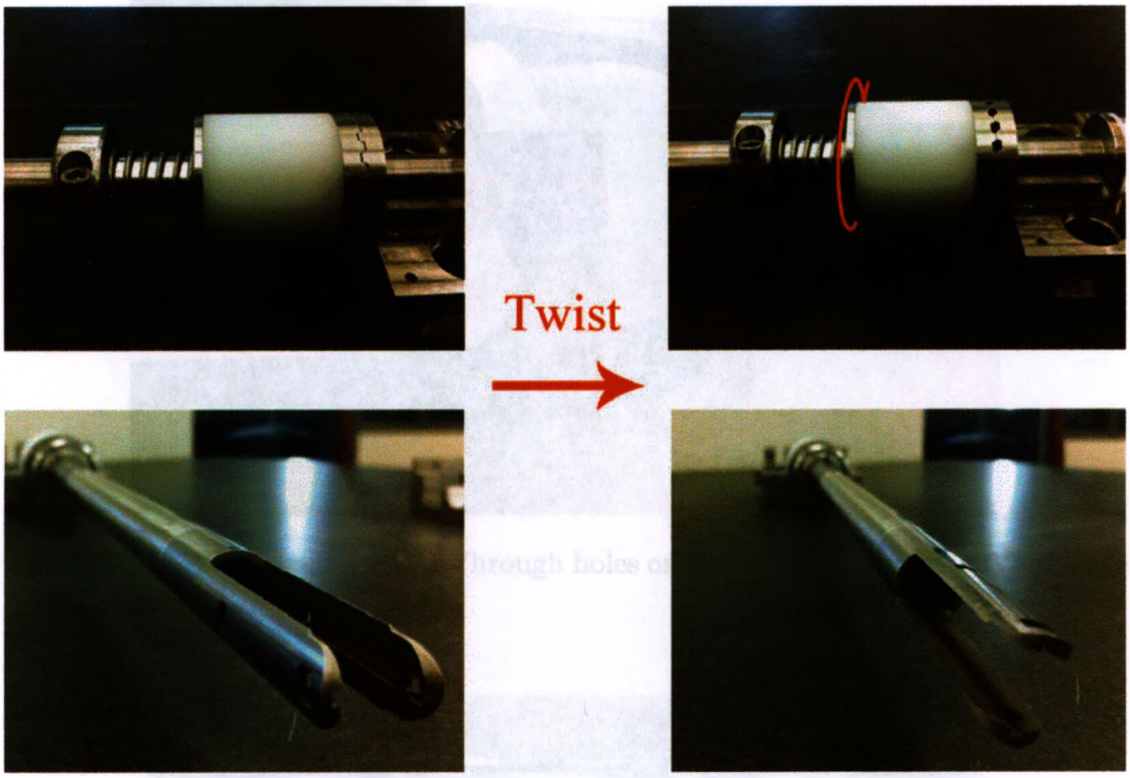

Figure 5.4: Twisting of the end effector (grasper mechanism not included).

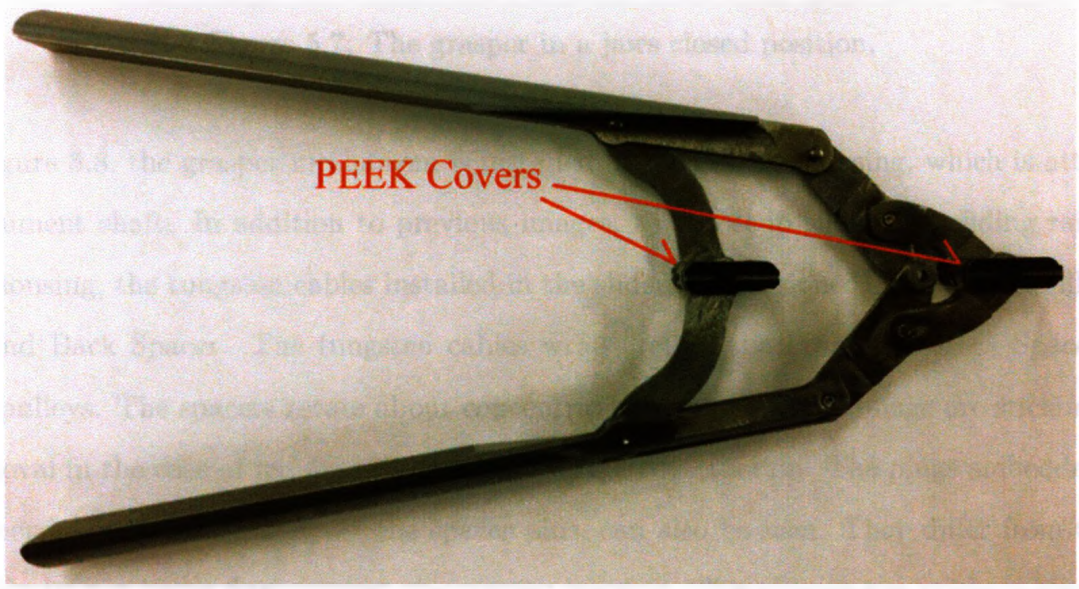

Figure 5.5: The grasper mechanism with black-coloured PEEK covers on the sliders.

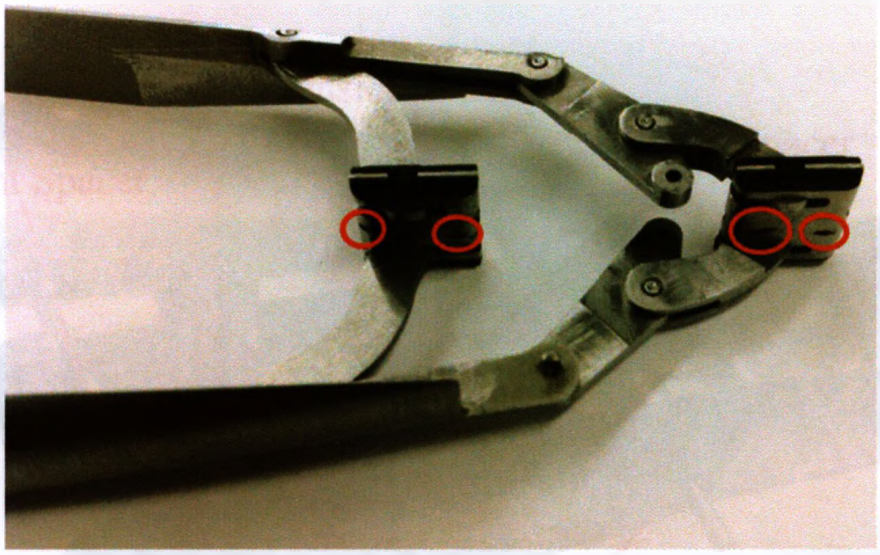

Figure 5.6: The jaws, links, and sliders. Through holes on the sliders for tungsten cables are circled in red.

Figure 5.7: The grasper in a jaws closed position.

In Figure 5.8, the grasper mechanism is installed in the grasper housing, which is attached to the instrument shaft. In addition to previous images, this closeup shows the sliding rails in the grasper housing, the tungsten cables installed in the sliders (untensioned), and the installed Front Spacer and Back Spacer. The tungsten cables wrap around the Front and Back Spacers using them as pulleys. The spacers rotate about concentric pins, which in the image are sticking out for easy removal in the case of required disassembly during construction. The plugs embedded within the grasper housing, which support the spacer pins, can also be seen. They differ from the CAD model only by not being flush against the grasper housing. This change was made to simplify the machining process. Finally, the grasper mechanism installed in the grasper housing is once again shown from the side in Figure 5.9.

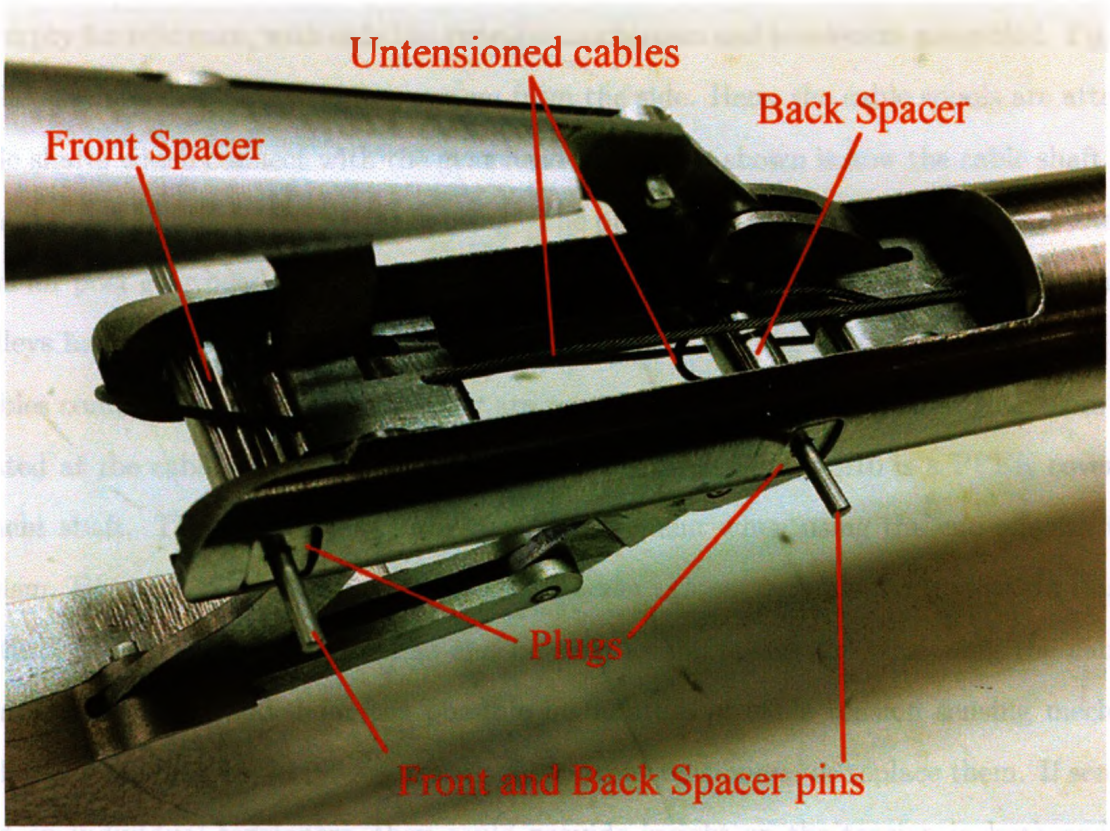

Figure 5.8: The assembled grasper in the instrument shaft with untensioned cables.

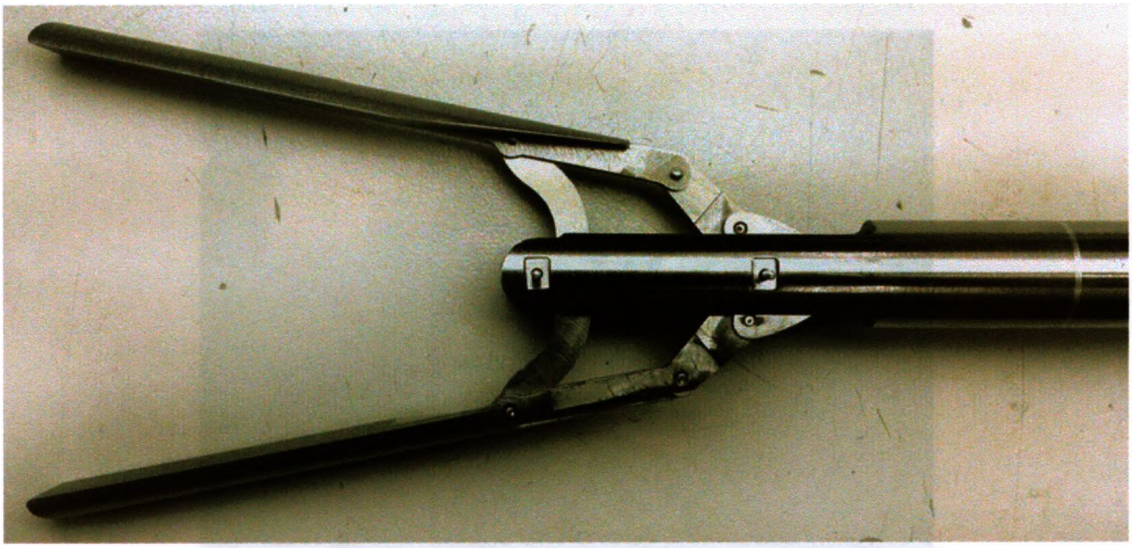

Figure 5.9: The assembled grasper in the instrument shaft (side view).

Lastly, the cable routing system is shown. In Figure 5.10, the bottom of the motor housing is shown empty for reference, with only the twisting mechanism and tensioners assembled. Figure 5.11 shows the assembled cable tensioning system from the side. Here, the cable spools are attached to the cable shafts which connect with the gear head shaft. Not shown is how the cable shaft extends upwards through the top of the motor housing. The protruding shaft is then attached to the optical encoders for post gear head backlash assessment, and possible further control considerations. Pins and pulleys have been installed in the bottom of the motor housing for the cables to wrap around. Two cables coming from each grasper slider are routed back through individual tensioners and are terminated at the cable spool. An additional difference from Figure 5.10 is a PEEK cover on the instrument shaft. This was installed for smooth movement when using the end effector twisting mechanism. Figure 5.12 once again shows the tensioner system from the back view. In this figure, screws threaded through the tensioners can be seen as the means for tensioning the cables. As well, ample space is provided for the possible installation of cable tension sensing mechanisms. Particularly, something could integrate with the current tensioners, or replace them. If sensors are installed on individual tensioners, they could provide insight on the tension in both ends of the cables attached to the sliders. Empty holes in this and the previous figure have been threaded and are used for screwing together neighbouring parts such as the motors and the top of the motor housing.

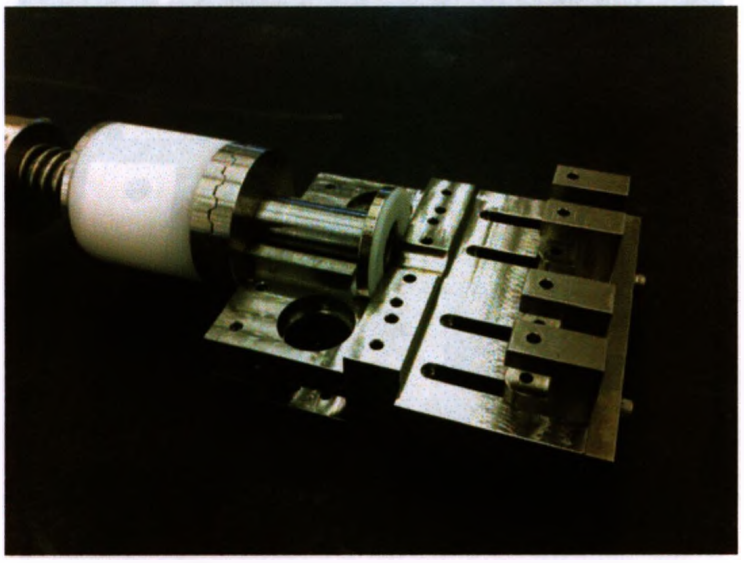

Figure 5.10: The bottom of the empty motor housing.

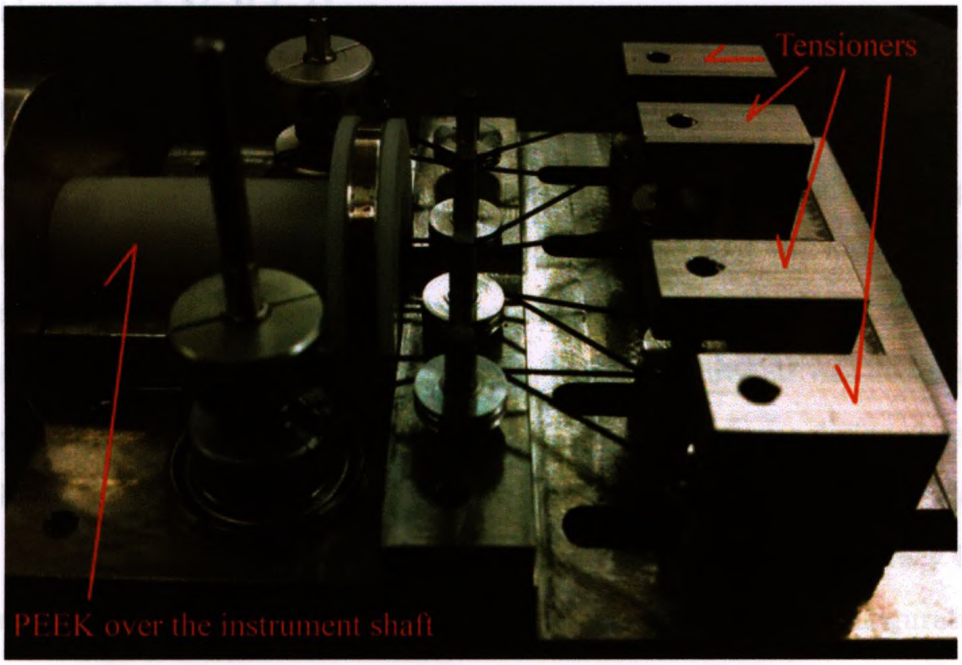

Figure 5.11: The cable tensioning system. PEEK covers the instrument shaft for smooth twisting (View 1).

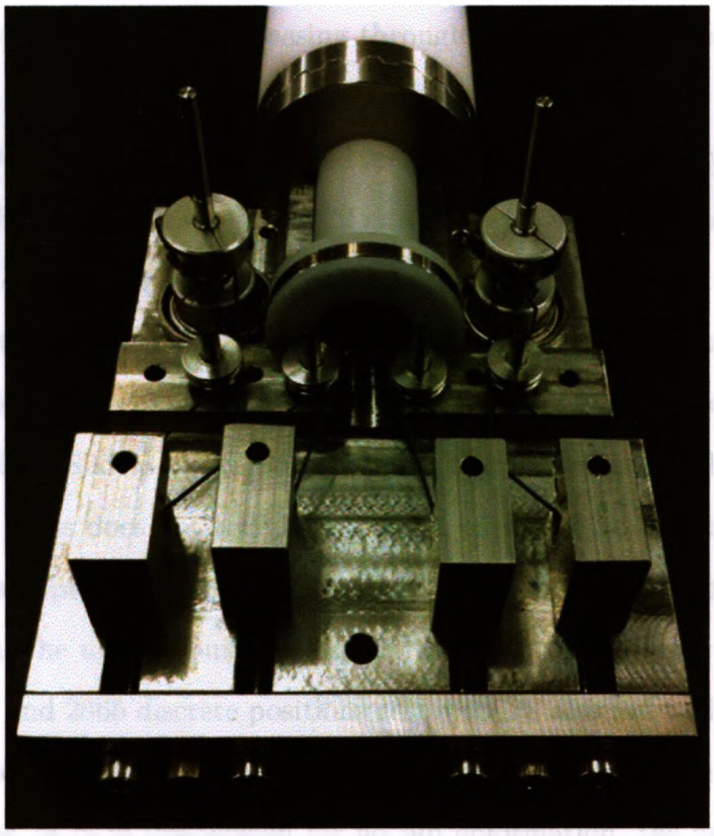

Figure 5.12: The cable tensioning system (View 2).

5.3 Testing and Validation

5.3.1 Workspace Assessment

The first design assessment considered the general motion of the device and the comparison of the real workspace to the CAD model workspace. It was observed that the instrument was able to reach all theoretical limits when compared to the SolidWorks 2010 model (Figures 5.13 through 5.16). Only the angle was measured as a comparison in these figures. It was deemed unnecessary to extensively evaluate the workspace limits, because the grasper was designed to separate its jaws wider than necessary. Only in vivo experiments could truly assess the device workspace applicability. Furthermore, it was not important to determine positional accuracy because cable elongation, which largely contributed to the accuracy of the desired jaw configurations, was not taken into account. Visually it can be seen that the prototype closely matches the CAD model. An important feature relating to the geometry was the ability to pass through a trocar. Although the prototype shaft was constructed using a 12.7 mm outer diameter tube, the instrument in jaws closed position was still capable of passing through a 12 mm diameter trocar, which clearly provided some leeway.

Post gear head optical encoders were included on the prototype to assess the amount of backlash in the system. With the 53:1 gear ratio of the 22 mm diameter Maxon Planetary Gearhead GP 22 C, a backlash of 1.6° existed. The range of motion of the Front and Back Sliders was 13.78 mm and 10.03 mm, respectively. As a conservative estimate for linear resolution, assuming a minimal rotational increment of 1.6° and the existing 5.58 mm diameter pulley mounted to the gear head shaft, the Front and Back Sliders could move in 0.078 mm increments with 163 and 128 discrete positions respectively. This does not take into account effects of cable elongation under tension. With the post gear head optical encoders providing 1250 lines per revolution mounted to eliminate the effects of backlash, the upper bound for linear resolution of the Front and Back Sliders was 0.0035 mm, with 3937 and 2865 discrete positions respectively, also not taking into account effects of cable elongation under tension. With a maximum cable load of half the largest shear load (77 N from Table 3.2) plus 14 N of pre-tension for no pin deformation, the cable strain is less than 0.4%, or 2 mm in a 500 mm long cable (Figure 3.54).

Figure 5.13: Jaws closed position.

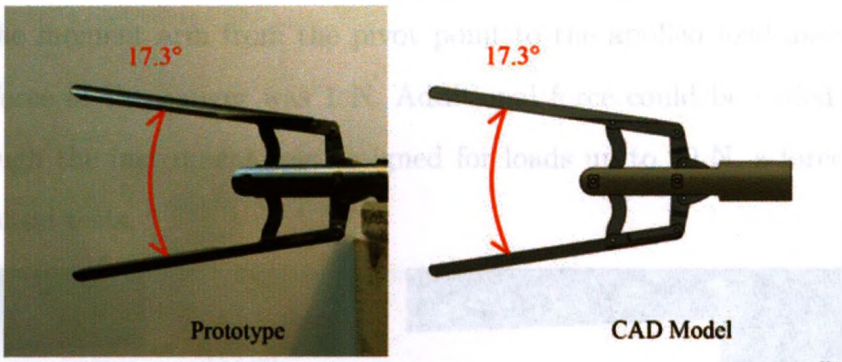

Figure 5.14: Jaws fully open position.

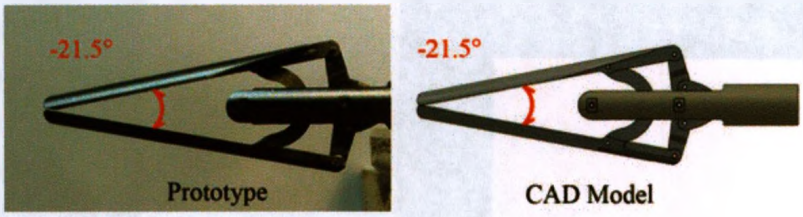

Figure 5.15: Jaws largest negative angle position.

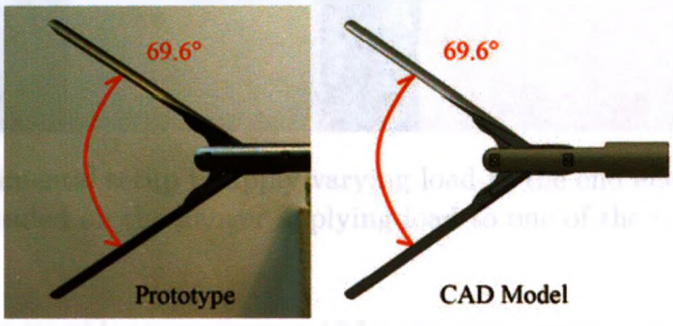

Figure 5.16: Jaws largest positive angle position.

5.3.2 Load Carrying Capacity

To validate the grasper's load carrying capacity, an experiment was set up to move the jaws over a number different positions with a varying applied load. This involved setting the Back Slider in four positions such that Joint 1 (Figure 4.1) was set to four positions over its range. In each of these positions, the Front Slider (Joint 6) was moved between its extremes with a force applied to one jaw at a time such that the jaws were being forced open or closed. The test setup is shown in Figure 5.17. The moment arm from the pivot point to the applied load and the jaw was 180 mm. The initial force of the hanger was 1 N. Additional force could be added in increments of 100 grams. Although the instrument was designed for loads up to 20 N, a force up to 10 N was applied in these initial tests.

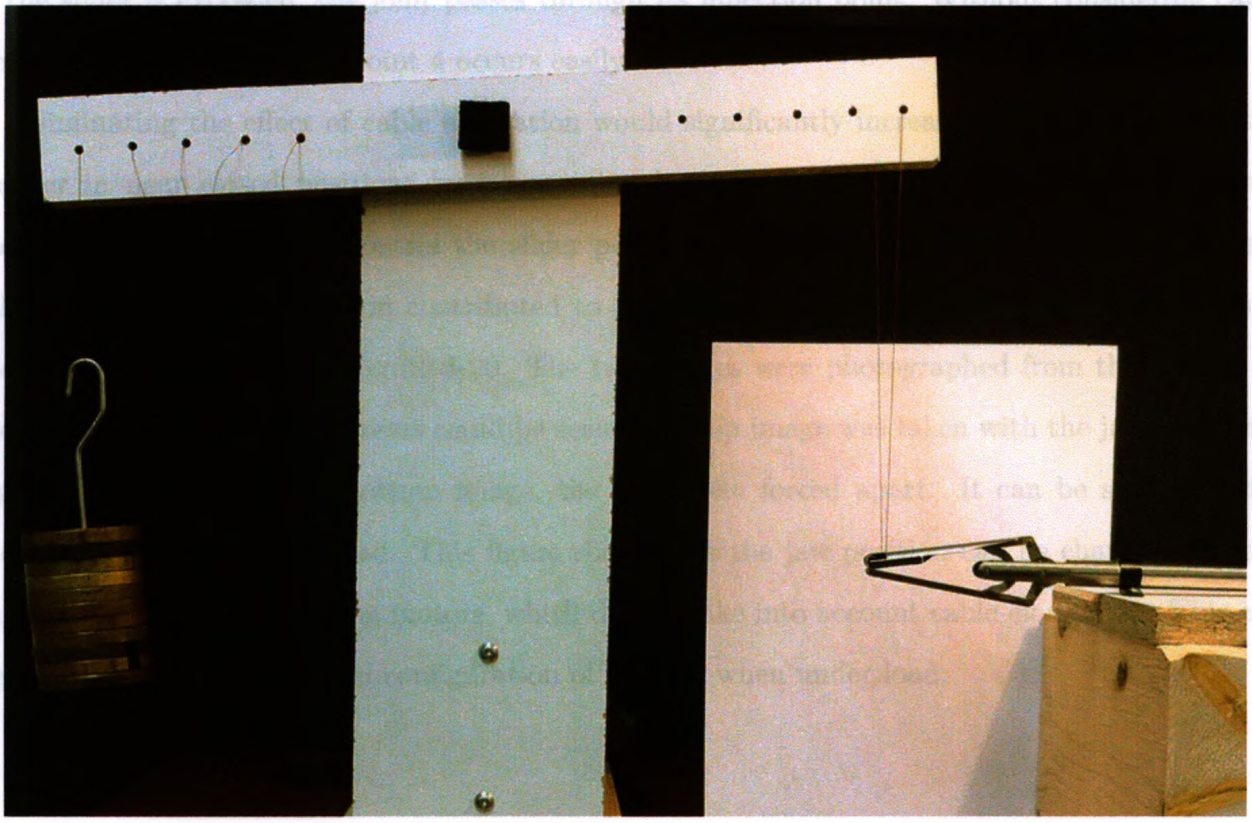

Figure 5.17: The experimental setup to apply varying load to the end effector jaw. One thousand grams is loaded on the hanger applying load to one of the jaw configurations.

The jaw was successfully able to manoeuvre 10 N of force in most positions. With well tensioned cables, the play in the jaw was minimized, which reduced the amount of jaw movement in any

desired position. The effect of jaw movement in a desired jaw position was due to cable elongation. The best performing positions were with a large thickness and low angle of palpation, similar to Figure 5.14. These positions exhibited the least jaw play and ease in moving the applied load.

In the forward position of the Back Slider with the jaw under load, Joint 4 moved through an inflection point. This is illustrated on the CAD model in Figure 5.18, and shown on the prototype in Figure 5.19. The load on the jaw causes a reaction force on Joint 4 that exceeds the maximum possible counter force exerted by the Back Slider. Additionally, the effect of cable elongation physically moves the Back Slider when it should ideally be stationary. When the Back Slider moves under load, it reduces the component of force counteracting the movement of Joint 4, which increases the force required for static equilibrium from the Back Slider. When the maximum force of the slider is exceeded, the joint passes through its inflection point. Without considering cable elongation, the inflection of Joint 4 occurs easily.

Eliminating the effect of cable elongation would significantly increase the performance of the grasper in near closed positions by maintaining both Front and Back Sliders in their desired positions. It is possible to control the slider positions while simultaneously taking into account cable tension. Cable extension contributed to less than 1 mm of travel in either slider. This is shown on the prototype in Figure 5.20. The two images were photographed from the bottom of the grasper so the slider positions could be seen. The top image was taken with the jaws squeezed together by hand. In the bottom image, the jaws were forced apart. It can be seen that the Front Slider moved under load. This figure shows that the jaw position can be changed without any input from the controlling motors, which do not take into account cable elongation. This can significantly effect the desired configuration of the jaw when under load.

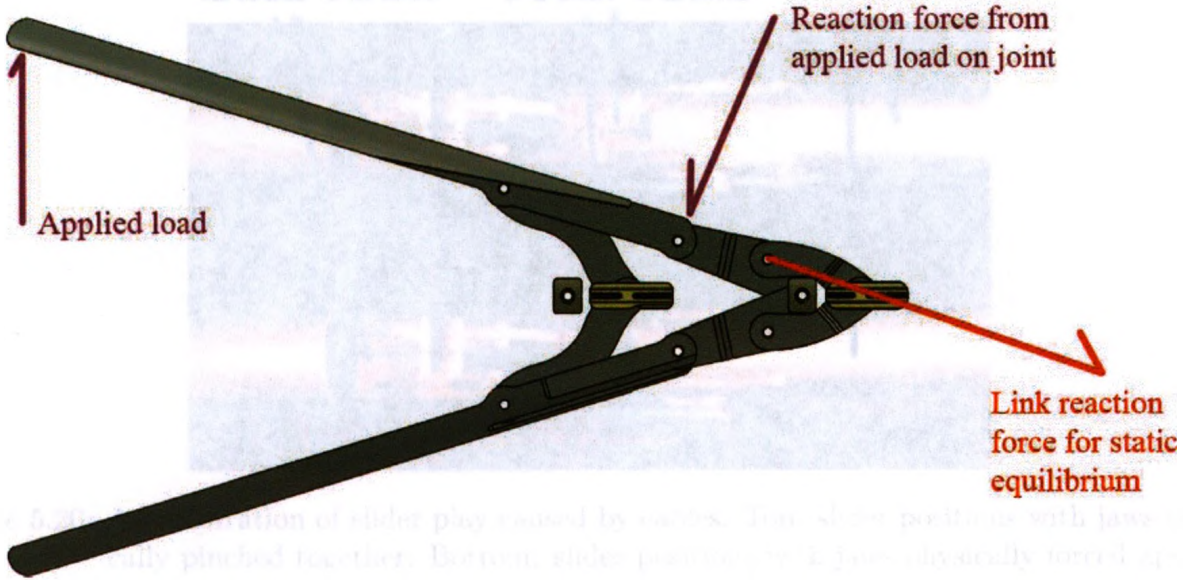

Figure 5.18: Forces on the jaw causing the inflection of Joint 4. The link has a smaller moment arm to counteract the joint force.

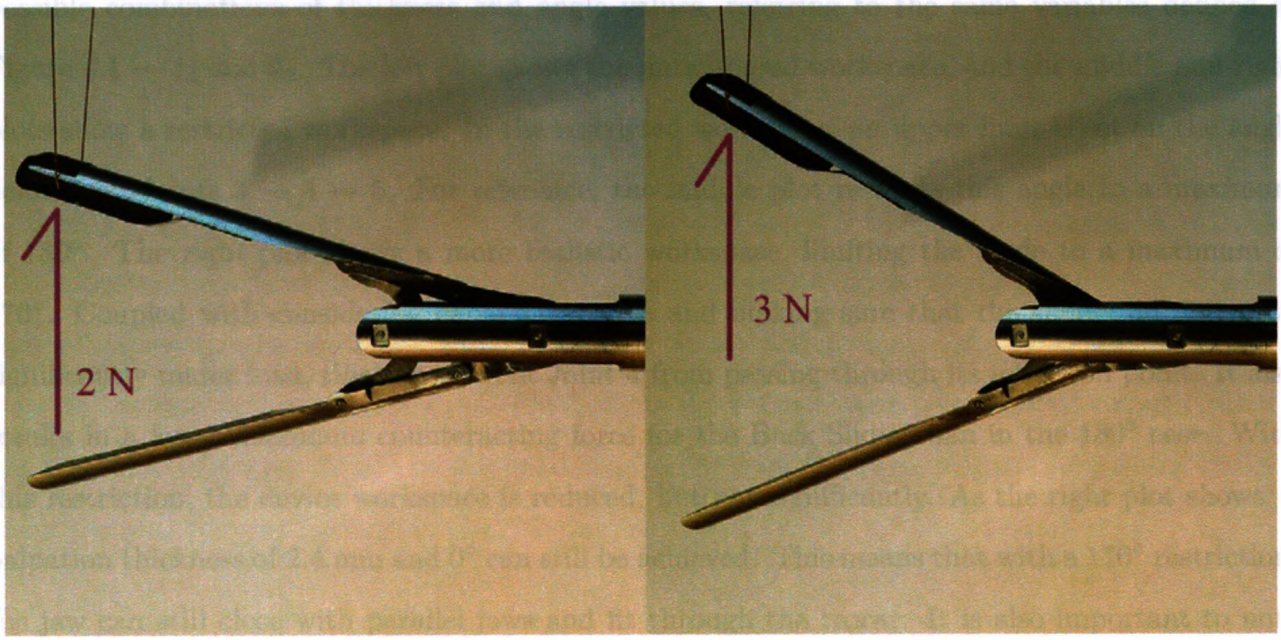

Figure 5.19: Inflection of joints. Left: 2 N force applied. Right: 3 N force applied. Motor positions are constant, cable extension causes movement of the Back Slider and makes it easier for the joints to inflect.

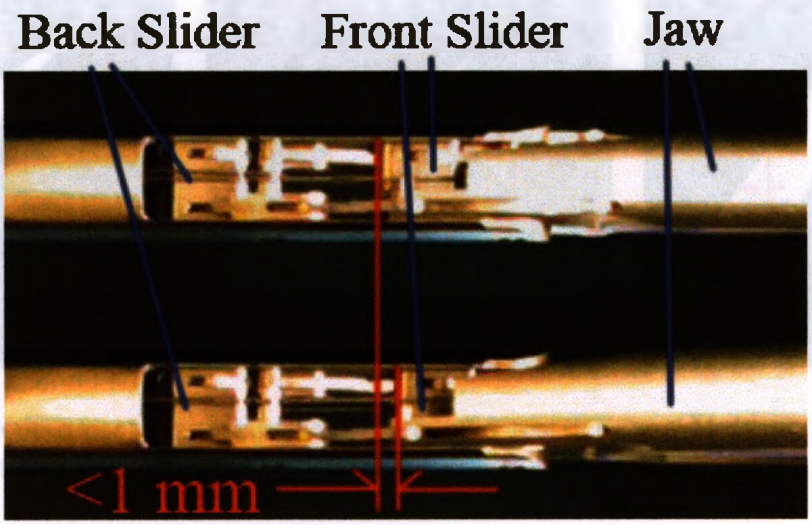

Figure 5.20: An illustration of slider play caused by cables. Top: slider positions with jaws physically pinched together. Bottom: slider positions with jaws physically forced apart.

Avoiding the inflection of Joint 4 must also be considered. Although this reduces the workspace, further assessment could be done to examine if doing so would be altogether detrimental. Figure 5.21 shows three plots of possible palpation thicknesses and angles. The white area describes possible combinations of thickness and angle values, referring to the same variables defined in Figure 4.1 — t_d and θ_d. The left plot shows the untampered workspace, and the middle and right plots show a restricted workspace. In the restricted workspace, an upper limit is set on the angle defined by Joints $3 \rightarrow 4 \rightarrow 5$. For reference, the middle plot restricts this angle to a maximum of 180°. The right plot shows a more realistic workspace, limiting the angle to a maximum of 170°. Coupled with considering cable elongation and making sure that the sliders do not move significantly under load, this can prevent Joint 4 from passing through its inflection point. It also results in a lower maximum counteracting force for the Back Slider than in the 180° case. With this restriction, the device workspace is reduced, but not significantly. As the right plot shows, a palpation thickness of 2.4 mm and 0° can still be achieved. This means that with a 170° restriction, the jaw can still close with parallel jaws and fit through the trocar. It is also important to note that this thickness is measured from approximately half way down the jaw length, and as such, thinner lung sections can be palpated by using the tip of the jaws and a negative palpation angle.

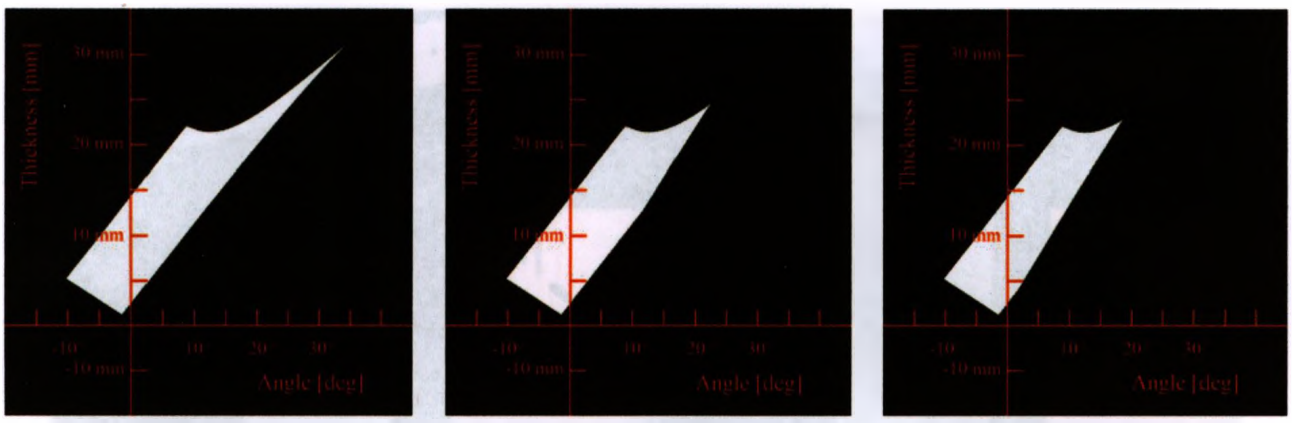

Figure 5.21: Different prototype workspaces. Left: No restrictions. Middle: 180° restriction on inflection joint. Right: 170° restriction on inflection joint.

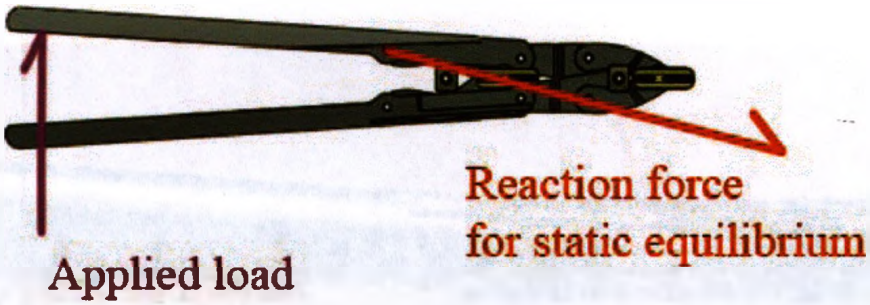

Figure 5.22: High components of force are required to maintain equilibrium in a near-closed position.

In working with the joint inflection in the worst possible jaw configuration, the jaws were still able to manoeuvre a 3 N load (Figure 5.23). This movement represents the motion of a standard Babcock grasper, having 1 DOF and moving in a scissor like manner. Similar to the Back Slider, when in a near closed jaw position, the Front Slider has a small component of force to react against the jaw force (Figure 5.22). The upper limit of force that the Front Slider could exert was not determined to prevent damage to the grasper and the cables.

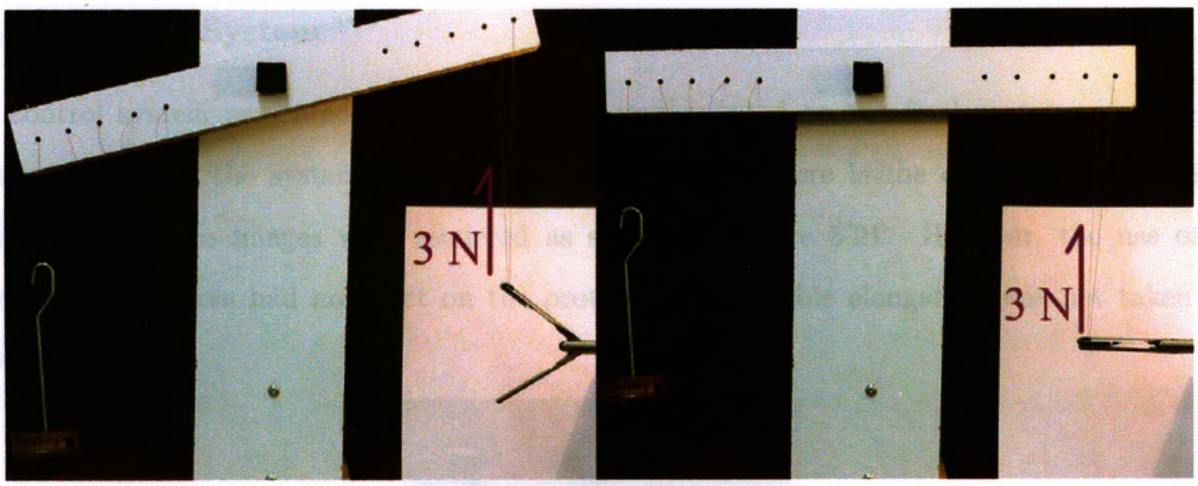

Figure 5.23: With a 3 N force, the end effector was able to move through its range of motion similar to a Babcock grasper.

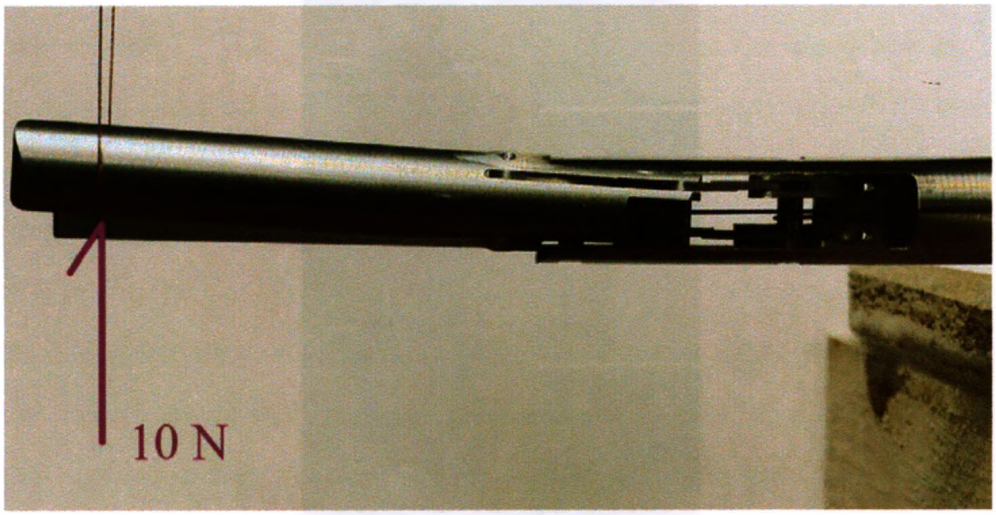

Figure 5.24: Jaw under side load. Deformation of the jaw prevents it from closing because it would collide with the housing.

Finally, the capability to hold a load across the jaws was tested. A 10 N load was applied to the jaws. This was to examine the effects on the jaw when manipulating a lung. No permanent damage was observed, and under load the jaws were able to articulate. Due to deformation of the jaws and the attached linkages under this load, this jaw movement was not suitable for palpation, because part interference would have occurred with the jaws and the grasper housing, preventing the jaws from closing (Figure 5.24).

5.3.3 Control System

The control system presented in Chapter 4 was implemented on the final prototype. The only difference between the system presented in Chapter 4 and here is the different jaw geometry. Different workspace images were rendered as shown in Figure 5.21. However, the use of the restricted workspaces had no effect on the prototype since cable elongation was not taken into account.

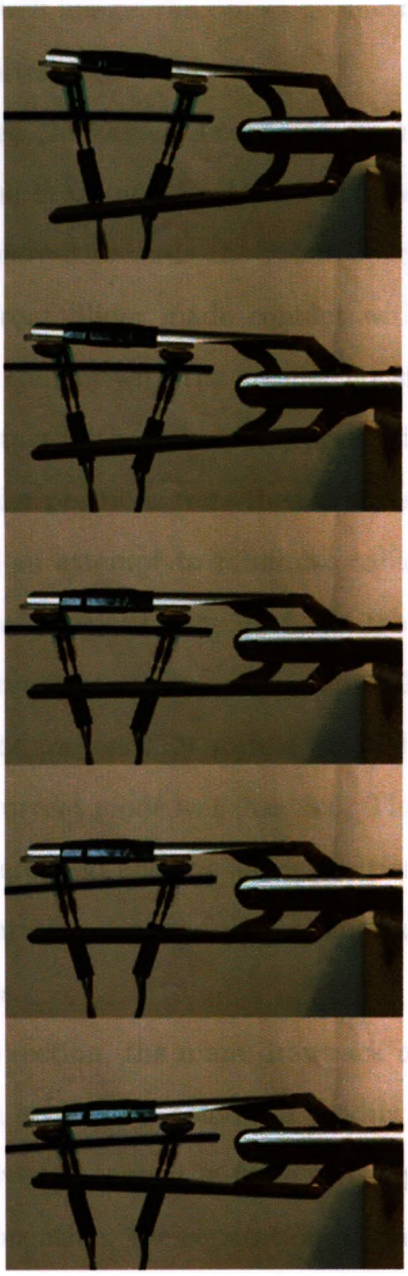

Figure 5.25: Automatic palpation control system on the prototype.

The control system worked as desired — within its workable limits, the jaw geometry would adhere to different shapes, making sure the jaws stayed parallel to the palpated object. As in the mock design presented in Chapter 4, a flexible plastic beam was used to palpate against, demonstrating automatic object tracking by the grasper. Figure 5.25 shows the grasper with two FSRs mounted to the upper jaw closing down on an object and conforming to its shape. Through the first three images, the object to palpate starts horizontal, and the grasper jaws orient themselves accordingly. In the fourth image, the object geometry changes, and in the fifth image, the jaws once again orient themselves accordingly.

The calibration procedure used the same methods as described in Chapter 4 — a constant current mode was selected and the Front and Back Sliders moved until obstructed. On the final prototype, first the Front Slider moved towards the Front Spacer, then both sliders moved back until physically stopped. The Front Slider made contact with the Back Spacer, and the link attached to the Back Slider made contact with the grasper housing (Figure 5.26). In this manner, the grasper jaws never made contact with each other, preventing damage to the system during this open loop procedure. The slider positions were then designated their distances from the Back Spacer, Joint 3 in Figure 4.1. In an attempt to minimize cable elongation effects, two methods of determining the slider reference positions were used. In the first, when an object obstructed movement, the motors stayed in constant current mode until 100 consecutive equivalent readings were measured. In the second, the motors first waited for 100 consecutive readings in constant current mode, then the constant current mode was disabled. This relaxed the cables. Another 100 consecutive equivalent readings were read and the slider positions determined. Neither of the two methods performed any better during automatic palpation, and the first method was arbitrarily chosen for subsequent experiments.

As mentioned in the previous section, the main drawback of the control system was the disregard for cable elongation. Thin geometries could not readily be palpated. Thin palpation jaw configurations could not be achieved because the force of the palpated object would spread the jaws apart. By ignoring cable elongation, the separation of the jaws could not be corrected for. One possible method of reducing cable elongation effects without changing the current system would be to monitor the motor current and include it in the control loop. This would provide a

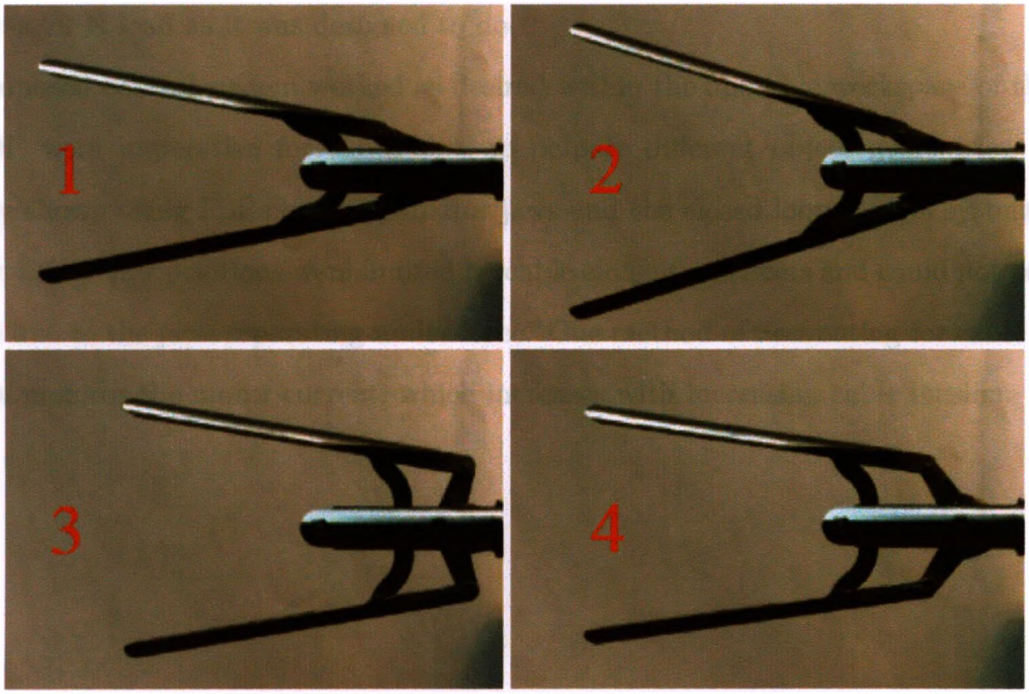

Figure 5.26: The prototype calibration procedure. 1 – A general jaw position. 2 – Front Slider forward. 3 – Front and Back Sliders backward. 4 – Ready to palpate.

low accuracy estimate of the cable tension, but could demonstrate the benefits of taking elongation into account.

5.4 Conclusion

The workspace of the grasper was shown to be equal to the theoretical workspace of the CAD model. There were no evident problems in the movement of the graspers under the no-load condition. Assessment of positional accuracy of the jaws was not undertaken due to the presence of cable elongation, which contributed to the majority of play in the system. It is a necessity to include cable elongation in the control loop or to use direct sensing means for the positions of the sliders.

The 2 DOF system has a joint inflection point that must be worked around. Cable play exaggerated the effect of joint inflection by allowing the Back Slider to move. If cable play could be minimized and the workspace of the grasper redefined to avoid the inflection point, the grasper could work as desired. After examination of the grasper load capacity using a maximum of 10 N, it is hypothesized that by removing the effects of the inflection point, the grasper could hold and

manoeuvre a 20 N load as it was designed to do.

The proposed control system worked as desired within the operable workspace of the grasper. The 2 DOF were imperative for the ability to palpate different object geometries. This was successfully shown using FSRs on the palpator jaws and the closed loop control system described in Chapter 4. The jaw positions were limited by cable elongation effects and could not palpate thin geometries due to the jaws separating under force. One method of accounting for cable elongation effects is to monitor the motor current, which increases with increasing cable tension.

Chapter 6

Conclusions

6.1 Summary

This thesis describes the design and development of a novel hand held minimally invasive lung tumour localization device. Its purpose is to surpass the performance of present laparoscopic devices and approach the capabilities of the human finger without the need for open surgery. To do so, the device is designed to incorporate the use of multiple sensing modalities, and uses a novel mechanical linkage for optimal tissue palpation. Also presented is a proof of concept for a control scheme to improve palpation over surgeon-controlled palpation. A thorough review of the relevant literature concludes that no such device has been developed before.

With an iterative design process and design analyses, it was determined the proposed device could be used under the expected 20 N load of a human lung, while achieving a factor of safety of 4. The design includes the ability to hold both an ultrasound and tactile sensor. After the final prototype construction, it was shown that the device could attain its theoretical workspace, and was able to manipulate and move loads of 10 N. A proof of concept control system using force sensing resistors in replacement of the tactile sensor demonstrated that the presented design could palpate different thicknesses and orientations of tissue automatically. Due to the cost and uniqueness related to the presented prototype, validation experiments were not conducted to failure.

6.2 Concluding Remarks

This thesis provides basis for future work on a minimally invasive lung tumour localization device adhering to fundamental design restrictions. The project consists of three novel ideas:

Multiple Sensing Modalities

The use of multiple sensors in a minimally invasive lung tumour palpation device is an idea not yet tested. In particular, the design holds two imaging sensors, ultrasound and tactile. Ultrasound is a standard method of examining subsurface tissue. Its obtained image is perpendicular to the ultrasound sensor surface. Tactile sensing creates a topographical pressure map of tissue, which is an image parallel to the sensor surface. Combining these two technologies increases the available information on the tissue and underlying features. Considering the two orthogonal imaging planes, it is reasonable to assume that a three-dimensional (3D) model of the subsurface tissue can be created using data fusion techniques. In addition to the aforementioned sensors, the device may also make use of kinaesthetic force feedback sensors mounted on linkages of the grasper mechanism. These sensors are intended for more accurate bulk force measurement over the palpated region than can be achieved with the tactile sensor alone. Furthermore, they can enhance the real time capabilities of possible control systems on the device since they have the capability to be sampled with a higher frequency than the ultrasound and tactile sensors, especially if data fusion is included in the control loop.

Two Degrees of Freedom

In traditional grasper-based minimally invasive palpating designs, only one degree of freedom is used. This severely limits the palpable regions of tissue. The two degrees of freedom incorporated in the presented design allow for varying geometries of tissue to be palpated. Angled, flat, thick, and thin tissue samples can be palpated in an optimal manner presenting two benefits. The first is that a large portion of the imaging sensor surfaces can be used since they have the ability to align themselves tangentally to the tissue. The second is that uniform pressure can be applied to the tissue, improving imaging and preventing damage.

Robotics-Assisted Palpation

It was shown in the literature that robotics-assisted palpation increases the performance of localizing lung tumours. With the included sensors and degrees of freedom on the end effector design, an automated palpation process can be applied. This has yet to be seen for minimally invasive palpation mechanisms. Coupled with the data acquiring sensors, the tissue can be palpated in an optimal manner in a repeatable way, which is hypothesized to increase tumour localization performance. Taking advantage of the 2 DOF, a demonstrative control system was presented using force sensing resistors.

6.3 Recommendations and Future Work

During the course of this project, a prototype was designed and constructed. Time limitations prevented the integration of the proposed sensors. However, using force sensing resistors, a proof of concept for an automated control scheme was presented. Preliminary validations were conducted on the device, but further examination of system performance should be done. Possible future work is discussed in three sections — mechanical, electrical and controls, and testing and validation.

6.3.1 Mechanical Recommendations

The first recommendation is the inclusion of strain gauges on the grasper links. The strain gauges have already been selected but not mounted. Including the strain gauges is also coupled with their subsequent calibration. A test setup needs to be designed to apply varying loads along a single jaw and both jaws, in varying directions for varying end effector configurations. The results could be tabulated and referred to during automatic palpation. In particular, this may help to approximate the palpation load while simultaneously acquiring information from the ultrasound and tactile sensors.

Strain gauges should also be placed on the cable tensioners for cable tension and elongation feedback. This may include designing something to work with the existing tensioners, or something to replace them. The location of the current tensioners provides ample space for sensor integration. To further reduce cable elongation, solid drawn wire may be used to replace sections of the cable

that do not experience bending. This may help by minimizing the working cable length. Challenges include proper cable clamping to the intermediate material to maintain cable strength.

Force measurements from live patient surgeries could be obtained to provide information on the loads that actually occur during lung tumour localization and excision. This information could allow for more accurately defined design specifications, resulting in the creation of either thinner, more complex designs, or thicker, more robust designs. Results could conclude that heat treated material for the jaws is unnecessary. Eliminating the required heat treating process is desired due to the added cost and complexity in manufacturing.

The integration of the ultrasound and tactile sensors remains to be carried out. This involves work communicating with the sensor manufacturers to develop specific geometry for each sensor that will comply to the design requirements of the end effector, such as applied load and size. This work may also involve investigating different materials to remove the restriction of using stainless steel alloy 440C.

The use of wrist joints should be considered. The inclusion of wrist joints could improve the use of the end effector by increasing its spatial configurations, making it easier to palpate tissue in otherwise hard to reach or impossible locations. Several challenges accompany the inclusion of wrist joints. End effector positional accuracy would be reduced due to the accumulation of error in additional degrees of freedom. The end effector total length would likely increase, making it unsuitable for the chest cavities of certain patients. The effect of bending, and sliding of the sensor and actuating cables against neighbouring components may be detrimental. Finally, the added complexity of the system may no longer allow for intuitive human control of the device.

Assessment of the geometry of the current design could be undertaken. Following the recommendations of an experienced thoracic surgeon, the end effector geometry was designed similar to a commercial product. The current jaw length and end effector workspace should be re-examined following experimental trials.

The motor housing was over designed for simplicity. A material assessment could be undertaken to replace the steel components with light weight materials, lessening the strain on the surgeon holding the device. A more aesthetically pleasing design could be produced, which may include encompassing the motors within the housing. Other considerations for the motor housing include

simple assembly and disassembly, preferably using plastics that can easily snap in and out of place without affecting the system performance. This could make for easy separation of components for sterilization. Ideally, the complete device should be sterilizable.

Due to the sliding effect seen in the proof of concept control system, a third degree of freedom — the ability to move the end effector back and forth should be reviewed. Sliding could cause tissue damage and its effect should also be assessed. The addition of a degree of freedom could require a complete redesign of the motor housing.

Finally, haptics and visual feedback are desired. This may serve as grounds for a new research project, as these elements were beyond the scope of this project. This could include but is not limited to a redesigned instrument handle including input controls currently not present, and haptic feedback to the hand of the operator.

6.3.2 Electrical and Controls Recommendations

With the inclusion of strain gauges on the cable tensioners, identifying tension in both the Front and Back Slider actuating cables could provide more effective control solutions. As is, the system performance is limited by the flexibility caused primarily by cable elongation. The motor controllers do not take this into account. Another method to remove cable elongation effects would be to include a position sensor directly measuring the slider positions. Such a sensor may have to be custom designed due to space restrictions.

Linkage-mounted strain gauges should be used to assess palpation force. In combination with the imaging sensors, the strain gauges could be used as a high frequency palpator force feedback method between imaging sequences to optimize control of palpation.

Future research regarding the control systems of the device could focus on developing a method to fuse the data of the ultrasound and tactile sensors. This should result in an intuitive information display and provide more information on the palpated tissue attributes. In a clinical context, it could also provide an accurate method of localizing a tumour and eliminate the need for a radiologist to be on site during surgery.

Backlash in the system has not been determined. Post gear head optical encoders already exist on the device but have not been used. It should be determined if they are required to compensate

for the effects of backlash, or whether the gear heads can be used alone.

Haptic and visual feedback are desired. Haptic feedback requires a control system that can interact with the surgeon, somehow relaying the existence of a tumour, to be designed. Related to this is the possibility of including a visual feedback system that could help the device operator identify and differentiate different tissue attributes.

Above all, the sampling frequency of the system using imaging sensors is low. The raw information from the selected tactile sensor alone has a frequency of 10 Hz. Including algorithms for fusing data with ultrasound information and overall image manipulation, the frequency could be even lower. This may restrict real time operation. The proof of concept control system for this project was used on Windows XP Professional because of the simple integration with the motor controllers. Similarly, the ultrasound and tactile sensors integrate with a Windows environment. Designing an embedded system could increase the performance of the device. Possible options include the use of Windows CE or IntervalZero RTX to maintain a Windows environment. This would simplify the integration of components with a computer while at the same time achieving a real time solution.

6.3.3 Testing and Validation Recommendations

Tests should be done to assess the effect of sliding palpation on lung tissue, which is currently caused by the 2 DOF in the presented design. The assessment and performance difference of an additional DOF can be analyzed by mounting the design on a robotic arm. The robotic arm could simulate the third DOF — the ability to move forward and backward to reduce sliding.

To validate the ease of use and effectiveness of the current system, palpation experiments on tissue (with phantom tumours embedded) should be conducted using multiple instrument operators with varying levels of expertise. System performance could be judged by the sensitivity and specificity of the device as a diagnostic test, and the ability of the operator to use the device. Similarly, the instrument should be tested in vivo to compare its performance against currently available minimally invasive localization devices.

References

[1] Canadian Cancer Society's Steering Committee, "Canadian Cancer Statistics 2010: Toronto," *Canadian Cancer Society*, 2010.

[2] L. Ellison, L. Gibbons, and the Canadian Cancer Survival Analysis Group, "Five-year relative survival from prostate, breast, colorectal, and lung cancer," *Health Reports*, vol. 13, no. 1, pp. 23–34, 2001.

[3] C. R. Wagner, N. Stylopoulos, and R. D. Howe, "The role of force feedback in surgery: Analysis of blunt dissection," in *International Symposium on Haptic Interfaces for Virtual Environment and Teleoperator Systems*, (Orlando, FL, USA), p. 73, 2002.

[4] B. Deml, T. Ortmaier, and U. Seibold, "The touch and feel in minimally invasive surgery," in *IEEE International Workshop on Haptic Audio Visual Environments and their Applications*, (Ottawa, Ontario, Canada), p. 6, October 2005.

[5] S. M. Hosseini, S. Najarian, S. Motaghinasab, A. T. Golpaygani, and S. Torabi, "Prediction of Tumor Existence in the Virtual Soft Tissue by Using Tactile Tumor Detector," *American Journal of Applied Sciences*, vol. 5, no. 5, pp. 483–489, 2008.

[6] J. Dargahi and S. Najarian, "An integrated force-position tactile sensor for improving diagnostic and therapeutic endoscopic surgery," *Bio-Medical Materials and Engineering*, vol. 14, pp. 151–166, May 2004.

[7] G. Tholey, J. P. Desai, and A. E. Castellanos, "Force feedback plays a significant role in minimally invasive surgery: results and analysis," *Annals of Surgery*, vol. 241, pp. 102–109, January 2005.

[8] A. Bicchi, G. Canepa, D. De Rossi, P. Iacconi, and E. Scillingo, "A sensor-based minimally invasive surgery tool for detecting tissue elastic properties," in *IEEE International Conference on Robotics and Automation*, vol. 1, (Minneapolis, MN , USA), pp. 884–888, Apr 1996.

[9] M. V. Ottermo, O. Stavdahl, and T. A. Johansen, "Palpation instrument for augmented minimally invasive surgery," in *IEEE/RSJ International Conference on Intelligent Robots and Systems*, vol. 4, (Sendai, Japan), pp. 3960–3964, September 2004.

[10] S. Schostek, C. N. Ho, D. Kalanovic, and M. O. Schurr, "Artificial tactile sensing in minimally invasive surgery – a new technical approach," *Minimally Invasive Therapy & Allied Technologies*, vol. 15, no. 5, pp. 296–304, 2006.

[11] A. M. Dollar, C. R. Wagner, and R. D. Howe, "Embedded sensors for biomimetic robotics via shape deposition manufacturing," in *The First IEEE/RAS-EMBS International Conference on Biomedical Robotics and Biomechatronics*, (Pisa, Italy), pp. 763–768, February 2006.

[12] J. Dargahi, S. Najarian, and K. Najarian, "Development and three-dimensional modelling of a biological-tissue grasper tool equipped with a tactile sensor," *Canadian Journal of Electrical and Computer Engineering*, vol. 30, no. 4, pp. 225–230, 2005.

[13] R. L. Feller, C. K. L. Lau, C. R. Wagner, D. P. Perrin, and R. D. Howe, "The effect of force feedback on remote palpation," in *IEEE International Conference on Robotics and Automation*, vol. 1, (New Orleans, LA, USA), pp. 782–788, April 2004.

[14] A. P. Miller, W. J. Peine, J. S. Son, and Z. T. Hammoud, "Tactile imaging system for localizing lung nodules during video assisted thoracoscopic surgery," in *IEEE International Conference on Robotics and Automation*, (Rome, Italy), pp. 2996–3001, April 2007.

[15] M. V. Ottermo, M. Ovstedal, T. Lango, O. Stavdahl, Y. Yavuz, T. A. Johansen, and R. Marvik, "The role of tactile feedback in laparoscopic surgery," *Surgical Laparoscopy, Endoscopy & Percutaneous Techniques*, vol. 16, pp. 390–400, December 2006.

[16] A. L. Trejos, J. Jayender, M. T. Perri, M. D. Naish, R. V. Patel, and R. A. Malthaner, "Experimental evaluation of robot-assisted tactile sensing for minimally invasive surgery," *2nd IEEE RAS EMBS International Conference on Biomedical Robotics and Biomechatronics*, pp. 971–976, October 2008.

[17] C. K. L. Lau, C. R. Wagner, and R. D. Howe, "Compliant background subtraction algorithms for tactile rendering," in *12th International Symposium on Haptic Interfaces for Virtual Environment and Teleoperator Systems*, pp. 32–39, March 2004.

[18] A. L. Trejos, J. Jayender, M. T. Perri, M. D. Naish, R. V. Patel, and R. A. Malthaner, "Robot-assisted Tactile Sensing for Minimally Invasive Tumor Localization," *The International Journal of Robotics Research*, vol. 28, no. 9, pp. 1118–1133, 2009.

[19] G. Tholey, A. Pillarisetti, W. Green, and J. P. Desai, "Design, development, and testing of an automated laparoscopic grasper with 3-d force measurement capability," in *Medical Simulation* (S. Cotin and D. N. Metaxas, eds.), vol. 3078 of *Lecture Notes in Computer Science*, pp. 38–48, Springer Berlin Heidelberg, 2004.

[20] H. Liu, D. P. Noonan, K. Althoefer, and L. D. Seneviratne, "Rolling mechanical imaging: A novel approach for soft tissue modelling and identification during minimally invasive surgery," in *IEEE International Conference on Robotics and Automation*, (Pasadena, CA, USA), pp. 845–850, May 2008.

[21] G. L. McCreery, A. L. Trejos, R. V. Patel, M. D. Naish, and R. A. Malthaner, "Evaluation of force feedback requirements for minimally invasive lung tumour localization," in *IEEE/RSJ International Conference on Intelligent Robots and Systems*, (San Diego, CA, USA), pp. 883–888, October 2007.

[22] K. Takashima, K. Yoshinaka, T. Okazaki, and K. Ikeuchi, "An endoscopic tactile sensor for low invasive surgery," *Sensors and Actuators A: Physical*, vol. 119, pp. 372–383, April 2005.

[23] M. MacFarlane, J. Rosen, B. Hannaford, C. Pellegrini, and M. Sinanan, "Force-feedback grasper helps restore sense of touch in minimally invasive surgery," *Journal of Gastrointestinal Surgery*, vol. 3, no. 3, pp. 278–285, 1999.

[24] J. Rosen, B. Hannaford, M. P. MacFarlane, and M. N. Sinanan, "Force controlled and teleoperated endoscopic grasper for minimally invasive surgery-experimental performance evaluation," *IEEE Transactions on Biomedical Engineering*, vol. 46, pp. 1212–1221, October 1999.

[25] J. Peirs, J. Clijnen, D. Reynaerts, H. V. Brussel, P. Herijgers, B. Corteville, and S. Boone, "A micro optical force sensor for force feedback during minimally invasive robotic surgery," *Sensors and Actuators A: Physical*, vol. 115, no. 2-3, pp. 447–455, 2004.

[26] T. Hu, A. E. Castellanos, G. Tholey, and J. P. Desai, "Real-time haptic feedback in laparoscopic tools for use in gastro-intestinal surgery," in *Medical Image Computing and Computer-Assisted Intervention MICCAI 2002*, (London, UK), pp. 66–74, Springer-Verlag, 2002.

[27] J. Dargahi, "An endoscopic and robotic tooth-like compliance and roughness tactile sensor," *Journal of Mechanical Design*, vol. 124, no. 3, pp. 576–582, 2002.

[28] H. Roham, S. Najarian, S. M. Hosseini, and J. Dargahi, "Design and fabrication of a new tactile probe for measuring the modulus of elasticity of soft tissues," *Sensor Review*, vol. 27, pp. 317–323, September 2007.

[29] M. D. Hooven, "Endoscopic surgical system with sensing means," U.S. Patent US 5667517, 09 16, 1997.

[30] M. E. H. Eltaib and J. R. Hewit, "Tactile sensing technology for minimal access surgery–a review," *Mechatronics*, vol. 13, pp. 1163–1177, December 2003.

[31] N. Kattavenos, B. Lawrenson, T. G. Frank, M. S. Pridham, R. P. Keatch, and A. Cuschieri, "Force-sensitive tactile sensor for minimal access surgery," *Minimally Invasive Therapy and Allied Technologies*, vol. 13, pp. 42–46, February 2004.

[32] R. Sedaghati, J. Dargahi, and H. Singh, "Design and modeling of an endoscopic piezoelectric tactile sensor," *International Journal of Solids and Structures*, vol. 42, pp. 5872–886, October 2005. PACAM VIII SPECIAL ISSUE.

[33] D. T. V. Pawluk, J. S. Son, P. S. Wellman, W. J. Peine, and R. D. Howe, "A distributed pressure sensor for biomechanical measurements," *Journal of Biomechanical Engineering*, vol. 120, no. 2, pp. 302–305, 1998.

[34] K. Baba, "Endoscope having an ultrasonic diagnosis function," US Patent US 4401123, 08 30, 1983.

[35] M. A. Goldfarb and E. Goldfarb, "Articulated surgical probe and method for use," US Patent Application US 2006/0094933 A1, 05 04, 2006.

[36] F. E. Shelton, J. N. Ouwerkerk, J. R. Morgan, and J. S. Swayze, "Motor-driven surgical cutting and fastening instrument with tactile position feedback," US Patent Application US 2007/0175962 A1, 08 02, 2007.

[37] M. A. Cundari, A. I. West, T. W. Roberts, and D. R. Widder, "Diagnosis and treatment of tissue with instruments," US Patent US 6063031, 05 16, 2000.

[38] A. C. Guyton and J. E. Hall, *Textbook of Medical Physiology, Tenth Edition.* W.B. Saunders Company, 2000.

[39] M. H. Lee and H. R. Nicholls, "Review article tactile sensing for mechatronics–a state of the art survey," *Mechatronics*, vol. 9, no. 1, pp. 1–31, 1999.

[40] W. J. Hyung, J. S. Lim, J. H. Cheong, Y. C. Lee, and S. H. Noh, "Tumor localization using laparoscopic ultrasound for a small submucosal tumor," *Journal of Surgical Oncology*, vol. 86, pp. 164–166, June 2004.

[41] N. S. Methil, Y. Shen, D. Zhu, C. A. Pomeroy, R. Mukherjee, N. Xi, and M. Mutka, "Development of supermedia interface for telediagnostics of breast pathology," in *IEEE International Conference on Robotics and Automation*, (Orlando, FL, USA), pp. 3911–3916, May 2006.

[42] A. West, J. Weinstein, N. Dewagan, and D. Krag, "Obtaining images of structures in bodily tissue using ultrasound and pressure-sensing," WO Patent Application WO 2001/039668 A1, 06 07, 2001.

[43] P. Kurowski, *Engineering Analysis with Solidworks Simulation 2010*, ch. 14. Mission, KS: Schroff Development Corporation, 2010.

[44] J. Shackelford, *CRC Materials Science and Engineering Handbook*, ch. 6. CRC Press, 3 ed., 2001.

[45] Latrobe Specialty Steel Co., "440 N-DUR Datasheet," 2007.

[46] H. Boyer, *Practical Heat Treating*, ch. 7. Metals Park, OH: American Society for Metals, 1984.

[47] G. Totten, *Steel Heat Treatment*, ch. 6. Boca Raton, FL: Taylor & Francis Group, 2 ed., 2007.

[48] B. Hannaford, J. Trujillo, M. Sinanan, M. Moreyra, J. Rosen, J. Brown, R. Leuschke, and M. MacFarlane, "Computerized endoscopic surgical grasper," *Medicine Meets Virtual Reality*, vol. 50, pp. 265–271, 1998.

[49] R. D. Howe, W. J. Peine, D. A. Kantarinis, and J. S. Son, "Remote palpation technology," *Engineering in Medicine and Biology Magazine, IEEE*, vol. 14, pp. 318–323, May 1995.

[50] R. S. Johansson and G. Westling, "Coordinated isometric muscle commands adequately and erroneously programmed for the weight during lifting task with precision grip," *Experimental Brain Research*, vol. 71, pp. 59–71, 1988.

[51] S. Y. Kim, K. U. Kyung, J. Park, and D. S. Kwon, "Real-time area-based haptic rendering and the augmented tactile display device for a palpation simulator," *Advanced Robotics*, vol. 21, pp. 961–981, September 2007.

[52] S. H. Kim, J. W. Milsom, J. M. Church, K. A. Ludwig, A. Garcia-Ruiz, J. Okuda, and V. W. Fazio, "Perioperative tumor localization for laparoscopic colorectal surgery," *Surgical Endoscopy*, vol. 11, pp. 1013–1016, October 1997.

[53] A. Krupa, G. Morel, and M. de Mathelin, "Achieving high precision laparoscopic manipulation through adaptive force control," in *IEEE International Conference on Robotics and Automation*, vol. 2, (Washington, DC, USA), pp. 1864–1869, August 2002.

[54] S. J. Lederman and R. L. Klatzky, "Sensing and displaying spatially distributed fingertip forces in haptic interfaces for teleoperator and virtual environment systems," *Presence: Teleoperators & Virtual Environments*, vol. 8, pp. 86–103, February 1999.

[55] W. J. Peine and R. D. Howe, "Do humans sense finger deformation or distributed pressure to detect lumps in soft tissue?," in *Proceedings of the ASME Dynamic Systems and Control Division*, pp. 273–278, 1998.

[56] R. Santambrogio, M. Montorsi, P. Bianchi, A. Mantovani, F. Ghelma, and M. Mezzetti, "Intraoperative ultrasound during thoracoscopic procedures for solitary pulmonary nodules," *The Annals of Thoracic Surgery*, vol. 68, pp. 218–222, July 1999.

[57] K. B. Shimoga and P. K. Khosla, "Touch and force reflection for telepresence surgery," in *Proceedings of the 16th Annual International Conference of the IEEE Engineering in Medicine and Biology Society*, vol. 2, (Baltimore, MD , USA), pp. 1049–1050, November 1994.

[58] R. H. Taylor, J. Funda, B. Eldridge, S. Gomory, K. Gruben, D. LaRose, M. Talamini, L. Kavoussi, and J. Anderson, "A telerobotic assistant for laparoscopic surgery," *Engineering in Medicine and Biology Magazine, IEEE*, vol. 14, pp. 279–288, May 1995.

[59] R. Taylor, P. Jensen, L. Whitcomb, A. Barnes, R. Kumar, D. Stoianovici, P. Gupta, Z. Wang, E. Dejuan, and L. Kavoussi, "A steady-hand robotic system for microsurgical augmentation," *The International Journal of Robotics Research*, vol. 18, pp. 1201–1210, December 1999.

[60] S. Walairacht, Y. Koike, and M. Sato, "String-based haptic interface device for multi-fingers," in *IEEE Virtual Reality Conference*, (New Brunswick, NJ , USA), p. 293, March 2000.